Waves and instabilities on vortices in stratified and rotating fluids

Junho Park

École Polytechnique
Laboratoire d'Hydrodynamique (LadHyX)

Thèse présenté pour obtenir le grade de

DOCTEUR DE L'ÉCOLE POLYTECHNIQUE

spécialité : mécanique

par

Junho Park

Waves and instabilities on vortices in stratified and rotating fluids

---

Soutenue le 16 novembre 2012 devant le jury composé de:

Paul Billant	Directeur de thèse	Ecole Polytechnique, Palaiseau
Thierry Dauxois	Examinateur	Ecole Normale Superieure de Lyon, Lyon
Bérengère Dubrulle	Examinatrice	SPHYNX-CNRS, CEA, Gif sur Yvette
Bach Lien Hua	Examinatrice	IFREMER, Plouzané
Stéphane Le Dizès	Rapporteur	IRPHE-Aix-Marseille Université, Marseille
Leo Maas	Rapporteur	NIOZ, Utrecht University, The Netherlands
Riwal Plougonven	Examinateur	LMD-ENS, Paris

Junho Park

Waves and instabilities on vortices in stratified and rotating fluids

Résumé

En milieu stratifié-tournant, les ondes supportées par un tourbillon colonnaire vertical peuvent être instables en raison d'un rayonnement d'ondes, un phénomène connu sous le nom d'instabilité radiative. Dans la première partie de cette thèse, on étudie numériquement et analytiquement l'effet d'une rotation planétaire sur cette instabilité. En présence de rotation cyclonique, le rayonnement d'ondes diminue et le taux de croissance maximum de l'instabilité radiative décroît exponentiellement quand la rotation augmente. Il devient negligeable quand le nombre Rossby est inférieur à l'unité. En présence de rotation anticyclonique avec un nombre de Rossby supérieur à -1, l'instabilité centrifuge est stable mais on montre que l'instabilité radiative se produit également si le nombre d'onde azimutal est plus grand que 2 et le profil de vorticité est suffisamment raide. Le taux de croissance dans ce régime fortement anticyclonique est comparable à celui dans le régime cyclonique. La principale conclusion est donc qu'un tourbillon colonnaire en milieu stratifié-tournant peut être instable pour n'importe quel nombre de Rossby. Le mécanisme et les propriétés de l'instabilité radiative sont expliqués par une analyse WKBJ pour grands nombres d'ondes.

Dans la deuxième partie de cette thèse, la stabilité de l'écoulement de Taylor-Couette stratifié est analysée quand la vitesse angulaire augmente radialement, une régime encore jamais exploré. On montre que cet écoulement est instable vis à vis d'une instabilité stratorotationelle. Cette instabilité est similaire à l'instabilité radiative d'un tourbillon en régime fortement anticyclonique. Ces résultats révèlent que l'écoulement de Taylor-Couette stratifié est toujours instable sauf dans la limite d'une rotation solide.

Abstract

In stratified rotating fluids, waves sustained by a vertical columnar vortex can be unstable due to an outward radiation of waves, a phenomenon known as the radiative instability. In the first part of this thesis, we investigate numerically and analytically the effect of a planetary rotation on this instability. When the planetary rotation is cyclonic, the wave radiation is reduced so that the maximum growth rate of the radiative instability decreases exponentially as the rotation increases. It becomes negligibly small when the Rossby number is smaller than unity. When the planetary rotation is anticyclonic with Rossby number higher than -1, the centrifugal instability is stable but it is shown that the radiative instability also occurs when the azimuthal wavenumber is larger than 2 and the vorticity profile sufficiently steep. The maximum growth rate in this strong anticyclonic regime is comparable to the one in the cyclonic regime. The main conclusion is therefore that a columnar vortex in a stratified rotating fluid can be unstable for any Rossby number. The mechanism and properties of the radiative instability are explained by means of WKBJ analyses for large wavenumbers.

In the second part of the thesis, the stability of the stratified Taylor-Couette flow is studied when the angular velocity increases radially, a regime never explored before. We show that such flow is unstable to a strato-rotational instability. Such instability is closely related to the radiative instability of a vortex in the anticyclonic regime. These results reveal that the stratified Taylor-Couette flow is always unstable except for pure solid-body rotation.

Acknowledgement

First of all, I would like to thank to Paul Billant, who was my supervisor during my Ph.D life at LadHyX. It was a honour to me that I was able to work with him, not only because of his kind and nice personality but also because of his brilliance and enthusiasm on my Ph.D subject. Merci beaucoup pour tous!

I would like to thank all the people at LadHyX. (I hope I don't forget all the names while writing ;)) Starting from Patrick Huerre who brought me to Ecole Polytechnique for the master program, and introduced me Paul Billant, I thank to Jean-Marc Chomaz, Paul Manneville, Cristophe Clanet, Abdul Barakat, Charles Baroud, Emmanuel de Langre, Julien Husson, Lutz Lesshafft, Sebastien Michelin, Sabine Ortiz, Peter Schmid, Antoine Sellier, Carlo Cossu who was my supervisor for M2 thesis, Therese Lescuyer, Sandrine Laguerre, Delphine L'Huillier, Judith Koue Lu, Michel Paraskiova, Avin Barbataheri, Caroline Frot, Antoine Garcia, Daniel Guy, Pascal Hemon, Alexandre Rosinsky, and to my collegues, Yongyun Hwang (my korean supervisor ;)), Remi Dangla (my french life supervisor), Kiran, Clement, Sungyun, Arnaud, Jimmy, Franz, Etienne, Pierre, Cristobal, Jon, Cristophe, Diego, Joran, Fabien, Madiha, Baptiste, Caroline, Adrien, Pierre-Borice, Pascal, Xavier, Eunok, Miguel, Gianluca, Benoit, Loic, Yifan, Mathieu, Emmanuel, David, Nicolas, Guillaume, Remi, Yu Song, Elena, Gregory, Sherry, ...

I also thank to the members of the jury of my phd defense, Thierry Dauxois, Berengere Dubrulle, Bach Lien Hua, Stephane Le Dizes, Leo Maas, Riwal Plougonven.

I would like to thank to all the people that I met at Ecole Polytechnique, starting from our master programme mates, Nemanja, Vladeta, Andras, Remi, Yackar, Marco, Maylis, Prakhar, Iftikar, Hadrien, Antoine, to the Ecole Polytechnique people, Christine Ferret, Audrey Lemarechal, Ecole Doctorale people, Foot de CSX people, ...

그리고 또, 프랑스 생활하면서 만났던 모든 한국 분들께도 진심으로 감사드립니다. 우선 우리 뽈리테크닉 형동생들, 병국이 형, 창석이형, 기환형, 가현형, 종우형, 종욱형, 진우, 태하, 태우, 창현, 글고 모든 동생들 고맙고, 저 뽈리테크닉 오는데 추천서 써주신 카이스트 이덕주교수님, 박승오교수님께도 감사드립니다. 나 박사하는 동안 카톡 열심히 해준 동규, 정호, 전형도 감사하고 민수 어메 유죙 등등도 고마워. 저에게 프랑스에게 축구를 가르쳐주신 파리화랑 형 동생들, 철웅형, 원준형, 원기형, 석민형, 정완형, 동혁형, 서우 등등 모두 고마워요~ 빠리 유학동안 저에게 제 2의 가족이나 다름없던 선한교회분들, 성원용목사님과 가족분들, 종윤형, 영섭이 형네와 가족들, 유성은, 송만섭, 이군행, 구교찬, 황은옥, 방대진, 백주황, 이명연, 미선누나, 연희, 가혜, 희주, 예환, 민준이, 주봉이 주성이, 유진, 지원, 나래, 동일, 진옥누나, 손지민, 연지성 최슬기, 현겸형, 그리고 모든 분들께 감사드립니다. 그리고 우리 다민이하고 박미향 권사님도 감사합니다. 그리고 ma fiancée Da-Hee Kim 우리 다희도 너무 고마워요 나 박사과정 내내 나 외조하느라 많이 힘들었지? 사랑해요! 나 박사과정하느라 한국에서 응원해주었던 우리 엄마, 아빠, 형 사랑해요!

Contents

Chapter 1

Introduction

1 Introduction to Geophysical Fluid Dynamics

Geophysical Fluid Dynamics (GFD) is the study of large scale flows which occurs naturally in the atmosphere or in the oceans (Pedlosky, 1979; Cushman-Roisin, 1994). Large length scales L and large time scales T are one of the characteristics of geophysical flows. Interestingly, these scales are observed to be proportional to each other. For example, flows such as tornadoes with length scales of order O($1\sim 10km$) have time scales of order of days while very large scale flows such as atmospheric depression or oceanic circulations with length scales of order O($100\sim 1000km$) have time scales of order of months or years. On the other hand, velocity scale $U = L/T$ is found to be relatively invariant and is typically of order O($0.1m/s$) in the oceans or of order O($10\sim 20m/s$) in the atmosphere (Kundu & Cohen, 1990). GFD focuses mainly on flows on Earth but it also deals with flows in the atmosphere of other planets, ionized gas in stars or even in the inner part of Earth which have fluid-like properties.

GFD has attracted many attentions since environmental science became particularly important in the late 20th century. But beyond scientific interests, GFD is also important due to its social and industrial interests. For example, sea currents which enhance the mixing of temperature, salinity or nutrient elements of the oceans, affect not only physical properties of the oceans but also biological systems, weather and even climate which are closely related to humans' lives and industries such as fisheries or agricultures. Also, typhoons are formed every summer near the equator in the south-east Asia and pass through countries in the far-east Asia such as Korea, Japan or China with causing serious economical damages on these countries. There are much more examples which emphasize the importance of researches on GFD.

1.1 Physical features of geophysical flows

In contrast to classical fluid dynamics, GFD deals with peculiar physical features which originate from the dynamic properties of the Earth and introduce new phenomena that are not observed in classical fluid dynamics. Two main features are the stratification and the planetary rotation.

1.1.1 Stratification

In GFD, variations of density of the fluid need to be taken into account. Due to the gravitional force, heavy fluids rest below light fluids leading to a vertical and stable density stratification.

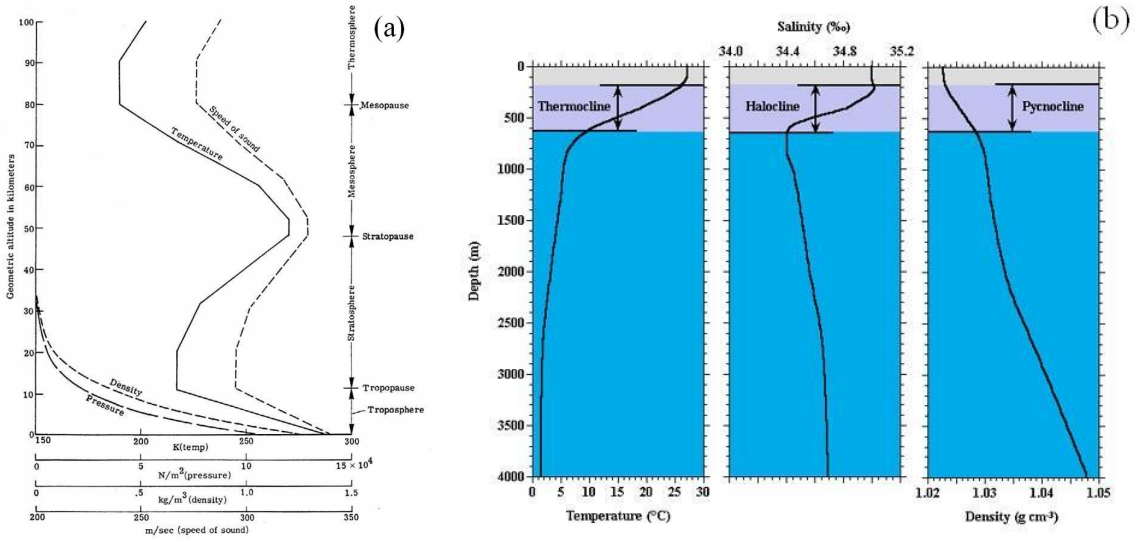

Figure 1.1: (a) Typical atmospheric variations with altitude for density, pressure, temperature and speed of sound. Source from the U.S. Standard Atmosphere in 1962, NASA. (b) Typical oceanic variations in depth for temperature, salinity and density. Source from LDEO Columbia university.

The vertical density stratification is commonly observed in the atmosphere and in the oceans, as shown in figure 1.1. Moreover, there also exists a horizontal variation of density across the latitudes due to differential heat radiation by the sun (Pedlosky, 1979). However, in this thesis, we only consider a vertical density stratification.

In the presence of a vertical density stratification, the equations of motions become more complicated but the Boussinesq approximation is commonly applied to simplify the equations. This approximation assumes that the variations of density are small compared to the mean density (called reference density). For example, density variations in the oceans are of order $\mathrm{O}(1kg/m^3)$ while the mean density is about $\mathrm{O}(1000kg/m^3)$ as shown in figure 1.1(b).

To measure a density stratification, we commonly use a parameter called the buoyancy frequency or Brunt-Väisälä frequency N, defined as

$$N^2 = -\frac{g}{\rho_0}\frac{d\rho}{dz}, \tag{1.1}$$

where g is the gravity, ρ_0 is the reference density and $d\rho/dz$ is the density gradient along the direction of stratification z. When the fluid is stably stratified with $d\rho/dz < 0$ as considered in the thesis, N^2 is positive thus N is positive and real $N > 0$. Moreover, to measure the importance of the stratification effects compared to the inertial effects, we use the Froude number defined as

$$F = \frac{U}{NL}, \tag{1.2}$$

where U is the velocity scale and L the length scale. This implies that the stratification is strong when $F << 1$ while it is negligible when $F >> 1$.

Lee wave is an example of waves in stratified fluids which we can easily observe in nature (figure 1.2a). A lee wave can be formed as the air flows over obstacles such as an island or a

mountain and can be visualized by clouds. The wave can become unstable further downstream and breaks down when its amplitude becomes sufficiently large.

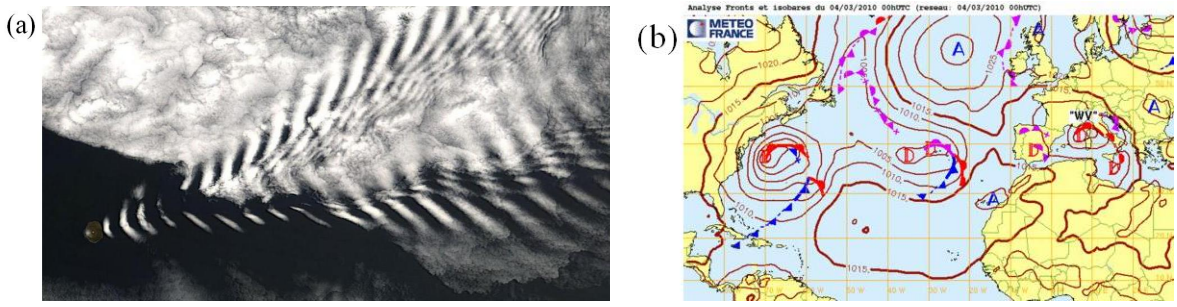

Figure 1.2: (a) Satellite image of the lee wave over Amsterdam Island in the Indian ocean, source from NASA Earth Observatory. (b) Pressure contours of cyclones (D) and anticyclones (A) in the pacific ocean, source from Meteo france.

1.1.2 Rotation

The rotation of the Earth also influences geophysical flows. Since we are fixed on the Earth when we observe the flows, we consider a rotating coordinate as a reference frame of motions. In the rotating frame, there are two additional accelerations, the centrifugal acceleration and the Coriolis acceleration. In GFD, the centrifugal acceleration is unimportant since the flattening of Earth neutralizes the effect of the centrifugal force (Cushman-Roisin, 1994). Thus, we only consider the Coriolis force. To measure the importance of the Coriolis force compared to the inertial effects, we use the Rossby number Ro defined as

$$Ro = \frac{U}{\Omega_b L} \tag{1.3}$$

where Ω_b is the angular velocity of the rotating frame. This implies that the rotation is dominant when the Rossby number is much smaller than unity $Ro << 1$ whereas it is negligible if the Rossby number is much larger than unity $Ro >> 1$.

The atmosphere and the oceans are very thin along the vertical compared to the horizontal: $L_V << L_H$. From the continuity equation, we can scale the vertical velocity W and the horizontal velocity U as $W/L_V \sim U/L_H$. Therefore, the vertical velocity W is typically much smaller than the horizontal U ($W << U$) (Kundu & Cohen, 1990; Cushman-Roisin, 1994). For this reason, only the component of the Coriolis parameter normal to the surface $f = 2\Omega_b \sin\theta$ is effective where θ is the latitude. The rate of the Earth's rotation is about $\Omega_b \sim 0.73 \times 10^{-4}(1/s)$. Beside, if the flow field is not too wide, the latitude θ varies very little so that we can assume the Coriolis parameter f as a constant. This approximation, known as the f-plane approximation, is used in this thesis. On the other hand, when we consider large scale flows such as atmospheric circulations or the flows near the equator, the variation of the Coriolis parameter is not negligible so that the f-plane approximation no longer applies but another approximation called the β-plane approximation can be used. It assumes that the Coriolis parameter varies linearly with latitude y as $f \sim f_0 + \beta y$.

Examples of flows under the strong influence of the Earth's rotation are cyclones and anticyclones (see figure 1.2b). The cyclones (anticyclones) rotate in the same (opposite) direction

as the Earth's rotation. When the size of these rotating flows is large, their turn-over frequency ($\sim U/L$) is much slower than the Earth's rotation (i.e. the Rossby number is very small as $Ro << 1$) and we can apply the geostrophic approximation. Under this approximation, we obtain a simple expression for the velocity field (u, v) in the horizontal plane (x, y) as

$$u = \frac{-1}{f\rho}\frac{\partial p}{\partial y} \ , \ v = \frac{1}{f\rho}\frac{\partial p}{\partial x}, \tag{1.4}$$

where ρ is the density and p is the pressure. We see that the velocity vector (u, v) is orthogonal to the horizontal pressure gradient $(\partial p/\partial x, \partial p/\partial y)$. This implies that for positive f (i.e. in the Northern Hemisphere), a cyclone is formed around a low pressure region while an anticyclone is formed around a high pressure region. This is opposite in the Southern Hemisphere. These cyclones and anticyclones have significantly different weather patterns since the cyclones lead to accompany a lot of clouds and rains whereas the weather is very clear in the anticyclones.

1.2 Typical motions in geophysical flows

1.2.1. Waves

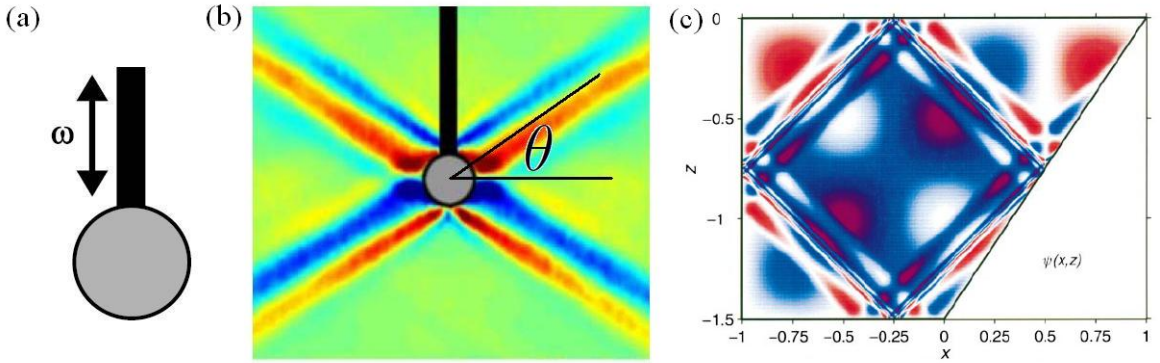

Figure 1.3: (a),(b): A vibrating cylinder with frequency ω in a stratified fluid. Gravity wave beams captured with a synthetic Schlieren technique (Gostiaux *et al.*, 2007). (c): Wave attractors focused by internal waves confined in a vibrating container with a continuously stratified fluid (Maas *et al.*, 1997)

Waves have been widely studied since they are widespread and play a very important role in geophysical flows. They are typically generated by the combined effects of the density stratification and the rotation. For example, when perturbations are applied in a stably stratified fluid, they return to their original positions due to a restoring buoyancy force. This generates waves known as the gravity or internal waves. Many laboratory experiments on internal waves have been performed (Mowbray & Rarity, 1967; Maas *et al.*, 1997; Gostiaux *et al.*, 2007). For example, by vibrating a cylinder with frequency ω in a stratified fluid with constant N (figure 1.3a), wave beams are generated with an angle θ from the horizontal (figure 1.3b). We can explain this theoretically by writing a wave solution in the form $e^{i(k_x x + k_y y + k_z z - \omega t)}$ where k_x, k_y, k_z are the wavenumbers in x, y, z directions. The dispersion relation then reads $\omega^2 = N^2 \sin^2\theta$ in the inviscid limit, where θ is the angle of the wave vector $\vec{k}$ with the vertical. This implies that the wave beams can be observed when the vibration frequency ω is less than

the Brunt-Väisälä frequency N (i.e. $|\omega| < N$). The group velocity vector, which represent the direction of the energy propagation, is along the wave beam direction θ while the phase velocity vector is perpendicular to the group velocity which agrees very well with observations in experiments. Interestingly, internal waves conserve their angle $|\theta|$ when N is constant so that when they reflect from a boundary, the angle $|\theta|$ does not change regardless of the geometry of the boundary. As a result, when internal waves are generated in a vibrating container of a stratified fluid as in figure 1.15(c), they accumulate after several reflections and form wave attractors which are responsible for mixing properties of the oceans (Maas *et al.*, 1997).

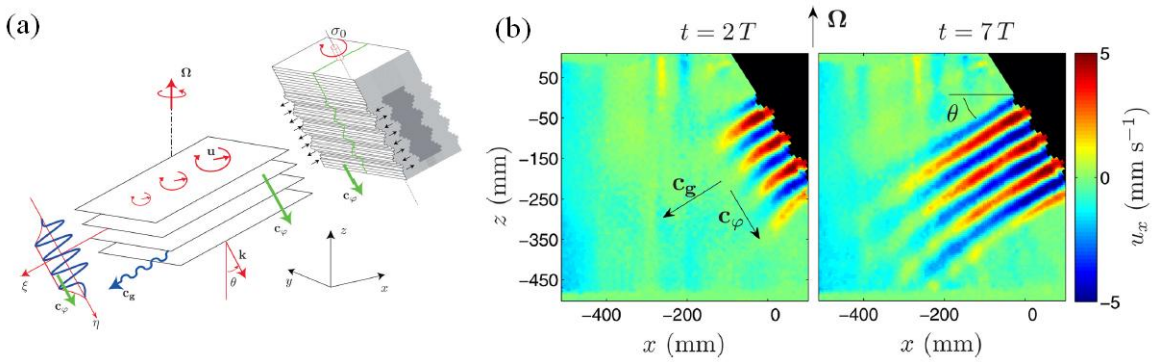

Figure 1.4: (a) Experimental set-up of an inertial wave generator in a rotating fluid (b) Time evolution of inertial wave propagation. Figures are from Bordes *et al.* (2012).

Waves can be also generated in a fluid rotating with angular velocity Ω_b, known as the inertial waves (figure 1.4a,b). In this case, the Coriolis force plays the role of the restoring force. Inertial waves satisfy the dispersion relation $\omega^2 = 4\Omega_b^2 \cos^2\theta$ so that the wave exists only if $|\omega| < 2\Omega_b$ (Batchelor, 1967; Cortet *et al.*, 2010; Bordes *et al.*, 2012). More generally, waves in a stratified and rotating fluid, known as inertia-gravity waves, satisfy the dispersion relation

$$\omega^2 = N^2 \sin^2\theta + 4\Omega_b^2 \cos^2\theta. \tag{1.5}$$

This implies that the inertia-gravity waves exist only when the frequency ω lies in the range $2\Omega_b < |\omega| < N$ if $N^2 > 4\Omega_b^2$; otherwise $N < |\omega| < 2\Omega_b$ if $N^2 < 4\Omega_b^2$ (see also Peacock & Weidman, 2005). An example of inertia-gravity waves visualized by clouds in the atmosphere is shown in figure 1.5(a).

Another example of waves in geophysical flows is the Rossby waves. These waves can appear as a result of the variations of the Coriolis parameter f in latitude. The β-plane approximation is typically considered for the Coriolis parameter f

$$f = 2\Omega_b \sin\phi \sim f_0 + \beta_0 y, \tag{1.6}$$

where $f_0 = 2\Omega_b \sin\phi_0$ is the reference Coriolis parameter at the latitude ϕ_0 and y the northward coordinate at the latitude ϕ_0. Under this approximation and for the shallow-water equations, we obtain a dispersion relation for the Rossby waves as

$$\omega = -\beta_0 R_{ro}^2 \frac{k_x}{1 + R_{ro}^2(k_x^2 + k_y^2)}, \tag{1.7}$$

where $R_{ro} = \sqrt{gH}/f_0$ is the Rossby radius of deformation with H the depth of the fluid. Note that the frequency ω is now of order $\mathrm{O}(\beta_0)$ which is much smaller than the Coriolis parameter

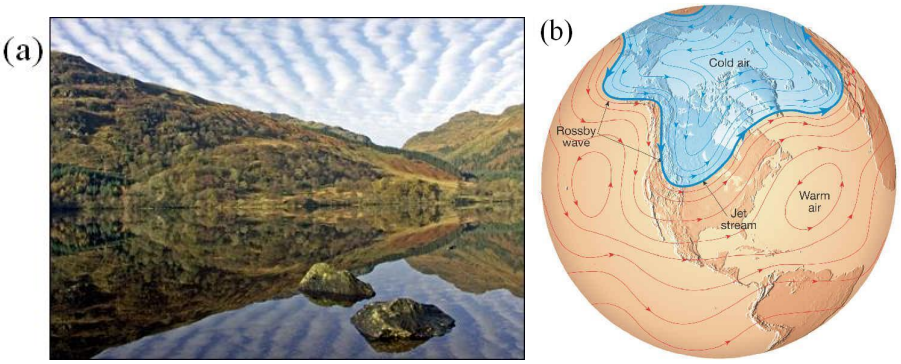

Figure 1.5: (a) Atmospheric inertia-gravity waves visualized by clouds, photo from the BBC news Scotland (b) Atmospheric Rossby wave evidenced by five long-wavelength undulations of the jet stream, source from Department of Geography and computer science, CUNY.

f_0. These slow waves appear as meanders of the jet stream with a large wavelength (figure 1.5b).

1.2.2. Geophysical vortices

Vortices are frequently observed in nature and their dynamics is an important topic in GFD. The geophysical vortices typically have velocity U of order $O(10m/s)$ in the atmosphere and of order $O(0.1m/s)$ in the oceans (Kundu & Cohen, 1990) but their horizontal sizes L_H can vary largely between $O(100m \sim 1000km)$. Thus, their Rossby numbers are strongly correlated with their length scales (Cushman-Roisin, 1994). For example, large scale vortices such as typhoons (figure 1.6a), which have radii of order $O(100 \sim 1000km)$ generally have Rossby numbers much less than unity $Ro << 1$ corresponding to the quasi-geostrophic regime where the Coriolis force is dominant. On the other hand, small scale vortices such as tornadoes with radii of order $O(100m \sim 1km)$ (figure 1.6b), typically have Rossby numbers much larger than unity $Ro >> 1$ so that the effect of the Earth's rotation (i.e. the Coriolis force) is negligible.

There also exist mesoscale vortices such as intense tropical cyclones, polar lows or island wake vortices (figure 1.6c) which have length scales of order O(10∼100km). They have Rossby numbers of order of unity $Ro \sim O(1)$ and the quasi-geostrophic approximation is no longer applicable. As a consequence, mesoscale vortices have a more complicated dynamics. For example, mesoscale vortices can sustain a gravity wave emission which is neglected in the quasi-geostrophic approximation. Such wave emission may trigger spiral bands outside the vortex core (Chow *et al.*, 2002; Schecter & Montgomery, 2006; Schecter, 2008). Various kinds of geophysical vortices are summarized in figure 1.6(d) depending on their Froude and Rossby numbers (Schecter & Montgomery, 2006) .

Moreover, there are also anticyclonic vortices such as the Mediterranean eddies (Meddies) which have negative Rossby numbers in the range $-1 < Ro < 0$. The Meddies are formed as the saltier Mediterranean seawater enters the Atlantic ocean. Initially, it is a tongue-shaped undercurrent and it changes its direction toward the gulf of Cadiz due to the Coriolis force (Bower *et al.*, 1997). Then, it transforms to pancake-shape vortices (McWilliams, 1985; D'Asaro, 1988). Due to the restrictions on vertical motions by the stratification, the Meddies have horizontal length scales of order $O(50 \sim 100km)$ while they have much smaller vertical length scales of order $O(500m \sim 1km)$ (figure 1.7). The Meddies play a significant role of

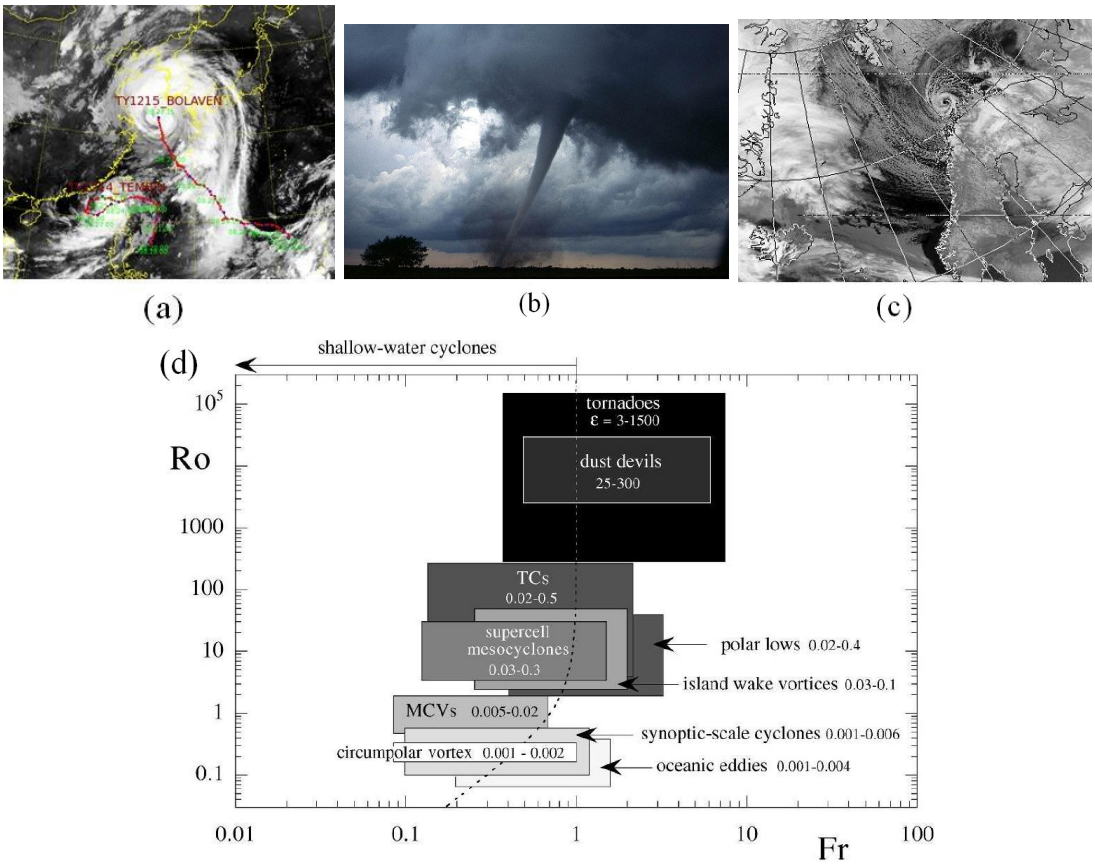

Figure 1.6: (a) Typhoon Bolven and Tembin, satellite image taken in summer 2012, source: Korea Meteorological Administration. (b) A tornado observed in central Oklahoma in 1999, source from NOAA's National Severe Storms Laboratory. (c) A polar low near northern Norway, source: World Climate Report (d) Geophysical vortices and corresponding Rossby number and Froude number (Schecter & Montgomery, 2006).

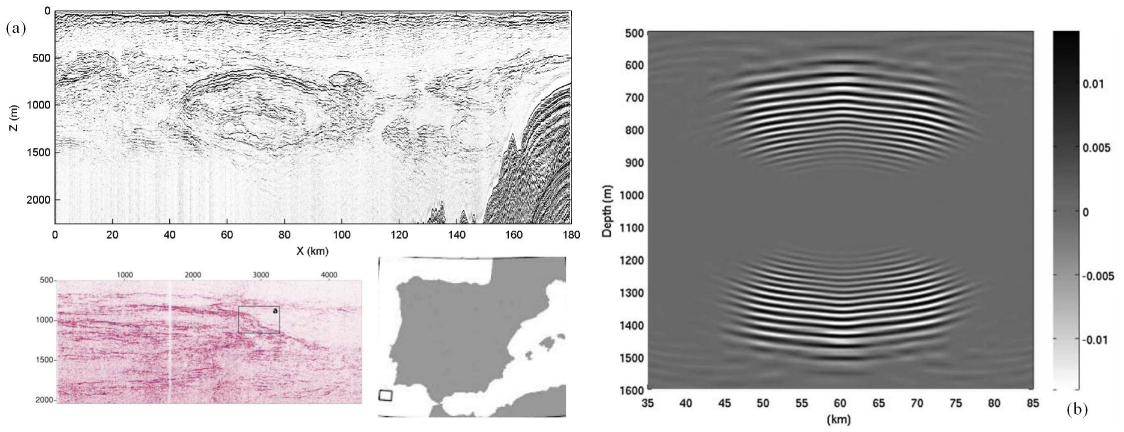

Figure 1.7: (a) High resolution seismic images of the Mediterranean eddy in the Gulf of Cadiz during the GO experiment (courtesy of D. Klaeschen & C. Papenberg, see also Geli *et al.*, 2009). (b) Numerical simulation of an anticyclonic eddy (Ménesguen *et al.*, 2009).

mixing since they affect largely the salinity of the Atlantic ocean.

1.2.3. Instabilities

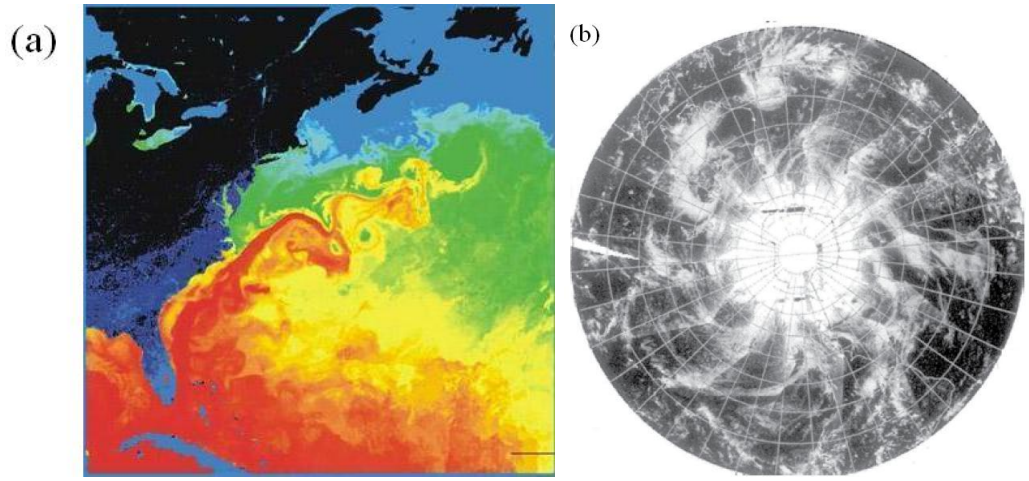

Figure 1.8: (a) Surface temperature on the Gulf stream (red: warm, blue: cold), source from NASA. (b) Tropospheric clouds with meanders over antartica (Nadiga & Aurnou, 2008)

Instabilities in geophysical flows is also an important subject in GFD since they are very common. An example of instabilities observed in the Gulf stream is shown in figure 1.8. As warm water of the Gulf stream mixes with cold water, an instability appears and forms vortices. This resembles the Kelvin-Helmholtz instability. These vortices have an important role since they generate mixing of the oceans.

In GFD, barotropic and baroclinic instabilities are considered as two basic forms of instabilities. Strictly speaking, the definitions of the terms barotropic and baroclinic are such that a flow is barotropic if p/ρ^γ is constant where γ is the ratio of specific heats of a gas, while it is baroclinic if p/ρ^γ is not constant. This implies that the pressure gradient is not aligned with the density gradient when it is baroclinic. However, in the GFD context, an instability is generally called barotropic if it is two dimensional and baroclinic if it is three dimensional.

Stability conditions are already well established especially for classical inviscid shear flows. A necessary condition for instability of an inviscid flow with velocity profile $U(y)$ is that there exists an inflection point in the profile (i.e. $d^2U/dy^2 = 0$), known as the Rayleigh's inflection point criterion. When the Coriolis parameter varies $f = f_0 + \beta_0 y$, the Rayleigh's criterion is slightly modified such that a necessary condition for instability is that there exists a point where $\frac{d^2U}{dy^2} = \beta_0$ (Kuo, 1949). This barotropic instability is possibly responsible for the instability of currents in the oceans and in the atmosphere (Kundu & Cohen, 1990).

The baroclinic flow configuration, where pressure gradient is not aligned in the direction of density gradient, is common on the Earth due to the differential sun radiation along latitude. In this case, the density increases with latitude while decreasing with altitude so that the isodensity surfaces are inclined. By assuming the geostrophic and hydrostatic balances (i.e. the balance between pressure gradient and the density), the equations of motions give

$$\frac{\partial u}{\partial z} = \frac{g}{\rho_0 f}\frac{\partial \rho}{\partial y}\ , \ \frac{\partial v}{\partial z} = -\frac{g}{\rho_0 f}\frac{\partial \rho}{\partial x}, \tag{1.8}$$

where ρ_0 is the reference density. This is known as the thermal wind equation. We see that the horizontal velocity field (u, v) varies along the vertical z when there exists a horizontal density gradient $\left(\frac{\partial \rho}{\partial x}, \frac{\partial \rho}{\partial y}\right)$. Inclined isodensity surfaces contain more potential energy than horizontal isodensity surfaces so that the potential energy can be converted to the kinetic energy by parallelising the density gradient and the pressure gradient (Kundu & Cohen, 1990). This is the mechanism of the baroclinic instability. An example of baroclinic instability is shown in figure 1.8(b). Cold air in the antartica surrounded by warm air spreads out towards lower latitude due to the density gradient, and spiraling eddies are formed as visualized by tropospheric clouds (Nadiga & Aurnou, 2008).

1.2.4. Turbulence

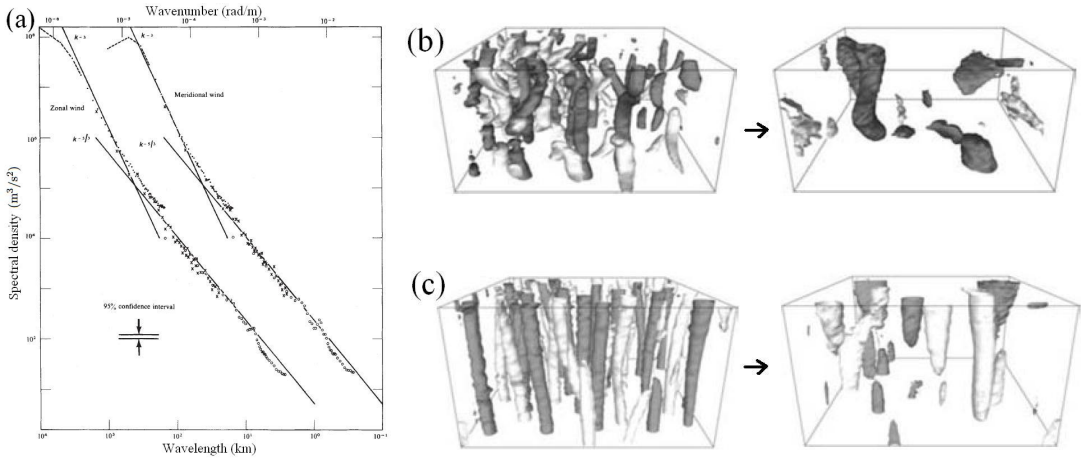

Figure 1.9: (a): Kinetic energy spectrum from the data obtained near the tropopause (Nastrom *et al.*, 1984). (b),(c): Evolution of the three dimensional turbulent structures of the vertical vorticity in quasigeostophic flows when (b) the stratification is dominant and (c) the rotation is dominant (Praud *et al.*, 2006).

Geophysical flows have relatively large length scales of order O(1∼1000km), and their Reynolds numbers $Re = UL/\nu$ (ν is the dynamic viscosity) are thus very large. As a consequence, turbulence in geophysical flows is a very common feature. A distinguishable feature of geophysical turbulence is that the turbulence is affected by the strong stratification and rotation so that it is significantly different from classical turbulence in homogeneous fluids. In stratified and rotating fluids, velocity fields become quasi-horizontal due to the restriction on vertical velocity by the rotation and the stratification, and also due to the small vertical length scale. In classical turbulence, energy transfers towards small length scales (forward energy cascade) and dissipates by viscosity at very small length scales, known as the Kolmogorov length scale. The forward energy cascade has a $-5/3$ power law dependence. In contrast, the two-dimensional quasi-geostrophic turbulence has an inverse energy cascade where the energy transfers towards large scales and the dissipation by viscosity becomes negligible (Charney, 1971). This inverse energy cascade comes from the conservation of enstrophy (i.e. the mean square vorticity) and in contrast to the inverse energy cascade, the enstrophy has a foward cascade such that it transfers towards small length scales and dissipates by viscosity at very

small scales. The forward enstrophy cascade has a -3 power law dependence and it has been detected in nature as shown in figure 1.9(a) when the flow is quasi-geostrophic (i.e. strong rotation $Ro << 1$ and stratification $F << 1$).

In figure 1.9(a), we see that the value of power in spectral density changes from -3 to -5/3 when length scales are below $O(500km)$. This is because the Rossby number becomes large as $Ro >> 1$ in this meso-scale range. However, the stratification remains strong $F << 1$ in this range and recent works on stratified turbulence have shown that there is a forward energy cascade with a -5/3 slope and the turbulent structures are layered (figure 1.9b and Praud *et al.*, 2006).

1.3 Waves and instabilities on vortices

1.3.1. Vortices

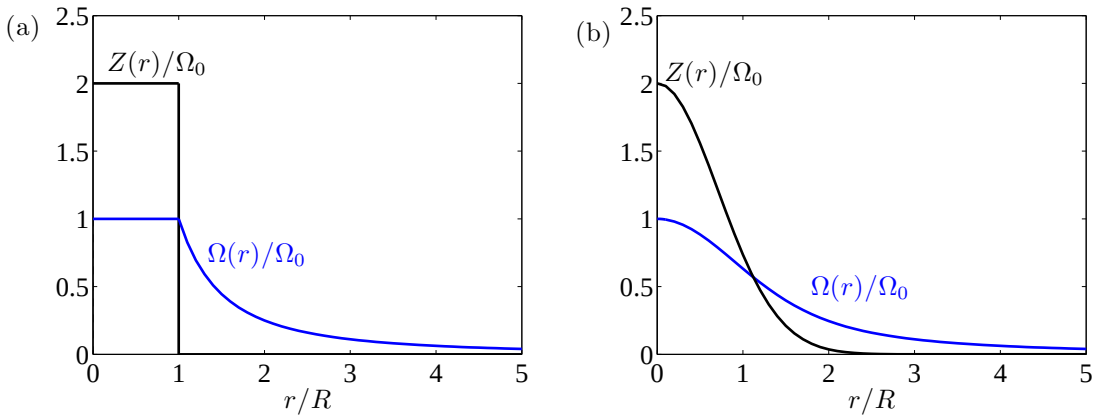

Figure 1.10: Profiles of vorticity $Z(r)$ (black) and angular velocity $\Omega(r)$ (blue) as a function of r for (a) the Rankine vortex and (b) the Lamb-Oseen vortex. The vorticity and the angular velocity are normalized by the angular velocity Ω_0 at the center $r = 0$ and the radius by the radius of the vortex core R

Vortices are flows in circular motions and they have been studied since centuries not only in fluid mechanics but also in physics, engineering or mathematics (Saffman, 1992). One of the simplest examples of vortices is the Rankine vortex. The Rankine vortex is a solution of the Euler equation and it has profiles of angular velocity $\Omega(r)$ and vorticity $Z(r) = \frac{d}{dr}(r^2\Omega)$ as follows:

$$\Omega(r) = \Omega_0, \quad Z(r) = 2\Omega_0, \quad \text{if} \quad r < R, \tag{1.9a}$$

$$\Omega(r) = \Omega_0 \frac{R^2}{r^2}, \quad Z(r) = 0, \quad \text{if} \quad r > R, \tag{1.9b}$$

where Ω_0 is the angular velocity at the vortex centre $r = 0$ and R the radius of the vortex core. The fluid elements in the vortex core rotate like a solid, while the motion outside the core is irrotational (Kundu & Cohen, 1990). Figure 1.10(a) shows the profiles (1.9) of the Rankine vortex. Note that there is a vorticity jump at $r = R$ for the Rankine vortex. Although this is not realistic, the Rankine vortex is used as a convenient model in vortex dynamics due to its simplicity.

While the Rankine vortex is only a solution of the inviscid equations, there exists an exact solution of the Navier-Stokes equations, the Lamb-Oseen vortex, which has profiles as

$$\Omega(r) = \frac{\Gamma_0}{2\pi r^2}\left(1 - \exp\left(-\frac{r^2}{R^2}\right)\right), \quad Z(r) = \frac{\Gamma_0}{\pi R^2}\exp\left(-\frac{r^2}{R^2}\right), \tag{1.10}$$

where Γ_0 is the initial vortex circulation, $R = \sqrt{4\nu t + R_0^2}$ the vortex core radius, R_0 is the initial core radius and ν is the kinematic viscosity. The vortex core R grows in time due to viscous effects. These profiles are plotted in figure 1.10(b) normalized with the angular velocity at the center $\Omega_0 = \Gamma_0/(2\pi R^2)$. The Lamb-Oseen vortex has been used as a more realistic model to describe the decay of trailing vortices (Saffman, 1992; Batchelor, 1964).

Many other vortex profiles also exist. For example, the Batchelor vortex considers a flow in axial direction and it has been used to study realistic aircraft trailing wakes. Another example is an isolated vortex with a Gaussian streamfunction (Gent & McWilliams, 1986). While these vortices are all columnar, geophysical vortices such as the Meddies have generally a pancake shape. However in this thesis, only columnar monotonic vortices, whose vorticity decreases monotonically with r (i.e. $Z' < 0$), will be studied.

1.3.2. Waves on vortices

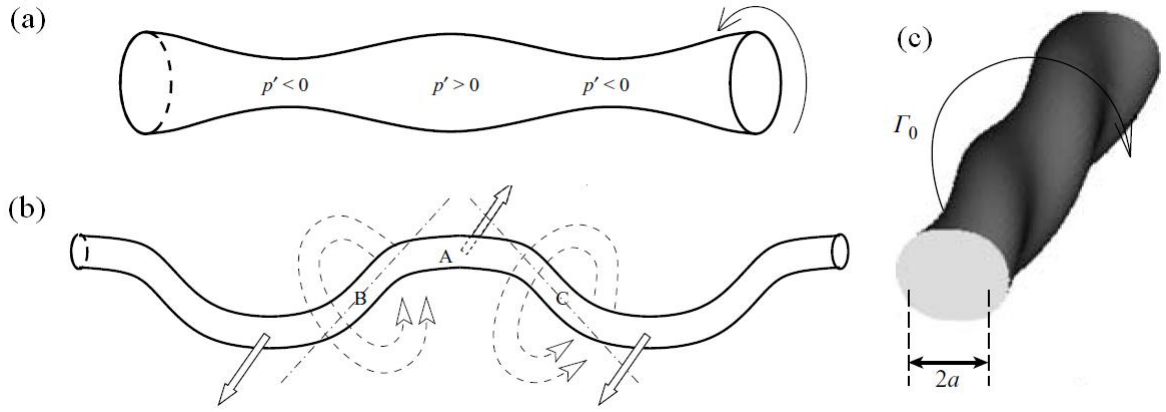

Figure 1.11: The vortex Kelvin waves for the azimuthal wavenumber (a) $m = 0$: axisymmetric mode, (b) $m = 1$: displacement mode and (c) $m \geq 2$: helical mode, figures from Fabre *et al.* (2006).

Waves on vortices have been first studied by Lord Kelvin (Kelvin, 1880). He performed a stability analysis with the Rankine vortex as a base flow. He found that there exist travelling waves along the vortex core, now known as the vortex Kelvin waves. These waves are inertial waves sustained by the rotation of the vortex core, and they are neutral for the Rankine vortex. Depending on the azimuthal wavenumbers m, there are different types of modes. For example, when the wave is axisymmetric ($m = 0$), the vortex core undulates (figure 1.11a) while for $m = 1$, the vortex core is sinusoidally displaced (displacement mode, see figure 1.11b). For larger azimtuthal wavenumbers $m \geq 2$, the core is twisted in the axial direction (helical mode, see figure 1.11c). These waves play an important role since, for example, turbulent energy can be transferred by the propagation of vortex Kelvin waves (Hopfinger *et al.*, 1982).

More recently, Kelvin waves have been thoroughly studied in the case of the Lamb-Oseen vortex (Fabre *et al.*, 2006). The modes are similar to those of the Rankine vortex except that some are singular and damped. Other types of stability analysis such as the transient growth (Antkowiak & Brancher, 2004; Pradeep & Hussain, 2006) or the stochastic forcing (Fontane *et al.*, 2008) have been performed for the Lamb-Oseen vortex.

1.3.3. Vortex instabilities

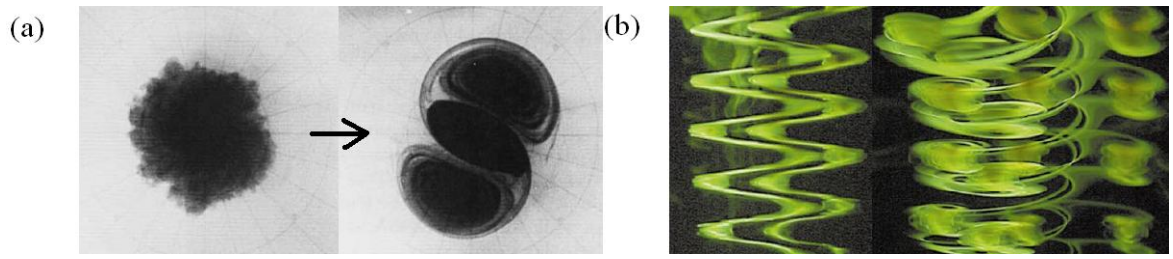

Figure 1.12: (a) Evolution of a cyclonic barotropic vortex destabilized by the centrifugal instability (Kloosterziel & van Heijst, 1991) (b) Frontal (left) and side (right) views of a pair of counter-rotating vortices destabilized by the zig-zag instability (Billant & Chomaz, 2000*a*)

Many studies have been devoted to vortex instabilities. Although columnar vortices such as the Rankine vortex or the Lamb-Oseen vortex are not linearly unstable, they can become unstable by introducing additional effects. For example, instabilities such as the Crow instability or the elliptic instability occur when a strain field is applied (Kerswell, 2002; Lacaze *et al.*, 2005). The Crow instability is a long wavelength instability which occurs on trailing vortices behind an aircraft, when a pair of counter-rotating vortices is shed from the wings and interacts each other by its strain field (Crow, 1970). On the other hand, the elliptic instability has a much shorter wavelength and induces a deformation of the vortex core (Meunier & Leweke, 2005).

A vortex can also be destabilized by the centrifugal instability (figure 1.12a). The centrifugal instability occurs when there exists a radius where the square of the vortex circulation $\Gamma^2 = (r^2\Omega)^2$ decreases in the radial direction (i.e. $\phi = \frac{1}{r^3}\frac{d\Gamma^2}{dr} = 2\Omega Z < 0$) leading to an unstable balance between the centrifugal force and the pressure gradient. In rotating fluids with the angular velocity Ω_b (Kloosterziel & van Heijst, 1991), the criterion is modified to $\phi(r) = (2\Omega_b + 2\Omega)(2\Omega_b + Z) < 0$. For example, the Rankine vortex becomes unstable if the background rotation lies in the range $-\Omega_0 < \Omega_b < 0$ (i.e. the Rossby number $Ro = \Omega_0/\Omega_b$ is in the range $Ro < -1$).

The presence of stable density stratification in vertical direction can triger instabilities as well. In particular, the stratification can destabilize the vortex owing to the inertia-gravity waves (Ford, 1994; Schecter & Montgomery, 2004; Billant & Le Dizès, 2009; Le Dizès & Billant, 2009). This instability, known as the radiative instability, will be discussed in the following section. Moreover, for a pair of counter-rotating vortices in a stratified fluid, the Crow instability disappears but a new instability known as the zig-zag instability occurs (Billant & Chomaz, 2000*a*,*b*). Due to the zig-zag instability, the vortex pair is sliced and forms pancake-shaped dipoles (figure 1.12b).

2 Objectives of the thesis

In this thesis, two types of instabilities will be studied: the radiative instability of columnar vortices in stratified and rotating fluids, and the stratorotational instability of stratified Taylor-Couette flow.

2.1 Radiative instability

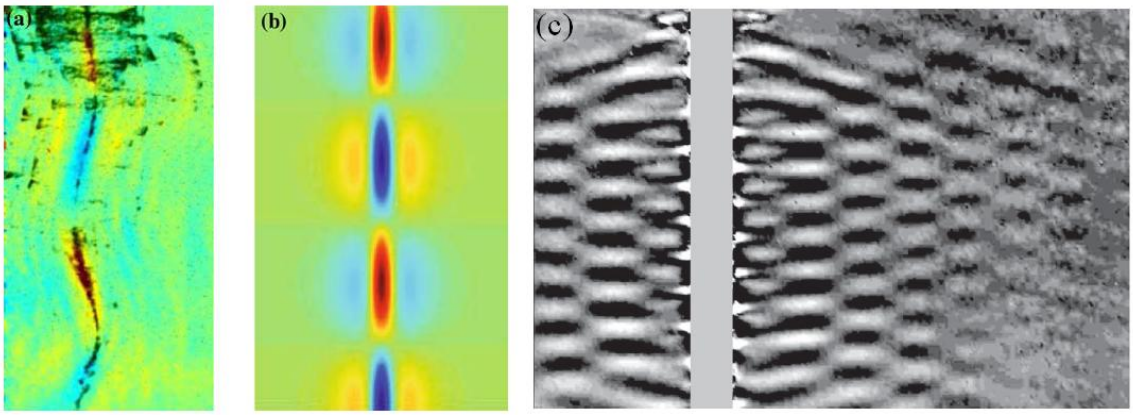

Figure 1.13: (a) Experimental and (b) numerical results showing the density gradient for the radiative instability of a columnar vortex in a stratified fluid (Riedinger *et al.*, 2010a). (c) Experimental visualisation of the radiative instability of the flow around a rotating cylinder in a stratified fluid (Riedinger *et al.*, 2011).

For columnar vortices in stratified fluids, there exists an instability called the radiative instability. The instability is named radiative since it involves a radiation of waves. For example, the radiative instability is found when there is an acoustic wave emission in compressible fluids (Miles, 1957; Broadbent & Moore, 1979) or when gravity waves propagate in shear flows or in shallow water flows (Jones, 1968; Lindzen *et al.*, 1980; Lindzen & Barker, 1985; Takehiro & Hayashi, 1992). Numerical stability analyses of columnar vortices in stratified fluids have shown that the radiative instability occurs due to gravity wave emission from the vortex core and it has been confirmed numerically (Schecter & Montgomery, 2004, 2006; Schecter, 2008; Billant & Le Dizès, 2009; Le Dizès & Billant, 2009). Moreover, experiments on the flow around a rotating cylinder in a stratified fluid have also given an evidence for the radiative instability (figure 1.13c and Riedinger *et al.*, 2011).

The mechanism of destabilization by a wave radiation has been explained in the case of an wave packet propagating in a inviscid shear flow $U(y)$ of the shallow water system (Takehiro & Hayashi, 1992). If there exists a critical point y_c (figure 1.14a) where the mean flow velocity equals to the phase velocity c of the wave $U(y_c) = c$, an inviscid equation for the wave becomes singular and there is an interaction between the mean flow and the wave, so that the wave can extract energy from the mean flow (Acheson, 1976). As the incident wave penetrates through the critical point, the wave momentum (i.e. the wave energy divided by the relative phase speed) changes its sign so that the transmitted wave has a negative wave momentum (figure 1.14a). In order to conserve the total wave momentum, there must be a reflected wave with a larger amplitude than the incident wave. This is called the over-reflection (Miles, 1957;

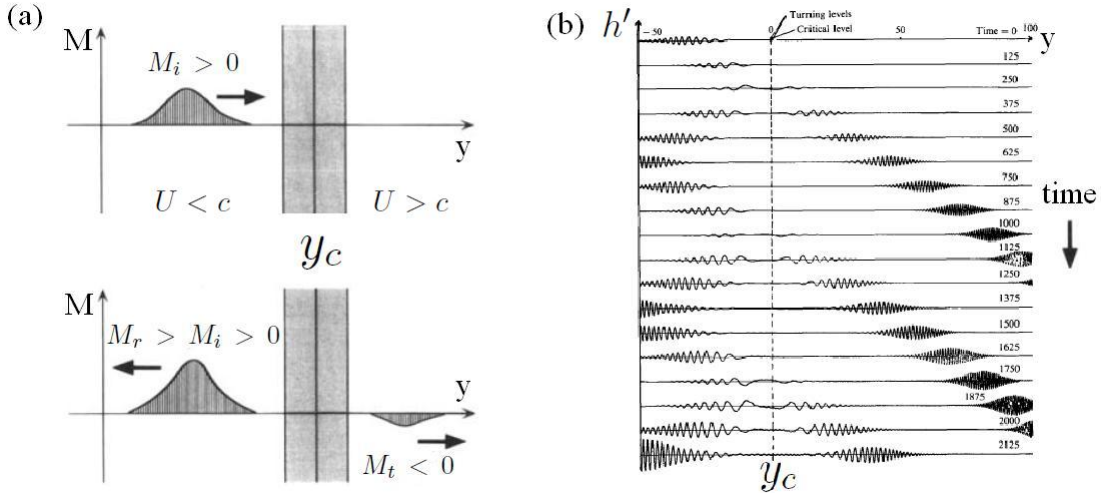

Figure 1.14: (a) Schematic pictures of an incident wave propagating towards the critical point. After hitting the critical point, the transmitted wave has negative momentum and the reflected wave is amplified, i.e. over-reflected whereas the total wave momentum M is conserved. (b) Multiple over-reflection processes. Figures are reproduced from Takehiro & Hayashi (1992).

Acheson, 1976; Lindzen *et al.*, 1980; Lindzen & Barker, 1985; Takehiro & Hayashi, 1992). Lindzen and his coworkers summarized necessary conditions for existence of the radiative instability. In order to have the radiative instability, there must be a critical point enclosed by two wavelike regions, the first wavelike region with one boundary and the second wavelike region without boundary, and the over-reflection must be supported in the first region between the boundary and the critical point as illustrated in figure 1.14(b). As the incident wave is over-reflected at the critical point, the reflected wave reflects again at the boundary and it propagates again toward the critical point leading to multiple over-reflections (Takehiro & Hayashi, 1992). Hence, the wave energy grows in time as the over-reflection continues and this is the origin of the radiative instability.

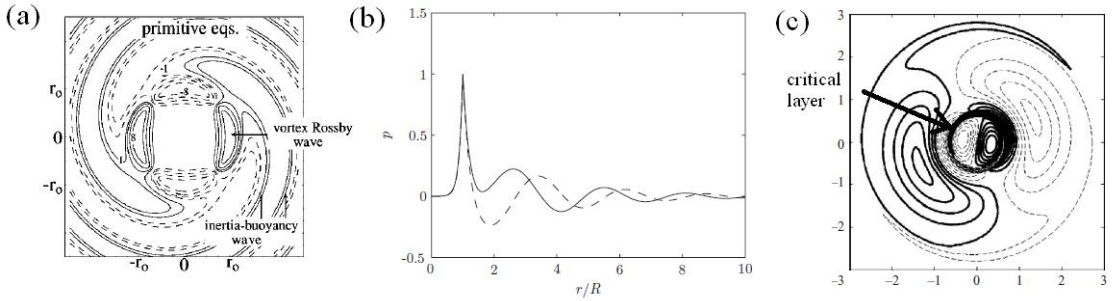

Figure 1.15: (a) Inertia-gravity wave emission from the vortex core in horizontal plane for the helical mode $m = 2$ (Schecter & Montgomery, 2004) (b) Pressure eigenfunction in radial direction showing the inertia-gravity wave emission (Billant & Le Dizès, 2009) (c) Inertia-gravity wave emission with the critical layer for the Lamb-Oseen vortex for the displacement mode $m = 1$ (Riedinger *et al.*, 2010b)

For the case of columnar vortices in stratified fluids, the vortex Kelvin waves are not confined to the vortex core but exist outside owing to the stratification. These waves are clearly visible in figure 1.15(a) and (b). Similar as the waves in shear flows, there is also a critical point r_c where the angular phase velocity equals to the angular velocity of the vortex (i.e. $\omega/m = \Omega(r_c)$ where ω is the frequency of the wave and m the azimuthal wavenumber) and this critical point r_c reverses the sign of the wave angular momentum so that the inertia-gravity wave has a negative angular momentum (Schecter & Montgomery, 2004), leading to over-reflection and the radiative instability (Billant & Le Dizès, 2009; Le Dizès & Billant, 2009). This radiative instability on columnar vortices is important since it is source of gravity waves (Riedinger *et al.*, 2010a). However, it disappears in the presence of strong viscous effects (Riedinger *et al.*, 2010b).

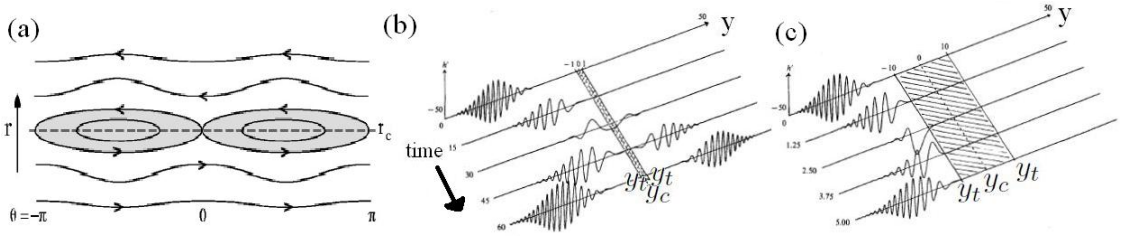

Figure 1.16: (a) Kelvin's cats' eyes pattern around the critical point r_c showing the mixing of the vorticity due to the perturbation (Schecter *et al.*, 2000). (b), (c): Example of waves passing through the potential barrier for (b) over-reflection with small potential barrier (shaded) and (c) perfect reflection with large potential barrier (Takehiro & Hayashi, 1992)

The radiative instability can be stabilized by the critical point. While the presence of the critical point is essential for the radiative instability (figure 1.15c), it can also have a stabilizing effect. Figure 1.16(a) shows an interaction between the vortex and the perturbation around the critical point. Due to the interaction, the angular momentum of the base flow is mixed with that of the perturbation. When the vorticity gradient is negative $Z_c' < 0$ (the case for monotonic vortices considered in this thesis), the perturbation mixes higher vorticity of the base flow inside the critical point $r < r_c$ with lower vorticity of the base flow outside the critical point $r > r_c$. This vorticity mixing leads to an increase of the angular momentum of the base flow so that the perturbation must lose its angular momentum in order to conserve the total angular momentum. As a result, the stabilization of the perturbation occurs (Schecter *et al.*, 2000; Le Dizès, 2000). Nonetheless, the radiative instability can still occur when the destabilizing effect of the wave emission is stronger than the damping at the critical point (Schecter & Montgomery, 2004, 2006; Schecter, 2008).

The presence of the potential barrier also stabilizes the radiative instability. The potential barrier is a region around the critical point where solutions are no longer wavelike but evanescent. It reduces the wave emission outside the critical point (figure 1.16b) which implies that the incident wave is less over-reflected so that the radiative instability is weaker. For a large potential barrier, the penetration of the incident wave is very small (figure 1.16c) and there is almost no instability in this case. This effect of the potential barrier is also called the tunnelling effect for the radioactive decay of bounded states in quantum mechanics (Bender & Orszag, 1978; Le Dizès & Billant, 2009).

In this thesis, we will investigate the radiative instability of a columnar vortex in stratified

and rotating fluids. We shall see that the background rotation has a stabilizing effect on the radiative instability by enlarging the potential barrier. In contrast, an anticyclonic rotation larger or equal to the angular velocity in the vortex core triggers the radiative instability.

2.2 Stratorotational instability

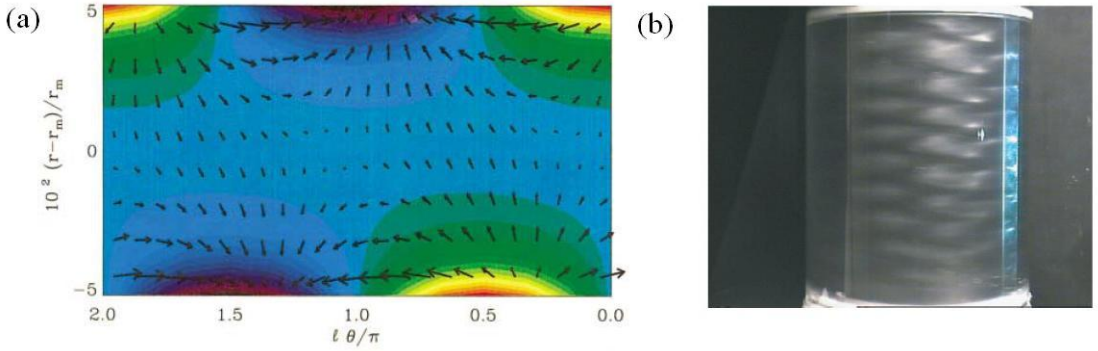

Figure 1.17: (a) Two boundary modes. Vectors represent the horizontal velocity and contour plots in color represent the vertical velocity (Molemaker *et al.*, 2001). (b) Kalliroscope visualization of the stratorotational instability in the vertically stratified salt water (Le Bars & Le Gal, 2007).

The stratorotational instability (SRI) is an instability of the Taylor-Couette flow which appears if the fluid is stratified. It occurs outside the regime of the centrifugal instability: $\mu \geq \eta^2$ where $\mu = \Omega_o/\Omega_i$ and $\eta = r_i/r_o$ are the ratios of the angular velocities and the radii of the inner and outer cylinders. Molemaker *et al.* (2001); Yavneh *et al.* (2001) have shown that the SRI exists in the regime $\eta^2 \leq \mu < 1$ in inviscid fluids. The instability is due to a resonance between two boundary waves which exist in the presence of density stratification. These waves are trapped near the cylinders by the shear of the mean flow (figure 1.17a). The SRI has been observed in viscous fluids in both numerical studies (Shalybkov & Rüdiger, 2005) and experiments (Le Bars & Le Gal, 2007). As shown in figure 1.17(b) of the experiment by Le Bars & Le Gal (2007), the SRI is non-axisymmetric unlike the centrifugal instability which forms axisymmetric vortices known as the Taylor vortices (Andereck *et al.*, 1986).

The stratorotational instability of the stratified Taylor-Couette flow has been shown to be related to the radiative instability by Le Dizès & Riedinger (2010). In this thesis, we will investigate the stability of the Taylor-Couette flow in the regime $\mu > 1$. We shall show that it is unstable to the SRI.

3 Structure of the thesis

In chapter 2, the numerical and asymptotic methods used to investigate the linear stability of the different basic flows are presented. In chapter 3, the stability of the Rankine vortex in a strongly stratified and rotating fluid is investigated. This chapter focuses on the effect of a cyclonic rotation but the effect of a weak anticyclonic rotation is also presented to describe the competition between the radiative instability and the centrifugal instability. The stability of a smoothed Rankine vortex and the Lamb-Oseen vortex are also investigated briefly.

In chapter 4, the stability of the Rankine vortex in the regime $-1 \leq Ro < 0$ is investigated. We show that the radiative instability also occurs in this range. The stability of the stratified Taylor-Couette flow in the regime $\mu > 1$ is also investigated in this chapter since this regime is analogous to the regime $-1 \leq Ro < 0$ for a vortex. In chapter 5, conclusions and discussions are established. The appendix presents some validations of the numerical codes.

Chapter 2

Problem formulation

1 Equations of motions under the Boussinesq approximation

In this section, we present the equations of motions under the Boussinesq approximation that are commonly used in geophysical fluid dynamics. In the reference frame rotating about the vertical axis with an angular velocity $\Omega_b = f/2$ where f is the Coriolis parameter, the continuity, the momentum and the density equations are

$$\frac{1}{\hat{\rho}}\frac{D\hat{\rho}}{Dt} + \vec{\nabla}\cdot\vec{U} = 0, \tag{2.1}$$

$$\hat{\rho}\left(\frac{D\vec{U}}{Dt} + f\vec{e}_z \times \vec{U}\right) = -\vec{\nabla}\hat{P} - \hat{\rho}g\vec{e}_z + \mu\nabla^2\vec{U}, \tag{2.2}$$

$$\frac{D\hat{\rho}}{Dt} = \kappa\nabla^2\hat{\rho}, \tag{2.3}$$

where the material derivative $\frac{D}{Dt}$ is defined as $\frac{D}{Dt} = \frac{\partial}{\partial t} + \vec{U}\cdot\vec{\nabla}$, $\vec{U}$ is the velocity, $\hat{\rho}$ the density, $\hat{P}$ the pressure, μ the dynamic viscosity and κ the density diffusivity, respectively. The density and the pressure can be decomposed as $\hat{\rho} = \rho_0 + \tilde{\rho}$, $\hat{P} = P_0 + P$ where ρ_0, P_0 are the reference density and pressure which satisfy the hydrostatic balance $\vec{\nabla}P_0 = -\rho_0 g\vec{e}_z$. The Boussinesq approximation assumes that the reference density ρ_0 is much larger than the density variation $\tilde{\rho}$ (i.e. $\rho_0 >> \tilde{\rho}$). With this approximation, the continuity equation becomes

$$\vec{\nabla}\cdot\vec{U} = 0, \tag{2.4}$$

which is the same as in incompressible homogeneous fluids, and the momentum equations become

$$\frac{D\vec{U}}{Dt} + f\vec{e}_z \times \vec{U} = -\frac{1}{\rho_0}\nabla P - \frac{\tilde{\rho}}{\rho_0}g\vec{e}_z + \nu\nabla^2\vec{U}, \tag{2.5}$$

where $\nu = \mu/\rho_0$ is the kinematic viscosity. Note that the density variation $\tilde{\rho}$ is taken into account only in the buoyancy force in the vertical momentum equation (2.5). Moreover, the equation for the density variation $\tilde{\rho}$ reads

$$\frac{D\tilde{\rho}}{Dt} = \kappa\nabla^2\tilde{\rho}. \tag{2.6}$$

2 Linear stability equations

To perform a linear stability analysis, we consider base flows which are steady and axisymmetric with velocity $\vec{U}_b = (0, U_\theta(r), 0)$ in a cylindrical coordinate system (r, θ, z) with a stable density stratification $\tilde{\rho} = \bar{\rho}_b(z)$. In this thesis, we focus mainly on two types of the base flows: Rankine vortex and Taylor-Couette flow. The Rankine vortex has an azimuthal velocity profile $U_\theta(r)$ as

$$U_\theta = \Omega_0 r, \quad r < R, \tag{2.7a}$$

$$U_\theta = \Omega_0 \frac{R^2}{r}, \quad r > R, \tag{2.7b}$$

where R is the radius of the vortex core and Ω_0 the angular velocity at the vortex center $r = 0$, while the azimuthal velocity profile U_θ of the Taylor-Couette flow is

$$U_\theta = Ar + \frac{B}{r}, \tag{2.8}$$

where

$$A = \frac{r_o^2\Omega_o - r_i^2\Omega_i}{r_o^2 - r_i^2}, \quad B = \frac{r_i^2 r_o^2(\Omega_i - \Omega_o)}{r_o^2 - r_i^2}, \tag{2.9}$$

where r_i, r_o are the radius of the inner and outer cylinder, Ω_i and Ω_o are the angular velocity of the inner and outer cylinder, respectively. Then, the momentum equations for these base flows are

$$-\frac{U_\theta^2}{r} - fU_\theta = -\frac{1}{\rho_0}\frac{\partial P_b}{\partial r}, \tag{2.10}$$

$$0 = \nu\left(\frac{\partial^2 U_\theta}{\partial r^2} + \frac{1}{r}\frac{\partial U_\theta}{\partial r} - \frac{U_\theta}{r^2}\right), \tag{2.11}$$

$$0 = -\frac{1}{\rho_0}\frac{\partial P_b}{\partial z} - \frac{\bar{\rho}_b}{\rho_0}g. \tag{2.12}$$

where $P_b(r, z)$ is the pressure of the basic state. Note that (2.12) is the hydrostatic balance. In the following, we adimensionalize the lengths and time by a length scale L (ex. the radius of the vortex core) and a time scale T (ex. inverse of the angular velocity of the vortex core). All the variables are non-dimensionalized accordingly:

$$\frac{r}{L} \to r\ ,\ \frac{z}{L} \to z\ ,\ \frac{\vec{U}}{\left(\frac{L}{T}\right)} \to \vec{U}\ ,\ \frac{p}{\left(\frac{\rho_0 L^2}{T^2}\right)} \to p\ ,\ \frac{\rho}{\left(-\frac{\partial\bar{\rho}}{\partial z}\right)L} \to \rho. \tag{2.13}$$

Then, we subject perturbations to the basic state: $\vec{U} = (0, U_\theta, 0) + (u_r', u_\theta', u_z')$, $P = P_b + p'$ and $\tilde{\rho} = \bar{\rho}_b + \rho'$. We assume that the perturbations are infinitesimally small so that the equations can be linearized. We use the normal mode in the form

$$(u_r', u_\theta', u_z', p', \rho') = (u_r(r), u_\theta(r), u_z(r), p(r), \rho(r))e^{i(kz + m\theta - \omega t)} + c.c., \tag{2.14}$$

where k is the vertical wavenumber, m the azimuthal wavenumber, ω the complex eigenfrequency and *c.c.* denotes the complex conjugate. Then, the linearized non-dimensional equations of momentum, continuity and density read

$$i\left(-\omega + m\Omega\right)u_r - \left(\frac{2}{Ro} + 2\Omega\right)u_\theta = -\frac{dp}{dr} + \frac{1}{Re}\left[\nabla^2 u_r - \frac{u_r}{r^2} - \frac{2im}{r^2}u_\theta\right] \tag{2.15}$$

$$i\left(-\omega+m\Omega\right)u_\theta+(\frac{2}{Ro}+Z)u_r=-\frac{imp}{r}+\frac{1}{Re}\left[\nabla^2u_\theta-\frac{u_\theta}{r^2}+\frac{2im}{r^2}u_r\right] \tag{2.16}$$

$$i\left(-\omega+m\Omega\right)u_z=-ikp-\frac{1}{F^2}\rho+\frac{1}{Re}\nabla^2u_z \tag{2.17}$$

$$\frac{1}{r}\frac{\partial(ru_r)}{\partial r}+\frac{imu_\theta}{r}+iku_z=0 \tag{2.18}$$

$$i\left(-\omega+m\Omega\right)\rho-u_z=\frac{1}{ReSc}\nabla^2\rho \tag{2.19}$$

where $\nabla^2=\frac{d^2}{dr^2}+\frac{1}{r}\frac{d}{dr}-(k^2+\frac{m^2}{r^2})$ is the Laplacian operator, $\Omega=\frac{U_\theta}{r}$ is the angular velocity and $Z=\frac{1}{r}\frac{d}{dr}(rU_\theta)$ is the axial vorticity of the base state, $Ro=\frac{2}{fT}$ is the Rossby number, $Re=\frac{L^2}{T\nu}$ is the Reynolds number, $F=\frac{1}{NT}$ is the Froude number, $N=\sqrt{-\frac{g}{\rho_0}\frac{\partial\bar{\rho}}{\partial z}}$ is the Brunt Väisälä frequency and $Sc=\frac{\nu}{\kappa}$ is the Schmidt number. When the fluid is inviscid and non-diffusive, the equations (2.15)-(2.19) can be further simplified into a single equation for the pressure. From (2.17) and (2.19), we obtain

$$\rho=-i\frac{k}{F^{-2}-s^2}p, \tag{2.20}$$

$$u_z=\frac{ks}{F^{-2}-s^2}p, \tag{2.21}$$

where $s=-\omega+m\Omega$ is the Doppler-shifted frequency. From (2.15) and (2.16), we obtain

$$u_\theta=\left[\frac{ms}{r}p+\left(\frac{2}{Ro}+Z\right)\frac{dp}{dr}\right]/\Delta, \tag{2.22}$$

$$u_r=-i\left[s\frac{dp}{dr}+\frac{2m}{r}\left(\frac{1}{Ro}+\Omega\right)p\right]/\Delta, \tag{2.23}$$

where $\Delta=\left(\frac{2}{Ro}+2\Omega\right)\left(\frac{2}{Ro}+Z\right)-s^2$. By inserting (2.21)-(2.23) into the continuity equation (2.18), we obtain a single equation for the pressure p

$$\frac{d^2p}{dr^2}+\left(\frac{1}{r}-\frac{\Delta'}{\Delta}\right)\frac{dp}{dr}+\left[-\frac{k^2}{F^{-2}-s^2}\Delta-\frac{m^2}{r^2}+\frac{2m\Delta}{rs}\left(\frac{\frac{1}{Ro}+\Omega}{\Delta}\right)'\right]p=0, \tag{2.24}$$

where prime denotes a differentiation with respect to r. Similarly, we can also obtain a single equation for the radial velocity u_r

$$\frac{d^2u_r}{dr^2}+\left(\frac{1}{r}-\frac{Q'}{Q}\right)\frac{du_r}{dr}+\left[-\frac{k^2}{F^{-2}-s^2}\Delta-\frac{m^2}{r^2}-\frac{mrQ}{s}\left(\frac{\frac{2}{Ro}+Z}{r^2Q}\right)'+Q\left(\frac{1}{rQ}\right)'\right]u_r=0, \tag{2.25}$$

where $Q=\frac{m^2}{r^2}-\frac{k^2s^2}{F^{-2}-s^2}$ (see Billant & Le Dizès, 2009; Le Dizès & Billant, 2009; Park & Billant, 2012). Due to the symmetry $\omega(k,m)=\omega(-k,m)=-\omega^*(-k,-m)$, we consider hereafter only positive k and m. Moreover, we generally assume that the fluid is strongly stratified so that the hydrostatic approximation can be applied: $1/F >> |s|$ (i.e. $F^{-2}-s^2\approx F^{-2}$). This implies that (2.24) and (2.25) depend on k and F only through the rescaled vertical wavenumber $\tilde{k}=kF$ owing to the self-similarity of strongly-stratified fluids (Billant & Chomaz, 2001). This assumption also implies that there is no singularity where $|s|=1/F$.

3 Boundary conditions

In order to integrate the equations (2.24) or (2.25) in the inviscid limit, we need to impose boundary conditions. For a vortex, the domain is from the vortex center $r = 0$ to infinity $r \to \infty$. To find the boundary conditions at the vortex center $r = 0$, a Taylor expansion can be applied around $r = 0$ for the equations (2.15)-(2.19). Depending on the azimuthal wavenumber m, the leading order of the Taylor expansions read

$$u_r \sim O(r) \ , \ u_\theta \sim O(r) \ , \ u_z \sim O(1) \ , \ p \sim O(1) \ , \ \rho \sim O(1), \tag{2.26}$$

if $m = 0$, or

$$u_r \sim O(r^{|m|-1}) \ , \ u_\theta \sim O(r^{|m|-1}) \ , \ u_z \sim O(r^{|m|}) \ , \ p \sim O(r^{|m|}) \ , \ \rho \sim O(r^{|m|}), \tag{2.27}$$

if $|m| \geq 1$ (Saffman, 1992; Fabre & Jacquin, 2004; Riedinger, Le Dizès & Meunier, 2010b). For $r \to \infty$, the boundary condition is that the perturbations vanish or correspond to a wave propagating outward. From (2.24), we can find an asymptotic solution for $r >> R$ for the pressure

$$p(r) \sim H_m^{(1)}\left(\tilde{k} r \sqrt{-\Delta_\infty}\right), \tag{2.28}$$

where $H_m^{(1)}$ is the Hankel function of the first kind of order m and $\Delta_\infty = \Delta(r \to \infty)$. For real ω, $H_m^{(1)}$ behaves as an outgoing wave if $\Delta_\infty < 0$; otherwise it decreases exponentially with r (Abramowitz & Stegun, 1965). We can also obtain asymptotic solutions for the other variables by inserting (2.28) into (2.20)-(2.23).

For the Taylor-Couette flow, the domain is from the inner cylinder $r = r_i$ to the outer cylinder $r = r_o$ so that we apply impermeable boundary conditions at both cylinders

$$u_r(r_i) = u_r(r_o) = 0. \tag{2.29}$$

In the case of the Taylor-Couette flow, we shall also investigate viscous effects (chapter 4). In this case, the boundary conditions are

$$u_r = u_\theta = u_z = 0 \ , \ \frac{d\rho}{dr} = 0, \tag{2.30}$$

at both cylinders $r = r_i, r_o$ (Caton *et al.*, 2000).

4 Numerical methods

4.1 Shooting method

In the inviscid limit, we use a shooting method to solve the eigenvalue problem. One of the advantages of the shooting method is that it can be used for discontinuous flows such as the Rankine vortex. In the shooting method, we impose the boundary conditions and then integrate the equations (2.24) or (2.25) with an initial guess of eigenfrequency ω_{guess}, from the boundaries to a fitting point r_f. At the fitting point, we compute the Wronskian $W_k = p(r_f^+)p'(r_f^-) - p(r_f^-)p'(r_f^+)$ (or in terms of u_r) and we use the secant method to find a next guess value for ω and continue this iterative process until $W_k = 0$. In the particular case of the Rankine vortex, since the axial vorticity is discontinuous, we do not compute the

Wronskian but we impose that the radial velocity and the pressure are continuous at the vortex core $r = R$ (i.e. $u_r(R^+) = u_r(R^-)$, $p(R^+) = p(R^-)$).

Another advantage of the shooting method is that we can easily deform the contour of integration in the complex plane around a critical point r_c. By deforming the integration contour above r_c since the angular velocity generally decreases in vortices, viscous effects which smooth the singularity can be taken into account (Le Dizès, 2004; Schecter & Montgomery, 2004; Billant, 2010)

4.2 Chebyshev spectral collocation method

In the presence of viscosity, we use a spectral method. One of the advantages of the spectral method is that we do not need a guess value for the eigenfrequency since the global spectrum is computed (Schmid & Henningson, 2001). The collocation points are distributed along radial direction r using the Chebyshev discretization. The MATLAB differentiation matrix suite for the Chebyshev polynomials written by Weideman & Reddy (2000) is used. The Chebyshev collocation points $s_j \in [-1, 1]$ are defined as

$$s_j = cos\left(\frac{(j-1)\pi}{N-1}\right) \ , \ j = 1, \ldots, N, \tag{2.31}$$

where N is the number of collocation points (Weideman & Reddy, 2000).

For a vortex, we use the algebraic mappings from s to r as

$$r(s) = \gamma \frac{s}{\sqrt{1-s^2}}, \quad \text{or} \tag{2.32a}$$

$$r(s) = \gamma \frac{s}{1-s^2}, \tag{2.32b}$$

where γ is the stretching factor. These mappings have been used previously in various works (Antkowiak, 2005; Fabre & Jacquin, 2004; Fabre *et al.*, 2006; Riedinger *et al.*, 2010b). Note that r varies in the interval $r \in [-\infty, \infty]$ and not in the interval $[0, \infty]$. The advantage of these mappings is that using the parity properties

$$[u_r(-r), u_\theta(-r)] = -(-1)^{|m|} [u_r(r), u_\theta(r)] , \tag{2.33}$$

$$[u_z(-r), p(-r), \rho(-r)] = (-1)^{|m|} [u_z(r), p(r), \rho(r)] , \tag{2.34}$$

we do not need to impose any boundary conditions at the vortex center $r = 0$. The Chebyshev expansions are of order $2N$ but there are N collocation points (Fabre & Jacquin, 2004; Antkowiak, 2005). Additionally, if we introduce an angle θ, we can avoid the singularities on the real axis by integrating in the complex plane $r' = re^{i\theta}$ and eigenvalues can be computed more efficiently (Fabre *et al.*, 2006; Riedinger *et al.*, 2010b).

For the Taylor-Couette flow, we use the linear mapping

$$r = r_i \left(\frac{1 - r_o/r_i}{2} s + \frac{1 + r_o/r_i}{2}\right), \tag{2.35}$$

where $s = 1 \to -1$ maps into $r = r_i \to r_o$. The advantage of this linear mapping is that the collocation points are concentrated on both boundaries of the Taylor-Couette flow where the

variations are stronger. In the case of the semi-infinite domain such as for the flow around a rotating cylinder, we use the semi-infinite mapping

$$r = r_i \left[1 + \gamma \left(\frac{1}{s+1} - \frac{1}{2} \right) \right], \tag{2.36}$$

where $s = 1 \rightarrow -1$ maps into $r = r_i \rightarrow \infty$.

The equations (2.15)-(2.19) have 5 variables (i.e. u_r, u_θ, u_z, p and ρ) so that differentiation matrices are $(5N \times N)$ if we use all the equations. A more efficient way is to first reduce the equations to 3 variables: $\vec{x} = (u_r, u_\theta, \rho)^T$. They can be expanded in Chebyshev space

$$\vec{x}(r) = \begin{pmatrix} u_r \\ u_\theta \\ \rho \end{pmatrix} = \sum_{j=1}^{j=N} \begin{pmatrix} a_j \\ b_j \\ c_j \end{pmatrix} T_{j-1}(s(r)), \tag{2.37}$$

where $\vec{c}_x = (a_j, b_j, c_j)^T$ are constants and T_j is a Chebyshev polynomial of order j. Then, the equations of momentum (2.15)-(2.19) can be written as

$$(-i\omega)\mathbf{B}\vec{x} + \mathbf{A}\vec{x} = \mathbf{0}, \tag{2.38}$$

where $\mathbf{B}$ is an energy operator

$$\mathbf{B} = \begin{pmatrix} \mathbf{B}_{11} & \mathbf{B}_{12} & 0 \\ \mathbf{B}_{21} & \mathbf{B}_{22} & 0 \\ 0 & 0 & \mathbf{B}_{33} \end{pmatrix} = \begin{pmatrix} I & 0 & 0 \\ 0 & I & 0 \\ 0 & 0 & I \end{pmatrix} + b_1 b_2^T, \tag{2.39}$$

with $b_1^T = \frac{1}{ik}\left(\frac{\partial}{\partial r}, \frac{im}{r}, 0\right)$, $b_2^T = \frac{1}{ik}\left(\frac{\partial}{\partial r} + \frac{1}{r}, \frac{im}{r}, 0\right)$, and $\mathbf{A}$ is an operator which can be decomposed as

$$\mathbf{A} = \begin{pmatrix} \mathbf{A}_{11} & \mathbf{A}_{12} & \mathbf{A}_{13} \\ \mathbf{A}_{21} & \mathbf{A}_{22} & \mathbf{A}_{23} \\ \mathbf{A}_{31} & \mathbf{A}_{32} & \mathbf{A}_{33} \end{pmatrix} = \mathbf{C} + \frac{1}{F^2}\mathbf{C}_{st} + \frac{1}{Ro}\mathbf{C}_{ro} - \frac{1}{Re}\mathbf{D}, \tag{2.40}$$

where $\mathbf{C}$ is a coupling operator

$$\mathbf{C} = \begin{pmatrix} \mathbf{C}_{11} & \mathbf{C}_{12} & 0 \\ \mathbf{C}_{21} & \mathbf{C}_{22} & 0 \\ \mathbf{C}_{31} & \mathbf{C}_{32} & \mathbf{C}_{33} \end{pmatrix} = \begin{pmatrix} im\Omega & -2\Omega & 0 \\ Z & im\Omega & 0 \\ 0 & 0 & im\Omega \end{pmatrix} + b_1(im\Omega)b_2^T - c_1 c_2^T, \tag{2.41}$$

with $c_1^T = \frac{i}{k}\left(0, 0, \frac{1}{r}\right)$, $c_2^T = \left(r\frac{\partial}{\partial r} + 1, im, 0\right)$, $\mathbf{C}_{st}$ is a coupling operator due to the stratification

$$\mathbf{C}_{st} = \begin{pmatrix} 0 & 0 & \mathbf{C}_{st13} \\ 0 & 0 & \mathbf{C}_{st23} \\ 0 & 0 & 0 \end{pmatrix} = c_2 c_1^T, \tag{2.42}$$

$\mathbf{C}_{ro}$ is a coupling operator due to the planetary rotation

$$\mathbf{C}_{ro} = \begin{pmatrix} 0 & -2 & 0 \\ 2 & 0 & 0 \\ 0 & 0 & 0 \end{pmatrix}, \tag{2.43}$$

and $\mathbf{D}$ is a diffusion operator

$$\mathbf{D} = \begin{pmatrix} \mathbf{D}_{11} & \mathbf{D}_{12} & 0 \\ \mathbf{D}_{21} & \mathbf{D}_{22} & 0 \\ 0 & 0 & \mathbf{D}_{33} \end{pmatrix} = \begin{pmatrix} \Delta_{m,k} - \frac{1}{r^2} & -2\frac{im}{r^2} & 0 \\ 2\frac{im}{r^2} & \Delta_{m,k} - \frac{1}{r^2} & 0 \\ 0 & 0 & \frac{1}{Sc}\Delta_{m,k} \end{pmatrix} + b_1 \Delta_{m,k} b_2^T, \quad (2.44)$$

where $\Delta_{m,k} = \frac{1}{r}\frac{\partial}{\partial r}\left(r\frac{\partial}{\partial r}\right) - \left(k^2 + \frac{m^2}{r^2}\right)$ (see also Antkowiak, 2005).

The boundary conditions are imposed in the matrices. For a vortex, we impose the boundary conditions for $|r| \to \infty$ by suppressing terms in the first/last column/row of the differentiation matrices so that perturbations vanish. The boundary conditions for $r = 0$ is imposed using the parity conditions (2.33) and (2.34) (for more details, refer to Antkowiak, 2005; Fabre & Jacquin, 2004; Fabre *et al.*, 2006). For the Taylor-Couette flow, we impose $u_r = 0$ at both cylinders $r = r_i, r_o$ if it is inviscid, or $u_r = 0, u_\theta = 0, d\rho/dr = 0$ for viscous fluids. In the latter case, we also impose $du_r/dr = 0$ instead of $u_z = 0$. The continuity equation (2.18) implies that these two relations are equivalent. In terms of the Chebyshev polynomials, the viscous boundary conditions can be rewritten

$$u_r(r = r_i, r_o) = \sum_{j=1}^{N} a_j T_{j-1}(\pm 1) = 0, \quad (2.45)$$

$$u_\theta(r = r_i, r_o) = \sum_{j=1}^{N} b_j T_{j-1}(\pm 1) = 0, \quad (2.46)$$

$$\rho'(r = r_i, r_o) = \sum_{j=1}^{N} c_j T'_{j-1}(\pm 1) = 0, \quad (2.47)$$

$$u'_r(r = r_i, r_o) = \sum_{j=1}^{N} a_j T'_{j-1}(\pm 1) = 0. \quad (2.48)$$

Using the matrix

$$\mathbf{T} = \begin{pmatrix} T_0(s_0) & T_1(s_0) & \dots & T_{N-1}(s_0) \\ T_0(s_1) & T_1(s_1) & \dots & T_{N-1}(s_1) \\ \vdots & \vdots & T_i(s_j) & \vdots \\ T_0(s_{N-1}) & T_1(s_{N-1}) & \dots & T_{N-1}(s_{N-1}) \end{pmatrix}, \quad (2.49)$$

the eigenvalue problem can be written

$$(-i\omega) \begin{pmatrix} \mathbf{B}'_{11} & \mathbf{B}'_{12} & \mathbf{B}'_{13} \\ \mathbf{B}'_{21} & \mathbf{B}'_{22} & \mathbf{B}'_{23} \\ \mathbf{B}'_{31} & \mathbf{B}'_{32} & \mathbf{B}'_{33} \end{pmatrix} \begin{bmatrix} a_j \\ b_j \\ c_j \end{bmatrix} = \begin{pmatrix} \mathbf{A}'_{11} & \mathbf{A}'_{12} & \mathbf{A}'_{13} \\ \mathbf{A}'_{21} & \mathbf{A}'_{22} & \mathbf{A}'_{23} \\ \mathbf{A}'_{31} & \mathbf{A}'_{32} & \mathbf{A}'_{33} \end{pmatrix} \begin{bmatrix} a_j \\ b_j \\ c_j \end{bmatrix}, \quad (2.50)$$

where $\mathbf{A}_{ij}{}'$ and $\mathbf{B}_{ij}{}'$ are matrices containg the boundary conditions. For example, $\mathbf{A}'_{1j}$ and $\mathbf{B}'_{1j}$ are

$$\mathbf{A}'_{11} = \begin{bmatrix} \epsilon_0 T_0(1) & \dots & \epsilon_0 T_{N-1}(1) \\ \epsilon_0 T'_0(1) & \dots & \epsilon_0 T'_{N-1}(1) \\ & \mathbf{A}_{11}\mathbf{T} & \\ \epsilon_0 T'_0(-1) & \dots & \epsilon_0 T'_{N-1}(-1) \\ \epsilon_0 T_0(-1) & \dots & \epsilon_0 T_{N-1}(-1) \end{bmatrix}, \quad \mathbf{A}'_{12} = \begin{bmatrix} \mathbf{0} \\ \mathbf{0} \\ \mathbf{A}_{12}\mathbf{T} \\ \mathbf{0} \\ \mathbf{0} \end{bmatrix}, \quad \mathbf{A}'_{13} = \begin{bmatrix} \mathbf{0} \\ \mathbf{0} \\ \mathbf{A}_{13}\mathbf{T} \\ \mathbf{0} \\ \mathbf{0} \end{bmatrix} \quad (2.51)$$

$$\mathbf{B}'_{11} = \begin{bmatrix} T_0(1) & \dots & T_{N-1}(1) \\ T'_0(1) & \dots & T'_{N-1}(1) \\ & \mathbf{B}_{11}\mathbf{T} & \\ T'_0(-1) & \dots & T'_{N-1}(-1) \\ T_0(-1) & \dots & T_{N-1}(-1) \end{bmatrix}, \quad \mathbf{B}'_{12} = \begin{bmatrix} \mathbf{0} \\ \mathbf{0} \\ \mathbf{B}_{12}\mathbf{T} \\ \mathbf{0} \\ \mathbf{0} \end{bmatrix}, \quad \mathbf{B}'_{13} = \begin{bmatrix} \mathbf{0} \\ \mathbf{0} \\ \mathbf{B}_{13}\mathbf{T} \\ \mathbf{0} \\ \mathbf{0} \end{bmatrix} \tag{2.52}$$

where ϵ_0 is a complex artificial parameter to impose the boundary conditions. The other block matrices $\mathbf{A}'_{ij}$ and $\mathbf{B}'_{ij}$ are modified similarly. The eigenmodes with an eigenvalue $\omega = \epsilon_0 i$ do not satisfy the boundary conditions (i.e. the spurious modes) so that they have to be ignored (see Schmid & Henningson, 2001). In contrast, all the physical eigenmodes satisfy the boundary conditions (2.45)-(2.48).

5 The WKBJ approximation

5.1 Introduction to the WKBJ approximation

The WKBJ analysis is a powerful method, named after the physicists Wentzel, Kramers, Brillouin and Jeffreys, to find an approximate solution of a differential equation when the solutions are rapidly varying. In general, the WKBJ method solves differential equations of the form

$$\epsilon^n \frac{d^n y}{dx^n} + a_1(x)\frac{d^{n-1}y}{dx^{n-1}} + \cdots a_{n-1}(x)\frac{dy}{dx} + a_n(x)y(x) = 0, \tag{2.53}$$

where ϵ is small. An asymptotic solution can be found in the form

$$y(x) \sim \exp\left[\frac{1}{\epsilon}\sum_{n=0}^{\infty}\epsilon^n S_n(x)\right], \tag{2.54}$$

where the functions S_n are of order of unity. For example, if we insert (2.53) in the equation

$$\epsilon^2 y'' = f(x)y, \tag{2.55}$$

we obtain

$$S_0'^2 + \epsilon\left(2S'_0S'_1 + S''_0\right) + \epsilon^2\left(S_1'^2 + 2S'_0S'_2 + S''_1\right) + \cdots = f(x). \tag{2.56}$$

We then solve each order in ϵ:

$$S_0'^2 = f(x), \tag{2.57a}$$

$$2S'_0S'_1 + S''_0 = 0, \tag{2.57b}$$

$$2S'_0S'_j + S''_{j-1} + \sum_{i=1}^{j-1} S'_iS'_{j-i} = 0, \quad j \geq 2. \tag{2.57c}$$

The two first functions S_n are

$$S_0(x) = \pm\int^x \sqrt{f(t)}dt\ ,\ S_1(x) = -\frac{1}{4}log(f(x))\ ,\cdots, \tag{2.58}$$

so that the solution of (2.55) is

$$y(x) \sim \frac{1}{f^{1/4}}\left[c_1\exp\left(\frac{1}{\epsilon}\int^x\sqrt{f(t)}dt\right) + c_2\exp\left(-\frac{1}{\epsilon}\int^x\sqrt{f(t)}dt\right)\right], \tag{2.59}$$

where c_1 and c_2 are constants (Bender & Orszag, 1978).

In this thesis, the WKBJ method will be used to solve the perturbation equations (2.24) for the pressure p and (2.25) for the radial velocity u_r when the rescaled vertical wavenumber $\tilde{k} = kF$ is large. In this limit, the equation for the pressure p can be written

$$\frac{d^2p}{dr^2} + \left(\frac{1}{r} - \frac{\Delta'}{\Delta}\right)\frac{dp}{dr} + \left[-\tilde{k}^2\Delta + O\left(1\right)\right]p = 0, \tag{2.60}$$

where the $O(1)$ terms will be negligible at leading order. Similarly, the equation for the radial velocity u_r can be written

$$\frac{d^2u_r}{dr^2} + \left(\frac{1}{r} - \frac{Q'}{Q}\right)\frac{du_r}{dr} + \left[-\tilde{k}^2\Delta + O\left(1\right)\right]u_r = 0. \tag{2.61}$$

The WKBJ approximation for the pressure is

$$p(r) \sim \frac{\Delta^{1/4}}{r^{1/2}}\left[A\exp\left\{\tilde{k}\int_{r_t}^{r}\sqrt{\Delta(t)}dt\right\} + B\exp\left\{-\tilde{k}\int_{r_t}^{r}\sqrt{\Delta(t)}dt\right\}\right], \tag{2.62}$$

where A, B are constants and r_t is a so-called turning point where $\Delta(r_t) = 0$. Similarly, the WKBJ approixmation for the radial velocity u_r is

$$u_r(r) \sim \frac{Q^{1/2}}{r^{1/2}\Delta^{1/4}}\left[A'\exp\left\{\tilde{k}\int_{r_t}^{r}\sqrt{\Delta(t)}dt\right\} + B'\exp\left\{-\tilde{k}\int_{r_t}^{r}\sqrt{\Delta(t)}dt\right\}\right], \tag{2.63}$$

where A' and B' are constants. When Δ is real, the sign of Δ determines whether the approximation is evanescent or wavelike, and the solutions are evanescent if $\Delta > 0$ and wavelike otherwise. In the latter case, the asymptotic solutions (2.62) and (2.63) can be rewritten

$$p(r) \sim \frac{(-\Delta)^{1/4}}{r^{1/2}}\left[C\exp\left\{i\tilde{k}\int_{r_t}^{r}\sqrt{-\Delta(t)}dt\right\} + D\exp\left\{-i\tilde{k}\int_{r_t}^{r}\sqrt{-\Delta(t)}dt\right\}\right], \tag{2.64}$$

$$u_r(r) \sim \frac{Q^{1/2}}{r^{1/2}(-\Delta)^{1/4}}\left[C'\exp\left\{i\tilde{k}\int_{r_t}^{r}\sqrt{-\Delta(t)}dt\right\} + D'\exp\left\{-i\tilde{k}\int_{r_t}^{r}\sqrt{-\Delta(t)}dt\right\}\right], \tag{2.65}$$

where C, D, C' and D' are constants. The WKBJ approximation breaks down near the turning point r_t since higher order terms are no longer negligible compared to the leading order term as Δ becomes zero. However, they can be connected by a local analysis around r_t.

While it is simple to figure out whether an evanescent solution increases or decreases exponentially with r, it is less straight forward to determine the direction of propagation of a wavelike solution. To do so, we need to look at the phase velocity and group velocity in the radial direction. For example, the phase velocity v_ϕ and the group velocity v_g of the first term of the equations (2.64) and (2.65) are as follows:

$$v_\phi = \frac{\omega_r}{l_r} = \frac{\omega_r}{Re\left[\frac{d}{dr}\left(\tilde{k}\int_{r_t}^{r}\sqrt{-\Delta(t)}dt\right)\right]} = \frac{\omega_r}{\tilde{k}Re\left(\sqrt{-\Delta}\right)}\ ,\ v_g = \frac{\partial\omega_r}{\partial l_r} = \frac{Re\left(\sqrt{-\Delta}\right)}{\tilde{k}Re(-s)}, \tag{2.66}$$

where l_r is the local radial wavenumber. The phase velocity v_ϕ depends on the sign of the frequency ω_r while the group velocity v_g depends on the sign of the Doppler-shifted frequency s. This implies that the group velocity v_g changes its sign at the critical point where $s(r_c) = 0$. Therefore, when $s < 0$, the first term of (2.64)-(2.65) represents a wave propagating outward whereas when $s > 0$, it corresponds to a wave propagating inward.

5.2 Flow configurations for the radiative instability

Based on the WKBJ analysis, we can explain the radiative instability by looking at the behaviour of the solutions. As explained in the previous chapter, the WKBJ approximations are wavelike or evanescent depending on the sign of Δ. In order to have the radiative instability, there must exist a potential barrier where the solutions are evanescent, enclosed by two wave regions, a first wave region outside the potential barrier and a second wave region between the potential barrier and a boundary (figure 2.1). Moreover, a critical point r_c where $s(r_c) = 0$ is necessary in the potential barrier (Lindzen & Barker, 1985; Le Dizès & Billant, 2009). When the potential barrier is sufficiently small (figure 2.1a), an incident gravity wave emitted in the first wave region toward the right penetrates the potential barrier, and reflects back. The amplitude of this reflected wave has a larger amplitude, a phenomenon known as wave over-reflection (Takehiro & Hayashi, 1992; Schecter & Montgomery, 2006; Schecter, 2008). This reflected wave reflects again (normal reflection) at the left boundary so that it will experience another over-reflection process when encoutering the potential barrier. These successive cycles of over-reflection are the origin of the radiative instability (Lindzen *et al.*, 1980; Takehiro & Hayashi, 1992; Billant & Le Dizès, 2009). When the potential barrier is large (figure 2.1b), the amplitude of gravity wave emitted through the potential barrier is reduced leading to less over-reflection. In the limit of an infinite potential barrier (figure 2.2), there is no wave emission and the waves are trapped between the boundary and the potential barrier. The modes are then neutral. The magnitude of the over-reflection therefore depends on the size of the potential barrier. It is thus important to determine the parameters that govern its size.

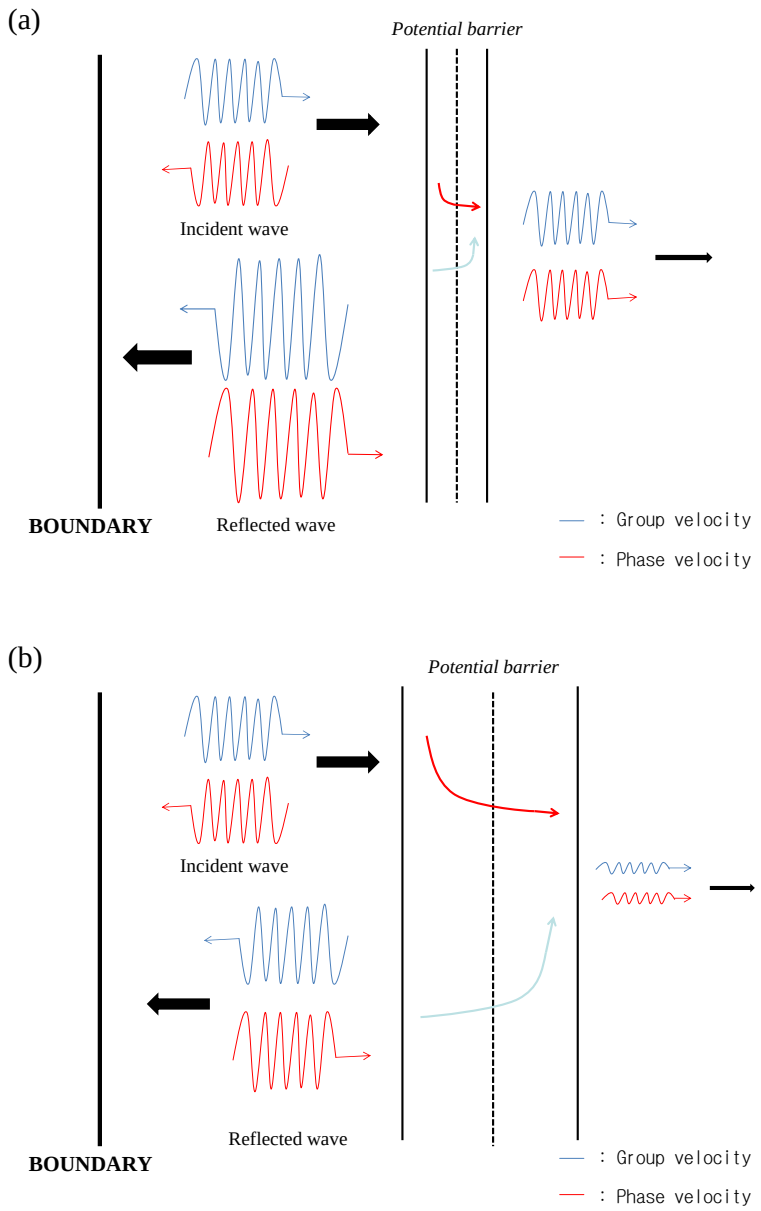

Figure 2.1: Examples of the eigenmode structures for the radiative instability in the presence of a potential barrier and a perfectly reflecting boundary (bold line). The potential barrier bounded by two turning points (thin solid lines) contains a critical point (dashed lines). The gravity wave emission on the right of the potential barrier and the over-reflection are attenuated as the size of the potential barrier increases (compare (a) and (b)).

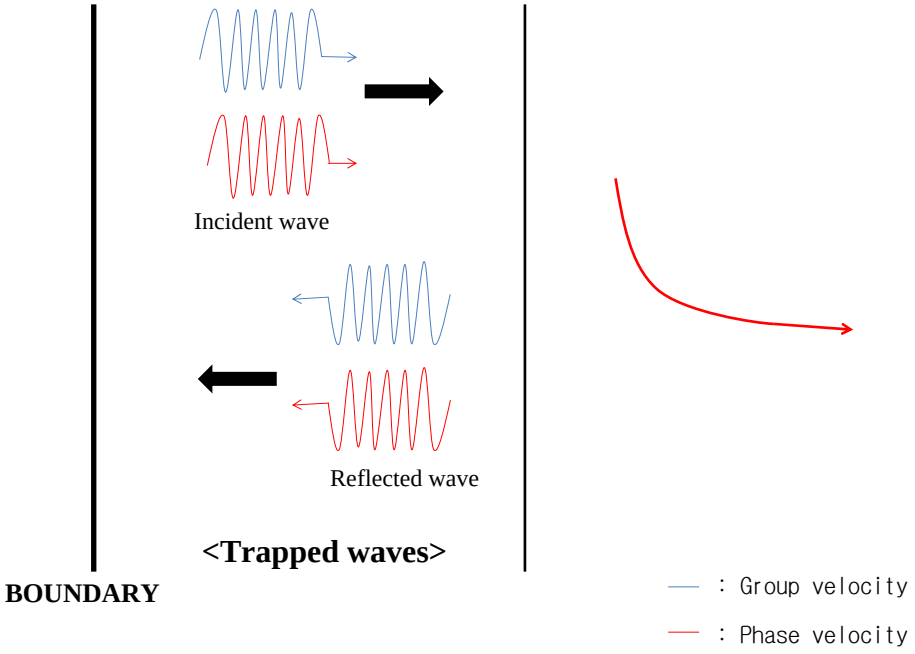

Figure 2.2: Waves trapped between the boundary and the potential barrier (i.e. perfect reflection).

5.3 Epicyclic frequency $\omega_{\pm}(r)$ and critical frequency $\omega_c(r)$

To determine the behaviour of the WKBJ approximations, it is useful to define the epicyclic frequency $\omega_{\pm}(r)$

$$\omega_{\pm}(r) = m\Omega \pm \sqrt{(f + 2\Omega)(f + Z)}, \tag{2.67}$$

which tells us where the function Δ becomes zero (i.e. where the turning points r_t are) (Le Dizès & Lacaze, 2005; Le Dizès & Billant, 2009; Billant & Le Dizès, 2009; Park & Billant, 2012). When the frequency ω_r lies in the range $\omega_- < \omega_r < \omega_+$, Δ is positive and the solutions are evanescent. In contrast, when $\omega_r > \omega_+$ or $\omega_r < \omega_-$, Δ is negative and the solutions are wavelike. These behaviours apply in the limit $F \to 0$ and are reversed in homogeneous fluids $F \to \infty$ (Le Dizès & Lacaze, 2005). We also define the critical frequency $\omega_c(r)$

$$\omega_c(r) = m\Omega, \tag{2.68}$$

which tells us where the Doppler-shifted frequency $s(r) = -\omega + m\Omega$ becomes zero and where the critical point r_c is located. Note that $\omega_c(r)$ always lies between $\omega_+(r)$ and $\omega_-(r)$.

Figure 2.3 shows an example of the epicyclic frequencies $\omega_{\pm}$ and the critical frequency for the Rankine vortex for $m = 1$ for the Coriolis parameter $f = 0.05\Omega$. The regions where the solutions are wavelike (i.e. $\Delta < 0$) are shaded. $\omega_+(r)$ and $\omega_-(r)$ are plotted by upper and lower solid line, and $\omega_c(r)$ is plotted by a dashed line. Note that the lines are discontinuous at the vortex core $r = R$ since the axial vorticity $Z(r)$ of the Rankine vortex is discontinuous there.

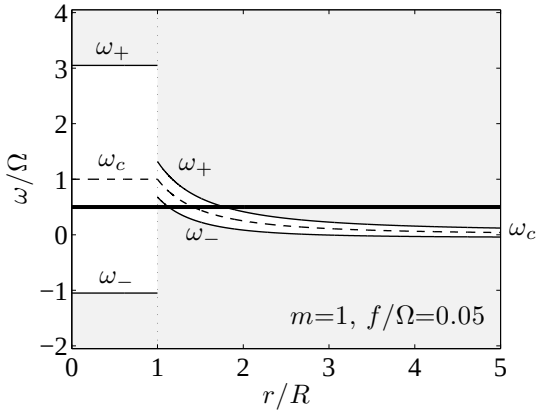

Figure 2.3: Examples of the epicyclic frequencies $\omega_\pm$ and the critical frequency ω_c of the Rankine vortex for $m = 1$ and $f/\Omega = 0.05$.

However, the epicyclic frequencies of the Rankine vortex resemble those of other continuous monotonic vortices such as the Lamb-Oseen vortex. The horizontal bold line shows an example of frequency where there exists a radiative configuration. There are indeed two wave regions separated by a potential barrier which contains the critical point r_c. The inner wave region is bounded by the vortex core $r = R$. Other examples of the epicyclic frequencies and critical frequency for $m = 1$ for different values of f from cyclonic rotation $f > 0$ to anticyclonic rotation $f < 0$ are shown in figure 2.4.

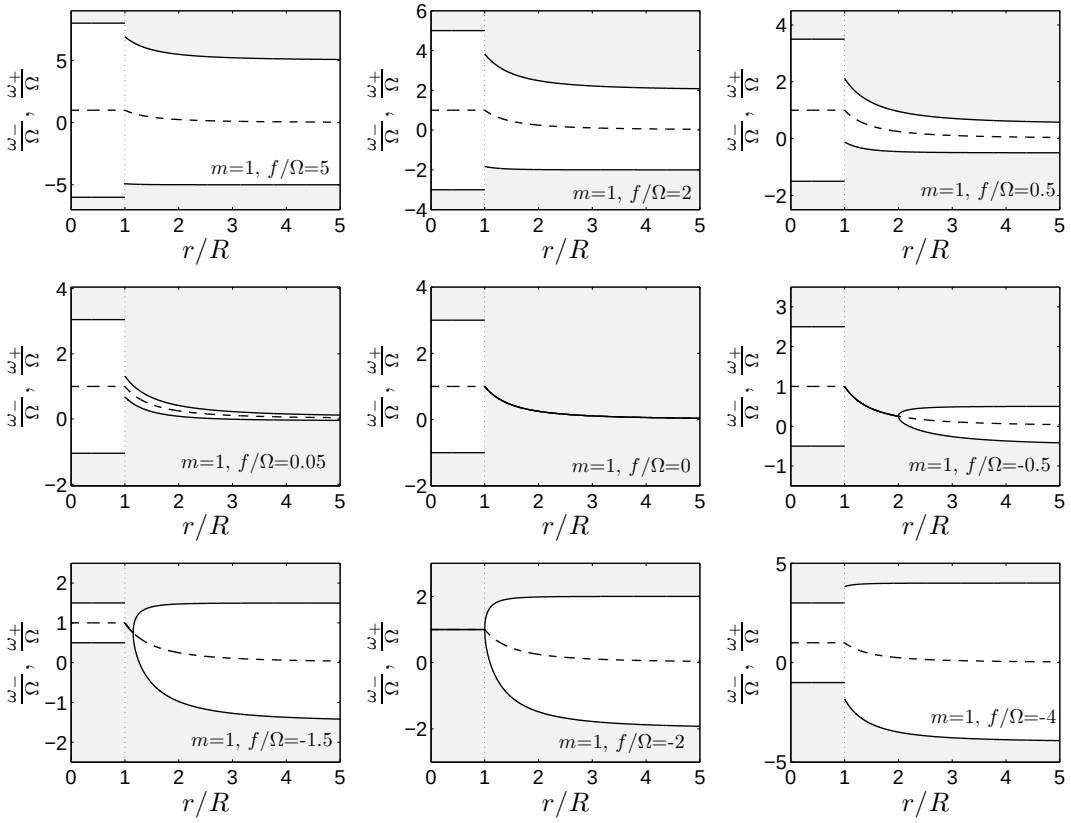

Figure 2.4: Examples of the epicyclic frequencies $\omega_\pm$ and the critical frequency ω_c of the Rankine vortex for $m = 1$ for different values of f.

We shall see (chapter 3) that there is no radiative configuration for $m = 1$ for strong cyclonic rotation $f/\Omega > 1$ since the potential barrier widens as f increases. In this range, neutral modes exist. For non-rotating fluids $f = 0$, the potential barrier disappears and the critical point and the two turning points merge. When f is in the range $-2 < f/\Omega < 0$, the epicyclic frequencies become complex since the Rayleigh's discriminant $\phi = (f + 2\Omega)(f + Z)$ is negative. It is therefore centrifugally unstable. For strong anticyclonic rotation with $f/\Omega \leq -2$, we shall find in chapter 4 that for $m = 1$ there is neither the radiative instability nor the centrifugal instability, but neutral modes exist.

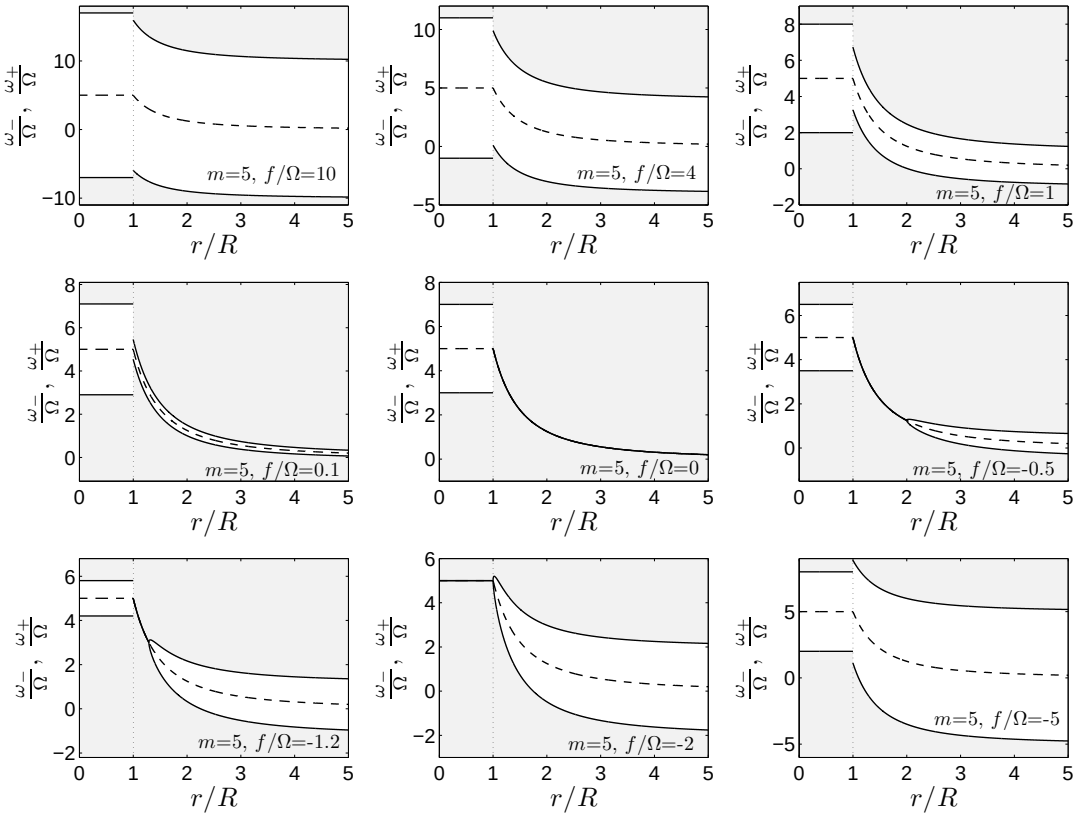

Figure 2.5: Same as figure 2.4 but for $m = 5$.

Figure 2.5 is the same as figure 2.4 but for $m = 5$. The global behaviour is the same as for $m = 1$ except that radiative configurations also exists for $f/\Omega < -2$. The radiative instability in this range will be investigated in chapter 4 (section 1) and will be shown to exist for azimuthal wavenumbers larger than 2.

Chapter 3

Effect of rotation on the radiative instability

1 Instabilities and waves on a columnar vortex in a strongly-stratified and rotating fluid

Article to be submitted to Physics of Fluids.

Instabilities and waves on a columnar vortex in a strongly-stratified and rotating fluid

Junho Park[a)] and Paul Billant

Laboratoire d'Hydrodynamique (LADHYX), CNRS, Ecole Polytechnique, Palaiseau Cedex F-91128, France

(Dated: 15 December 2012)

This paper investigates the effect of the planetary rotation on the radiative instability of a columnar Rankine vortex in a strongly stratified fluid. We show that a cyclonic rotation strongly stabilizes the radiative instability. The modes become neutral when the Rossby number is below a critical value which depends on the azimuthal wavenumber of the wave. In the limit of small Rossby number, there exists fast neutral waves that are not captured by the quasi-geostrophic theory. In the presence of weak anticyclonic rotation, the radiative instability becomes dominated by the centrifugal instability only when the Rossby number is above -400. The numerical stability analysis is completed by asymptotic analyses for large wavenumbers which explain the properties and mechanisms of the waves and the instabilities. The stability of a continuous smoothed Rankine vortex is also investigated. The most amplified azimuthal wavenumber is then finite instead of infinite for the Rankine vortex.

[a)]junho.park@ladhyx.polytechnique.fr

I. INTRODUCTION

In 1880, Lord Kelvin has described the waves sustained by a Rankine vortex[1]. These waves, now called the vortex Kelvin waves, is an important subject in vortex dynamics[2,3]. In homogeneous fluids, the Kelvin waves are confined to the vortical region of the vortex and belongs to the family of inertial waves. In contrast, vortex waves are no longer confined to the vortex core in stratified fluids but can exist outside in the form of internal gravity waves. A subtle coupling between the vortex rotation and internal waves leads to an instability which spontaneously emit internal waves from the vortex.

This radiative instability does not require the presence of vorticity and can occur on the potential flow around a rotating cylinder[4,5]. The instability mechanism has been explained in terms of wave over-reflection by means of a WKBJ analysis[6,7]. A wave emitted from the vortex core is indeed over-reflected at the critical radius where the angular velocity of the vortex is equal to the azimuthal phase velocity of the vortex. This phenomenon has been also explained in terms of pseudo-angular momentum. The transmitted wave has a negative pseudoangular momentum so that the reflected wave should have a larger amplitude to conserve the total pseudo-angular momentum[8–10]. The radiative instability occurs not only in stratified fluids[6–10], but also in shallow-water[11] or in compressible fluids with the emission of acoustic waves[12].

Geophysical flows are not only stably stratified but also under the influence of the planetary rotation. In this paper, we shall see that the radiative instability becomes much weaker in the presence of a cyclonic planetary rotation. Such stabilization has been already reported by Schecter & Montgomery[9] for some particular modes and vortex profiles. Here, we shall investigate systematically the effect of the planetary rotation on all the discrete waves sustained by a Rankine vortex and a smoothed Rankine vortex. We shall see that the stabilization of the radiative instability depends strongly on the azimuthal wavenumber of the waves and on the vortex profile. These results will be explained theoretically by means of a WKBJ analysis.

In the presence of small anticyclonic rotation, a vortex is unstable to the centrifugal instability but we shall show that the radiative instability remains the most dangerous instability when the Rossby number $Ro = 2\Omega/f$ is sufficiently large $Ro \lesssim -400$ where Ω is the angular velocity at the vortex center and f the Coriolis parameter.

The regime $-1 < Ro < 0$ where the centrifugal instability no longer exists has been already considered[13]. We have shown that the radiative instability can also occur in this range if the azimuthal wavenumber is larger than 2. We shall therefore restrict the analysis here to the range $1/Ro > -1$ (i.e. $f > -2\Omega$).

The paper is organized as follows: the stability problem is described in Sec. **II**. In Sec. **III**, the effect of cyclonic rotation is presented. In Sec. **IV**, WKBJ analyses for large vertical wavenumber k are performed to explain the instability mechanism and properties. The effect of an anticyclonic rotation is investigated in Sec. **V**. Finally, the effect of the smoothness of the vorticity profile is presented in Sec. **VI**.

II. PROBLEM FORMULATION

We consider an axisymmetric vortex with velocity components $(0, U_\theta(r), 0)$ in a cylindrical coordinate system (r, θ, z) which is rotating about the vertical axis at angular velocity $\Omega_b = f/2$ where f is the Coriolis parameter. The fluid is assumed to be inviscid and stably stratified with a constant Brunt-Väisälä frequency N. We subject this vortex to infinitesimally small three-dimensional perturbations of velocity $\tilde{\mathbf{u}} = (\tilde{u}_r, \tilde{u}_\theta, \tilde{u}_z)$, pressure $\tilde{p}$ and density $\tilde{\rho}$, written in the form

$$(\tilde{\mathbf{u}}, \tilde{p}, \tilde{\rho}) = (\mathbf{u}(r), p(r), \rho(r))e^{-i\omega t + ikz + im\theta} + c.c, \tag{1}$$

where c.c denotes the complex conjugate, ω is the complex frequency, k is the vertical wavenumber and m is the azimuthal wavenumber. Under the Boussinesq approximation, the linearized equations of momentum, density conservation and continuity for the perturbations read

$$isu_r - \left(f + \frac{2U_\theta}{r}\right) u_\theta = -\frac{d}{dr}\left(\frac{p}{\rho_0}\right), \tag{2}$$

$$isu_\theta + (f + \zeta)\, u_r = -\frac{imp}{\rho_0 r}, \tag{3}$$

$$isu_z = -ik\frac{p}{\rho_0} - \frac{g}{\rho_0}\rho, \tag{4}$$

$$is\rho = N^2\frac{\rho_0}{g}u_z, \tag{5}$$

$$\frac{1}{r}\frac{d}{dr}(ru_r) + \frac{im}{r}u_\theta + iku_z = 0, \tag{6}$$

where $s = -\omega + mU_\theta/r$ is the Doppler-shifted frequency, $\zeta = \frac{1}{r}\frac{d}{dr}(rU_\theta)$ is the axial vorticity of the vortex, g is the gravity and ρ_0 is a constant reference density. From the equations (2)-(6), a single equation for the pressure p can be deduced

$$\frac{d^2p}{dr^2} + \left(\frac{1}{r} - \frac{\Delta'}{\Delta}\right)\frac{dp}{dr} + \left[-\frac{k^2}{N^2 - s^2}\Delta - \frac{m^2}{r^2} + \frac{m\Delta}{rs}\left(\frac{f + \frac{2U_\theta}{r}}{\Delta}\right)'\right] p(r) = 0, \tag{7}$$

where prime denotes differentiation with respect to r and $\Delta(r) = (f + \zeta)(f + \frac{2U_\theta}{r}) - s^2$[13,14]. Due to the symmetry $\omega(k, m) = \omega(-k, m) = -\omega^*(-k, -m)$, we consider hereafter only positive k and m. Moreover, we assume that the fluid is strongly stratified so that the hydrostatic approximation can be applied: $N >> |s|$ (i.e. $N^2 - s^2 \approx N^2$). Then, (7) depends only on k and N through the rescaled vertical wavenumber $\tilde{k} = \frac{k}{N}$ owing to the self-similarity of strongly-stratified fluids. This assumption also implies that there is no singularity where $|s| = N$.

As a base flow, we first consider the Rankine vortex: $U_\theta(r) = \Omega r$ for $r < R$ and $U_\theta(r) = \Omega R^2/r$ for $r > R$, where R is the radius of the vortex core, and then a smoothed Rankine vortex in Sec. **VI**. We impose the boundary conditions that the perturbations are nonsingular at the vortex center $r = 0$ and decays exponentially or radiates energy outward as $r \to \infty$. For the Rankine vortex, we also have to apply the kinematic and dynamic boundary conditions at the boundary of the vortex core $r = R$, which enforce the continuity of the radial velocity and the pressure: $u_r(R^-) = u_r(R^+),\ p(R^-) = p(R^+)$. By expressing u_r in terms of p by means of (2)-(3), these boundary conditions lead to the dispersion relation

$$\frac{p'(R^+)}{p(R^+)} = \frac{\Delta(R^+)}{\Delta(R^-)}\frac{p'(R^-)}{p(R^-)} - \frac{m(f + 2\Omega)}{Rs(R)}\left[1 - \frac{\Delta(R^+)}{\Delta(R^-)}\right]. \tag{8}$$

The non-singular solution of (7) inside the vortex core $r < R$ is

$$p(r) \sim I_m\left(\tilde{k}r\sqrt{(f + 2\Omega)^2 - (-\omega + m\Omega)^2}\right), \tag{9}$$

where I_m is the modified Bessel function of the first kind of order m. When ω is purely real, I_m increases exponentially with r when $|f + 2\Omega| > |-\omega + m\Omega|$ and is wavelike when $|f+2\Omega| < |-\omega+m\Omega|$. Outside the vortex core $r > R$, (7) needs to be integrated numerically. The integration is performed inward starting far outside the vortex core $r >> R$ from the asymptotic solution which satisfies the boundary condition for $r \to \infty$

$$p(r) \sim H_m^{(1)}\left(\tilde{k}r\sqrt{\omega^2 - f^2}\right), \tag{10}$$

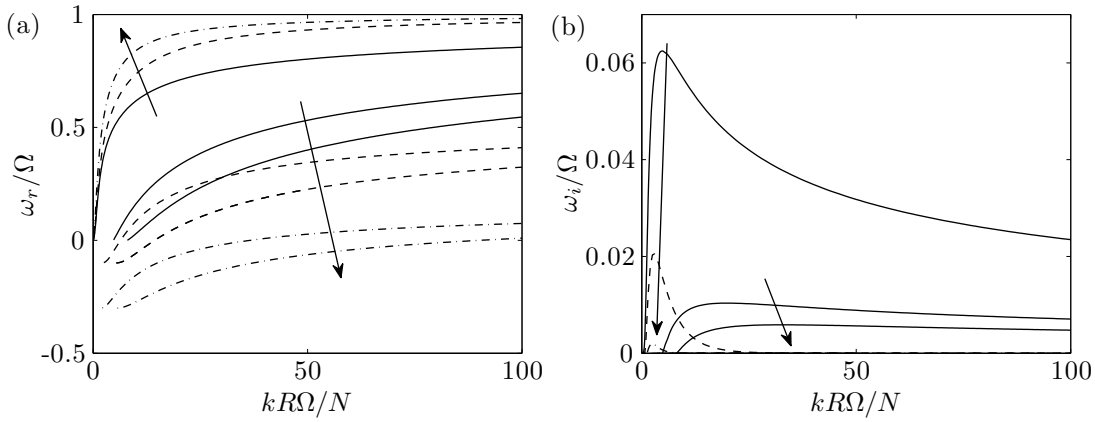

FIG. 1. (a) Frequency and (b) growth rate as a function of the rescaled vertical wavenumber $kR\Omega/N$ for $m = 1$ for different Coriolis parameters: $f/\Omega = 0$ (solid lines), $f/\Omega = 0.1$ (dashed lines) and $f/\Omega = 0.3$ (dash-dot lines). Only the first three branches are shown. f increases in the direction of the arrows. For $f/\Omega = [0.1, 0.3]$, growth rates of the higher branches are not visible because they are too small.

where $H_m^{(1)}$ is the Hankel function of the first kind of order m. For real ω, $H_m^{(1)}$ behaves as an outgoing wave when $|\omega| > |f|$ while it decreases exponentially with r when $|\omega| < |f|$. Starting from an initial guess value for ω, the secant method is used to find the value of ω which satisfy the dispersion relation (8).

III. NUMERICAL RESULTS

A. Cyclonic rotation

Figure 1 shows the frequency ω_r and growth rate ω_i of the first three branches for $m = 1$ for different non-negative values of the Coriolis parameter f. The results found previously for $f/\Omega = 0$ are shown to serve as a reference[6]. The frequency of the first branch starts from the 2D dispersion relation $\omega = (m-1)\Omega = 0$ at zero vertical wavenumber k independently of f. As f increases, the frequency increases with k more rapidly but it always tends to Ω as $k \to \infty$ regardless of f. The corresponding growth rate ω_i remains also maximum for a finite k but the maximum growth rate decreases rapidly as f increases. We have found that the maximum growth rate becomes of order of $O(10^{-5}\Omega)$, i.e. negligibly small when $f \gtrsim 0.5\Omega$. In contrast to the first branch, the frequency of the next branches start around $\omega = -f$ at

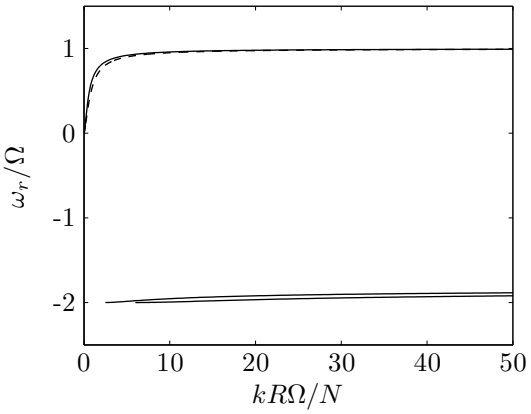

FIG. 2. Frequency of the first three branches for $f/\Omega = 2$ and $m = 1$. Solid lines are numerical results. The dashed line shows the quasi-geostrophic dispersion relation (11).

non-zero k and tends to $\omega_r = \Omega - \sqrt{f(f+2\Omega)}$ as $k \to \infty$. The growth rates of the next branches are much smaller than for the first branch and they decreases more rapidly as f increases. For example, the maximum growth rate ω_i of the second branch becomes of order $O(10^{-5}\Omega)$ as soon as $f \gtrsim 0.05\Omega$.

Figure 2 shows the frequency of the first three branches for $m = 1$ when f/Ω is larger: $f/\Omega = 2$. The frequency of the branches still lies in the same range: $0 < \omega_r < \Omega$ for the first branch and $-f < \omega_r < \Omega - \sqrt{f(f+2\Omega)}$ for the next branches but the growth rate is now strictly zero. As seen in figure 2, the frequency of the first branch is well predicted by the dispersion relation of the Rankine vortex in the quasi-geostrophic limit (i.e. $f >> \Omega$)[15],

$$\omega = m\Omega \left[1 - 2I_m\left(\frac{kRf}{N}\right) K_m\left(\frac{kRf}{N}\right) \right], \tag{11}$$

where I_m and K_m are the modified Bessel functions of order m. In contrast, the next branches have a frequency of order $|f|$. Hence, they are not captured by the quasi-geostrophic dispersion relation (11) because quasi-geostrophy assumes $O(|\omega|, |\Omega|) << |f|$.

Figure 3 displays some examples of pressure eigenfunctions. We clearly see a radiating inertia-gravity wave train outside the vortex core for the eigenmode of the first branch (figure 3a and b). However, the amplitude of this radiating wave is attenuated when f increases from $f/\Omega = 0$ to $f/\Omega = 0.3$. In contrast, the pressure eigenfunction of the second branch for $f/\Omega = 0.3$ (figure 3c) has only one node outside the vortex core and no radiating wavetrain. The next branches are similar except that the number of nodes outside the vortex core is $n-1$, where n is the branch number. These distinct properties will be explained in Sec **IV**.

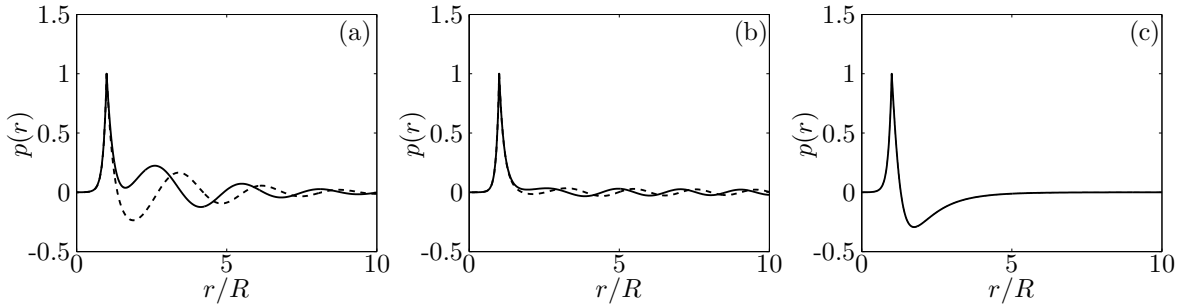

FIG. 3. Pressure eigenfunction for $kR\Omega/N = 5$ and (a) $f/\Omega = 0$, (b) $f/\Omega = 0.3$ for the first branch and (c) $f/\Omega = 0.3$ for the second branch. Solid lines and dashed lines represent the real and imaginary parts, respectively.

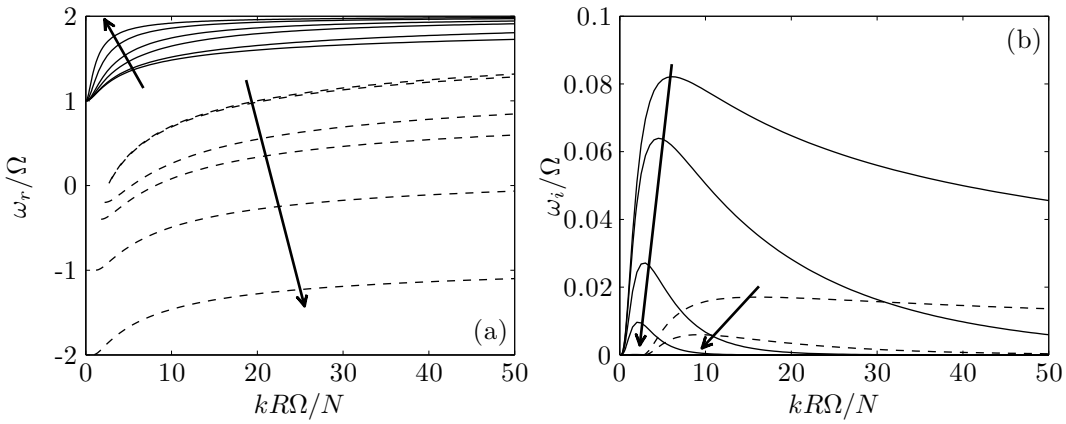

FIG. 4. Similar to FIG. 1 but for $m = 2$, (a) frequency ω_r and (b) growth rate ω_i for $m = 2$ for the first branch (solid lines) and the second branch (dashed lines) for $f/\Omega = [0, 0.04, 0.2, 0.4, 1, 2]$. f/Ω increases in the direction of the arrows.

B. Variation with the azimuthal wavenumber

Figure 4 shows the frequency and growth rate for $m = 2$. When f varies, the frequency of the first branch now lies in the range $[\Omega, 2\Omega]$ while the frequency of the next branches lies in the range $-f < \omega_r < 2\Omega - \sqrt{f(f + 2\Omega)}$. More generally, we have found for arbitrary non-zero azimuthal wavenumber m that the frequency of the first branch lies in the range

$$(m - 1)\Omega \leq \omega_r < m\Omega, \tag{12}$$

while the frequency range of the next branches is

$$-f < \omega_r < m\Omega - \sqrt{f(f + 2\Omega)}. \tag{13}$$

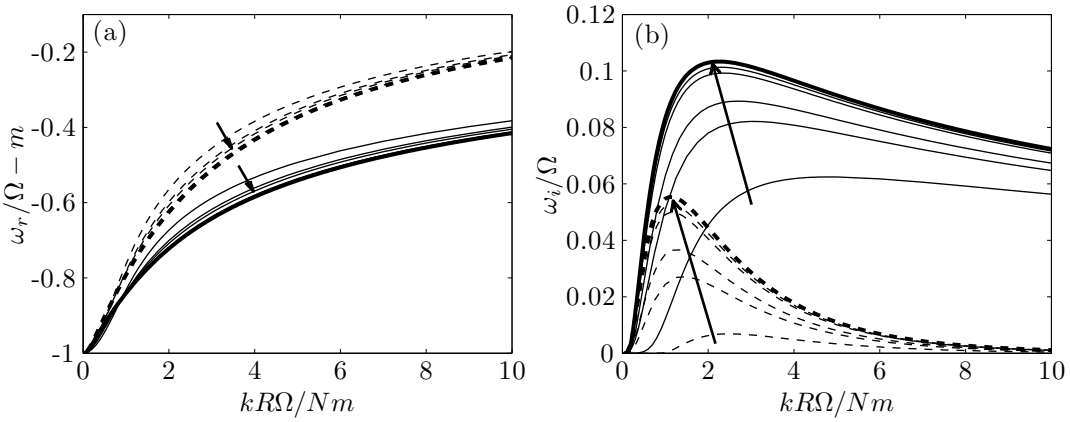

FIG. 5. (a) Rescaled frequency $\omega_r/\Omega - m$ and (b) growth rate ω_i of the first branch as a function of rescaled vertical wavenumber $kR\Omega/(Nm)$ for $m = [1, 2, 3, 10, 20]$ and for $f/\Omega = 0$ (solid lines) and $f/\Omega = 0.2$ (dashed lines). Bold lines have been obtained from the large m asymptotic equation (14). m increases in the direction of the arrows.

The particular case of the axisymmetric perturbation $m = 0$ is treated in appendix.

The maximum growth rate of the first branch for $m = 2$ and for $f = 0$ is $\omega_i \approx 0.08\Omega$ (for $kR\Omega/N \approx 6$) and is slightly larger than for $m = 1$ ($\omega_i \approx 0.05\Omega$ for $kR\Omega/N \approx 5$). Actually, for larger m, the maximum growth rate continues to increase monotonically with m but the corresponding eigenmode concentrates near $r = R$. Following[16], an asymptotic analysis can be performed for $m >> 1$ by introducing the rescaled variables: $\bar{r} = m(r/R - 1)$, $\omega_0 = \omega/\Omega - m$, $k_1 = kR\Omega/(Nm)$ and $\bar{f} = f/\Omega$ where $(\bar{r}, \omega_0, k_1, \bar{f})$ will be assumed to be of order one. Then (7) for $r > R$ becomes at leading order in m:

$$\frac{d^2p}{d\bar{r}^2} + \bar{\Delta}\frac{d}{d\bar{r}}\left(\frac{1}{\bar{\Delta}}\right)\frac{dp}{d\bar{r}} + \left[-k_1^2\bar{\Delta} - 1 - \frac{4(\bar{f}+2)}{\bar{\Delta}}\right]p(\bar{r}) = O\left(\frac{1}{m}\right), \tag{14}$$

where $\bar{\Delta}(\bar{r}) = \bar{f}(\bar{f}+2) - (\omega_0 + 2\bar{r})^2$. This equation is equivalent to the one obtained by[16] for the radial velocity. It has to be solved numerically except for $f = 0$ where an analytical solution exists

$$p(\bar{r}) = C_0\left(\bar{r} + \frac{\omega_0}{2}\right)D_{-\frac{1}{2}-\frac{i}{4k_1}}\left(2\sqrt{k_1}(\bar{r} + \frac{\omega_0}{2})e^{-i\frac{\pi}{4}}\right), \tag{15}$$

where D_ν denotes the parabolic cylinder function of order ν and C_0 is a constant. Note that (15) matches the outgoing wave boundary condition (10) as $\bar{r} \to \infty$.

In figure 5, we show the rescaled frequency $\omega_r/\Omega - m$ and the growth rate ω_i as a function of the rescaled vertical wavenumber $kR\Omega/(Nm)$ for $f/\Omega = 0$ and $f/\Omega = 0.2$. We see that

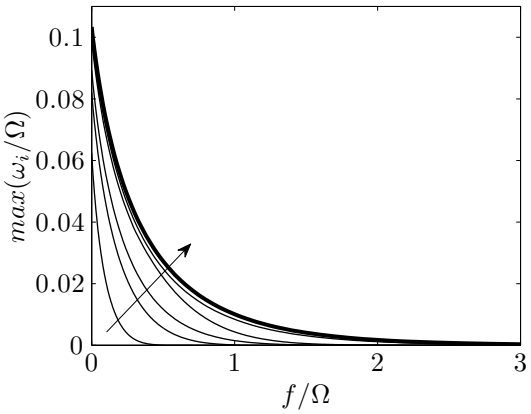

FIG. 6. Maximum growth rate as a function of the Coriolis parameter for different azimuthal wavenumbers. Thin and thick solid lines represent numerical results for $m = [1, 2, 3, 10, 20]$ and asymptotic results for $m >> 1$, respectively. m increases in the direction of the arrow.

the numerical results tend to the asymptotic results (bold lines) as m increases for both values of f/Ω. The maximum growth rate for $f = 0$ is approximately $\omega_i \approx 0.1\Omega$ and is reached around $kR\Omega/(Nm) \approx 2$. These values are very close to those obtained in the case of the potential flow around a rotating cylinder[16]. This indicates that the potential flow of the Rankine vortex is responsible for the instability whereas the vortex core plays no active role. However, the frequency range for the Rankine vortex (figure 5a) and the flow around a rotating cylinder are different since the first branch is absent in the latter flow owing to the impermeable boundary condition at $r = R$.

Figure 6 summarizes the effect of a cyclonic rotation on the radiative instability: the maximum growth rate is plotted as a function of the Coriolis parameter f for different azimuthal wavenumbers m. We see that the maximum growth rate $m = \infty$ (bold line) quickly decreases as f increases but remains positive whatever f. We can remark that the maximum growth rate tends to the asymptotic maximum growth rate (bold line) as m increases. For finite m, the growth rate goes to zero at a particular value of f/Ω.

IV. WKBJ ANALYSIS

A. Formulation

The numerical results obtained in the previous section can be explained by means of a WKBJ analysis for large rescaled vertical wavenumber $\tilde{k}$[6,7,17]. For large $\tilde{k}$, the equation (7) becomes at leading order

$$\frac{d^2p}{dr^2} + \left(\frac{1}{r} - \frac{\Delta'}{\Delta}\right)\frac{dp}{dr} + \left[-\tilde{k}^2\Delta + O(1)\right]p(r) = 0. \tag{16}$$

The WKBJ approximation focus on rapid exponential behaviours of the solution[18] so that the $O(1)$ term in (16) can be neglected at leading order. The WKBJ approximation of the solution of (16) is

$$p(r) \sim \frac{(-\Delta)^{1/4}}{r^{1/2}}\left[A\exp\left(i\tilde{k}\int_{r_t}^{r}\sqrt{-\Delta}dt\right) + B\exp\left(-i\tilde{k}\int_{r_t}^{r}\sqrt{-\Delta}dt\right)\right], \tag{17}$$

where A, B are constants and r_t is a turning point where $\Delta(r_t) = 0$. If the eigenfrequency ω is predominantly real (i.e. $\omega_r >> \omega_i$) and $\Delta < 0$, the approximation (17) is wavelike. Conversely if $\Delta > 0$, the WKBJ approximation has an exponential behaviour and (17) can be rewritten

$$p(r) \sim \frac{\Delta^{1/4}}{r^{1/2}}\left[C\exp\left(-\tilde{k}\int_{r_t}^{r}\sqrt{\Delta}dt\right) + D\exp\left(\tilde{k}\int_{r_t}^{r}\sqrt{\Delta}dt\right)\right], \tag{18}$$

where C and D are constants. The first term in (18) decays exponentially with r whereas the second term increases with r. Regarding the wakelike solution (17), we can define the phase velocity v_ϕ and the group velocity v_g in the radial direction of each term. For the first term, they are

$$v_\phi = \frac{\omega_r}{l_r} = \frac{\omega_r}{\tilde{k}Re\left(\sqrt{-\Delta}\right)}, \qquad v_g = \frac{\partial\omega_r}{\partial l_r} = \frac{Re\left(\sqrt{-\Delta}\right)}{\tilde{k}Re\left(-s\right)} \tag{19}$$

where $l_r = Re\left[\frac{\partial}{\partial r}\left(\tilde{k}\int_{r_t}^{r}\sqrt{-\Delta}dt\right)\right]$ is the local radial wavenumber. The sign of the phase velocity v_ϕ depends on the sign of the frequency ω_r while the sign of the group velocity v_g depends on the sign of the Doppler-shifted frequency s. This implies that the group velocity v_g changes its sign at the critical point r_c where $s(r_c) = 0$. As $r \to \infty$, the group velocity is $v_g = \sqrt{\omega_r^2 - f^2}/(\tilde{k}\omega_r)$. Therefore, when $\omega_r > f > 0$, the first term in (17) represents an outgoing wave whereas the second term corresponds to an incoming wave.

The WKBJ approximations (17) and (18) are valid except at the turning point r_t where $\Delta(r_t) = 0$[18]. In the neighborhood of the turning point r_t, (7) approximates at leading order to

$$\frac{\mathrm{d}^2 p}{\mathrm{d}\tilde{r}^2} - \frac{1}{\tilde{r}}\frac{\mathrm{d}p}{\mathrm{d}\tilde{r}} \mp \tilde{r}p = O(\epsilon), \tag{20}$$

where $\epsilon = \frac{1}{(\pm\Delta'(r_t)\tilde{k}^2)^{1/3}}$ and $\tilde{r} = \frac{r-r_t}{\epsilon}$. The sign $\pm$ corresponds to the sign of $\Delta'(r_t)$. The solution of (20) is

$$p(\tilde{r}) = a_\pm Ai'(\pm\tilde{r}) + b_\pm Bi'(\pm\tilde{r}), \tag{21}$$

where a_+, a_-, b_+, b_- are constants, Ai, Bi denote Airy's functions[19]. From the asymptotic behaviour of the Airy functions for $\tilde{r} \to +\infty$ and $\tilde{r} \to -\infty$, the WKBJ approximations in the regions $r > r_t$ and $r < r_t$ can be matched[18].

B. Radial structure of the WKBJ approximations

To determine the sign of Δ and the location of the turning point r_t, it is useful to define the epicyclic frequencies[17]

$$\omega_\pm(r) = m\frac{U_\theta}{r} \pm \sqrt{(f+\zeta)\left(f + \frac{2U_\theta}{r}\right)}, \tag{22}$$

for which $\Delta = 0$. When the frequency ω_r lies in the interval $\omega_- < \omega_r < \omega_+$, Δ is positive so that the WKBJ approximations are exponential. On the other hand, Δ is negative when $\omega_r > \omega_+$ or $\omega_r < \omega_-$, and the WKBJ approximations are wavelike.

Figure 7 shows two examples of the epicyclic frequencies for two different values of f/Ω for $m = 1$. They are typical of all the configurations that can be encountered for any azimuthal wavenumber $m \geq 1$ in the case of a cyclonic rotation. We have also plotted the critical frequency $\omega_c(r) = mU_\theta/r$ with dashed lines to indicate where the group velocity changes its sign. Since the epicyclic frequencies always decrease with r for $r > R$, we may distinguish three different ranges of frequencies:

(I): $max\left(\omega_+(\infty), \omega_-(R^+)\right) < \omega_r < \omega_+(R^+)$

(II): $min\left(\omega_+(\infty), \omega_-(R^+)\right) < \omega_r < max\left(\omega_+(\infty), \omega_-(R^+)\right)$

(III): $\omega_-(\infty) < \omega_r < min\left(\omega_+(\infty), \omega_-(R^+)\right)$.

The frequency ranges $\omega_r > \omega_+(R^+)$ or $\omega_r < \omega_-(\infty)$ are not considered because there is no eigenfunction. Indeed, the outer solution is wavelike for any $r > R$ but an outgoing WKBJ approximation (first term in (17)) can never satisfy the dispersion relation (8).

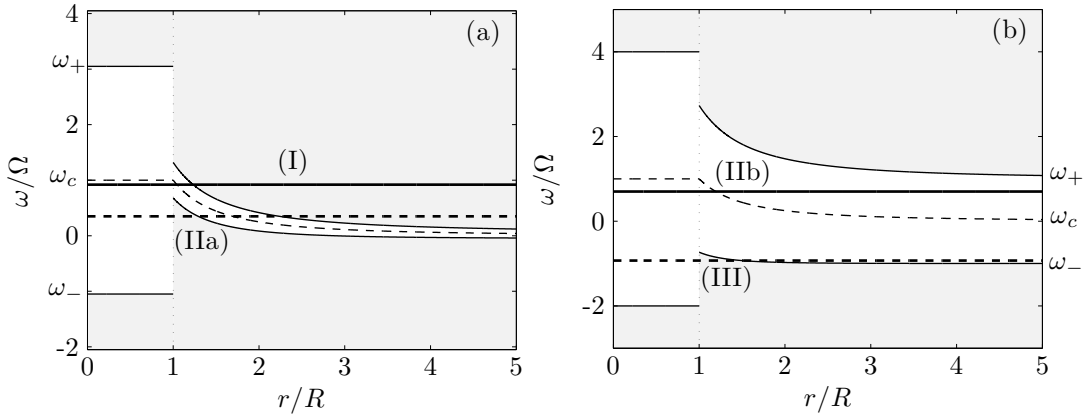

FIG. 7. Epicyclic frequencies ω_+ and ω_- (solid lines) and critical frequency (dashed lines) as a function of r for (a) $f/\Omega = 0.05$ and (b) $f/\Omega = 1$ for $m = 1$. Dotted lines represent the boundary of the vortex core. Thick solid and dashed lines show examples of the frequency ω_r for the four different configurations (I, IIa, IIb, III). The regions where the WKBJ approximations are wavelike (i.e. $\Delta < 0$) are shaded.

In the frequency range (I), there is a single turning point r_{t2} where the frequency ω is equal to $\omega = \omega_+(r_{t2})$, and the WKBJ approximations are wavelike for $r > r_{t2}$ and exponential-like for $r < r_{t2}$ (see the example shown by a bold solid line in figure 7a). The configuration in the frequency range (II) depends on $\omega_+(\infty)$ and $\omega_-(R^+)$. When $\omega_-(R^+) > \omega_+(\infty)$ (configuration hereafter refered as IIa), there are two turning points r_{t2} and r_{t1} such that $\omega = \omega_-(r_{t1}) = \omega_+(r_{t2})$. The WKBJ approximations are exponential-like between r_{t1} and r_{t2}, and wavelike for $r > r_{t2}$ and $r < r_{t1}$ (see the thick dashed line in figure 7a). Note that the critical point r_c is enclosed between r_{t1} and r_{t2}. In contrast, when $\omega_-(R^+) < \omega_+(\infty)$ (case hereafter refered as IIb), there exists no turning point and the WKBJ approximations are exponential-like for any $r > R$ as for the example displayed by a bold solid line in figure 7(b). Finally, in the range (III), there is a single turning point r_{t1} and the WKBJ approximations are exponential-like for $r > r_{t1}$ and wavelike for $r < r_{t1}$ (see the example illustrated by a thick dashed line in figure 7b).

In figure 8, we have plotted the frequencies $\omega_+(R^+)$, $\omega_+(\infty)$, $\omega_-(R^+)$ and $\omega_-(\infty)$ as a function of the Coriolis parameter f. The type of configurations is indicated in each domain.[6,7] have shown that the radiative instability can exist when there exists two distinct wave regions, i.e. for the configuration (IIa). In this case, an incident wave (i.e. with positive group velocity) is reflected at the turning point r_{t1} and transmitted to an outgoing wave for

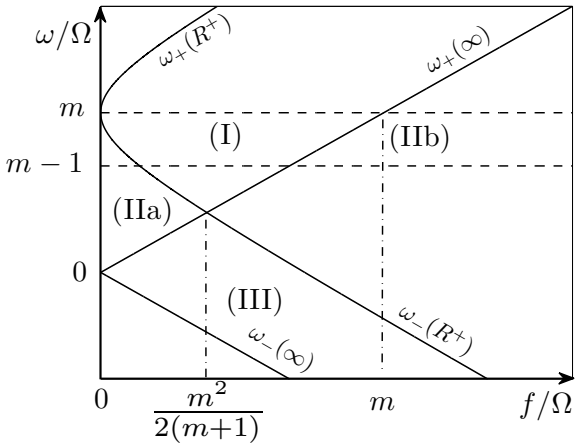

FIG. 8. Characteristic frequencies as a function of f/Ω. The labels refer to the structure of the WKBJ approximations described in the text. The dashed lines delimit the frequency range of the first branch $[(m-1)\Omega, m\Omega]$. The dashed-dotted lines show the thresholds for the radiative instability of the first and next branches.

$r > r_{t2}$ through the exponential region which is analogous to a potential barrier. However, because the group velocity is reversed at the critical point r_c in the potential barrier, the reflected wave for $r < r_{t1}$ has a larger amplitude than the incident wave. This phenomenon of over-reflection is the origin of the radiative instability. A condition for the existence of the radiative instability is therefore that the configuration (IIa) exists, i.e. $\omega_-(R^+) > \omega_+(\infty)$ (see figure 8) giving

$$m\Omega - \sqrt{f(f+2\Omega)} > f, \tag{23}$$

or in terms of the Rossby number Ro

$$Ro \equiv 2\Omega/f > \frac{4(m+1)}{m^2}. \tag{24}$$

However, we shall see in the next section that this condition is only sufficient but not necessary because the first branch is particular for the Rankine vortex.

We now derive in details the WKBJ approximations for each of the four possible configurations: (I), (IIa), (IIb), (III).

C. One turning point: case (I)

In the configuration (I), there is one turning point r_{t2} and the WKBJ approximations are wavelike for $r > r_{t2}$. In order to impose that the wave is outgoing for $r \to \infty$, we put $B = 0$

in (17). Then, the matching WKBJ approximation in the region $r < r_{t2}$ is

$$p(r) \sim A\mathrm{e}^{-\frac{\mathrm{i}\pi}{4}} \frac{\Delta^{1/4}}{r^{1/2}} \left[\frac{1}{2} \mathrm{e}^{-\tilde{k}\int_r^{r_{t2}} \sqrt{\Delta(t)}dt} + i\mathrm{e}^{\tilde{k}\int_r^{r_{t2}} \sqrt{\Delta(t)}dt} \right]. \tag{25}$$

This approximation can be directly inserted in the dispersion relation (8). We can also further expand the dispersion relation in powers of $\tilde{k}$ to obtain explicitly the eigenfrequency. This gives at leading order

$$\omega_r = m\Omega - \frac{\alpha}{R\tilde{k}} \ , \ \omega_i = \frac{\alpha^2}{2mR\Omega} \sqrt{f(f+2\Omega)} \frac{W}{\tilde{k}}, \tag{26}$$

where $\alpha = 2m\Omega / \left(f + \sqrt{f(f+2\Omega)} \right)$ and $W = \exp\left(-2\tilde{k} \int_R^{r_{t2}} \sqrt{\Delta(t)}dt \right)$. The frequency tends to $m\Omega$ as $\tilde{k} \to \infty$ and corresponds to the first branch. Surprisingly, its growth rate is positive and of order $O(W/\tilde{k})$ even if there is a single turning point. In fact, this first branch is particular because it originates from the vorticity jump present at $r = R$ in the Rankine vortex. This discontinuity acts like an infinitely small wave region which play the role of the second wave region needed for the radiative instability in the case of continuous vortex profiles[7].

For this reason, the first branch is unstable as long as there exists an outer wave region, i.e. $\omega_r > min(\omega_+) = f$. Since the frequency range of the first branch is observed to be always in the range $[(m-1)\Omega, m\Omega]$, it is unstable for some frequency provided that $f < m\Omega$ (see figure 8), i.e.

$$Ro > \frac{2}{m}. \tag{27}$$

The first branch is therefore unstable over a wider range of Rossby number than the next branches (see Eq. 24).

D. One turning point: case (III)

In the configuration (III), a turning point r_{t1} exists and the solution is now exponential-like for $r > r_{t1}$. In order to impose the boundary condition at $r = \infty$, we put $D = 0$ in (18). The matching WKBJ approximation in the region $r < r_{t1}$ is then

$$p(r) \sim \mathrm{e}^{\frac{\mathrm{i}\pi}{4}} \frac{(-\Delta)^{1/4}}{r^{1/2}} \left[A_{I1} \mathrm{e}^{i\tilde{k}\int_r^{r_{t1}} \sqrt{-\Delta(t)}dt} + A_{R1} \mathrm{e}^{i\tilde{k}\int_r^{r_{t1}} \sqrt{-\Delta(t)}dt} \right], \tag{28}$$

where $A_{I1} = C$ and $A_{R1} = -iC$. By inserting (28) in (8), we obtain the asymptotic dispersion relation

$$\tilde{k} \int_R^{r_{t1}} \sqrt{-\Delta}dt + \frac{i}{4} \log(\mathcal{R}) = n\pi, \tag{29}$$

where n is the branch number and $\mathcal{R}$ is the reflection coefficient at r_{t1}

$$\mathcal{R} = \mathcal{R}_1 \equiv A_{R1}^2/A_{I1}^2 = \mathrm{e}^{-i\pi}. \tag{30}$$

As $\tilde{k} \to \infty$, the integral $\int_R^{r_{t1}} \sqrt{-\Delta} dt$ should tend to zero in order to satisfy (29). This implies that the wave region concentrates near the vortex core R as $\tilde{k} \to \infty$. By using this feature, we can express the eigenfrequency in powers of $\tilde{k}$

$$\begin{aligned} \omega &= m\Omega - \sqrt{f(f+2\Omega)} - \beta/\left(\tilde{k}R\Omega\right)^{2/3}, \\ \beta &= \left[\tfrac{3\Omega^2}{\sqrt{2}}\left(n\pi - \tfrac{i}{4}\log\left(\mathcal{R}\right)\right)\left(m\sqrt{f(f+2\Omega)} - f\right)\right]^{2/3}/\sqrt{f(f+2\Omega)}, \end{aligned} \tag{31}$$

where $\mathcal{R} = \mathcal{R}_1$. Note that the frequency tends to $\omega_r = m\Omega - \sqrt{f(f+2\Omega)}$ as $\tilde{k} \to \infty$ as observed for all the branches except the first one. Since the absolute value of the reflection coefficient $|\mathcal{R}_1|$ is unity (i.e. perfect reflection), β is purely real so that the growth rate ω_i is zero. Hence, this configuration corresponds to neutral waves confined between R and r_{t1}.

E. Two turning points: case (IIa)

In the configuration (IIa), there are two turning points r_{t1} and r_{t2} (with $r_{t1} < r_{t2}$) enclosing a potential barrier. The WKBJ approximation for $r > r_{t2}$ is an outgoing wave like in subsection **C**. If the two turning points are well separated, the approximation for $r_{t1} < r < r_{t2}$ is also the same as in **C**. The WKBJ approximation which matches (25) for $r < r_{t1}$ is then

$$p(r) = \frac{(-\Delta)^{1/4}}{r^{1/2}}\left[A_{I2}\mathrm{e}^{i\tilde{k}\int_r^{r_{t1}}\sqrt{-\Delta(t)}dt} + A_{R2}\mathrm{e}^{-i\tilde{k}\int_r^{r_{t1}}\sqrt{-\Delta(t)}dt}\right], \tag{32}$$

where $A_{I2} = i(X - 1/(4X))A$, $A_{R2} = (X + 1/(4X))A$ and $X = \exp\left(\tilde{k}\int_{r_{t1}}^{r_{t2}}\sqrt{\Delta(t)}dt\right)$. The first term of (32) is an incident wave toward r_{t1} since its group velocity $v_g = -Re\left(\sqrt{-\Delta}\right)/(\tilde{k}Re(-s))$ is positive. However, its phase velocity $v_\phi = -\omega_r/\left(\tilde{k}Re\left(\sqrt{-\Delta}\right)\right)$ is negative. The second term corresponds to the reflected wave but its amplitude A_{R2} is larger than the amplitude of the incident wave A_{I2}. By inserting (32) in (8), we obtain the same asymptotic dispersion relation as (29) with the reflection coefficient

$$\mathcal{R} = \mathcal{R}_2 \equiv A_{R2}^2/A_{I2}^2 = \mathrm{e}^{-i\pi}\left(\frac{4X^2+1}{4X^2-1}\right)^2. \tag{33}$$

The formula (31) with $\mathcal{R} = \mathcal{R}_2$ therefore also applies to this case. Because of the over-reflection, the absolute value of the reflection coefficient $|\mathcal{R}_2|$ is now larger than unity since $X > 1$ so that the coefficient β in (31) is complex and leads to the radiative instability. The stabilizing effect of the cyclonic rotation on the radiative instability can be understood from (33). When f increases from zero, the two turning points r_{t1} and r_{t2} move apart from each other, i.e. the potential barrier widens, implying that X increases exponentially. Therefore, the reflection coefficient $|\mathcal{R}_2|$ tends to unity when f increases meaning that the radiative instability is stabilized.

When f is close to zero (i.e. $Ro >> 1$), the two turning points are close together so that the assumption of well-separated turning points is not valid. Instead, we can derive a local equation in the neighborhood of the critical point $r_c = R\sqrt{m\Omega/\omega}$ which is located in the middle between the two turning points r_{t1} and r_{t2}. Around the critical point, we can approximate the Doppler-shifted frequency s and the function Δ as $s(r) \sim -\sqrt{\frac{4\omega^3}{R^2 m\Omega}}\epsilon\tilde{r}$, $\Delta(r) \sim \frac{4\omega^3}{R^2 m\Omega}\epsilon^2(\frac{R^2}{2\omega^2}\frac{f}{\epsilon^2} - \tilde{r}^2)$ where $\tilde{r} = \frac{1}{\epsilon}(r - r_c)$ and $\epsilon = (\frac{R^2 m\Omega}{4\tilde{k}^2\omega^3})^{1/4}$. Assuming that f is small of order $f \sim O(\epsilon^2)$, (7) becomes at leading order in ϵ:

$$\frac{d^2p}{d\tilde{r}^2} - \frac{2\tilde{r}}{\tilde{r}^2 - a}\frac{dp}{d\tilde{r}} + \left(\tilde{r}^2 - a + \frac{2}{\tilde{r}^2 - a}\right)p(\tilde{r}) = 0, \tag{34}$$

where $a = \frac{R^2 f}{2\omega^2\epsilon^2} = \frac{f\tilde{k}R}{\sqrt{m\Omega\omega}}$. The solution of (34) is

$$p(\tilde{r}) = b_1 e^{\frac{i}{2}\tilde{r}^2}\left[U\left(i\frac{a}{4} - \frac{1}{4}, -\frac{1}{2}, -i\tilde{r}^2\right) + \frac{(ia-1)}{2}U\left(i\frac{a}{4} + \frac{3}{4}, \frac{1}{2}, -i\tilde{r}^2\right)\right], \tag{35}$$

where U denotes the Kummer function[19] and $b_1 = \frac{A}{\sqrt{\tilde{k}r_c\epsilon}}e^{\left(\frac{i\pi}{8} + \frac{a\pi}{8}\right)}(\frac{a}{4e})^{\frac{ia}{4}}$. By matching (35) to an outgoing wave for $\tilde{r} \to +\infty$[20], we find that the WKBJ approximation for $r < r_{t1}$ which matches (35) for $\tilde{r} \to -\infty$, is the same as (32) except that A_{I2} and A_{R2} are replaced by

$$\tilde{A}_{I2} = A\left[\frac{-2\pi e^{(\frac{i\pi}{4} + \frac{a\pi}{4})}}{\Gamma(i\frac{a}{4} + \frac{5}{4})\Gamma(-i\frac{a}{4} - \frac{1}{4})} - 1\right], \quad \tilde{A}_{R2} = A\left(i\frac{a}{4}\right)^{i\frac{a}{2}} e^{\frac{a}{2}(\pi - i)}\frac{2\pi}{\Gamma(i\frac{a}{4} + \frac{5}{4})\Gamma(i\frac{a}{4} - \frac{1}{4})}, \tag{36}$$

respectively, where Γ is the Gamma function. The asymptotic dispersion relations are then the same as (29) and (31) with

$$\mathcal{R} = \tilde{\mathcal{R}}_2(a) = \tilde{A}_{R2}^2/\tilde{A}_{I2}^2. \tag{37}$$

Figure 9 shows the reflection coefficient $\tilde{\mathcal{R}}_2$ as a function of $a = f\tilde{k}R/\sqrt{m\Omega\omega}$. We see that the reflection coefficient is $|\tilde{\mathcal{R}}_2| = 2$ for $a = 0$ (i.e. $f = 0$) as obtained by Billant

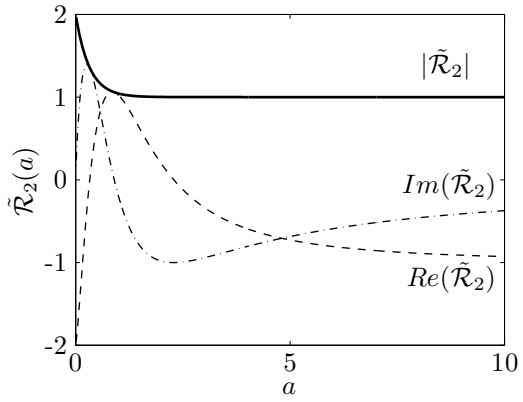

FIG. 9. Reflection coefficient $\tilde{\mathcal{R}}_2$ (37) as a function of a. The bold line, dashed line and dash-dot line are the absolute value, real part and imaginary part, respectively.

and Le Dizès[6]. When a increases, the reflection coefficient decreases quickly to unity. As mentioned before, this is because the size of the potential barrier $\delta r = r_{t2} - r_{t1} \approx 2\epsilon\sqrt{a}$ increases. The wave over-reflection becomes exponentially small when $a \gtrsim 1$. Since the parameter a is proportional to $f\tilde{k}/m$ (assuming $\omega \approx m\Omega$), this means that the radiative instability is stabilized as f increases all the more rapidly than $\tilde{k}$ is large and m is small.

F. No turning point: case (IIb)

Finally, when there is no turning point and Δ is positive, the WKBJ approximation (18) with $D = 0$ is valid everywhere for $r > R$. The frequency at leading order is then

$$\omega_r = m\Omega - \frac{\alpha}{R\tilde{k}}, \tag{38}$$

which is the same as (26) but the growth rate ω_i is zero. This configuration corresponds to the first branch when the Rossby number is smaller than $2/m$, i.e. when (27) is not satisfied.

G. Comparison with numerical results

The various asymptotic formula derived in the previous subsections are compared to the numerical results in figure 10 for $m = 1$ and $f/\Omega = [0, 0.1, 0.3]$. The WKBJ formula for the configurations with one turning point are shown by open circle for Eq. (26) (case I) and by crosses for Eq. (29)-(30) or squares for Eq. (30)-(31) (case III). In each case, the agreement is good at large vertical wavenumber, for both the frequency and the growth rate (but only

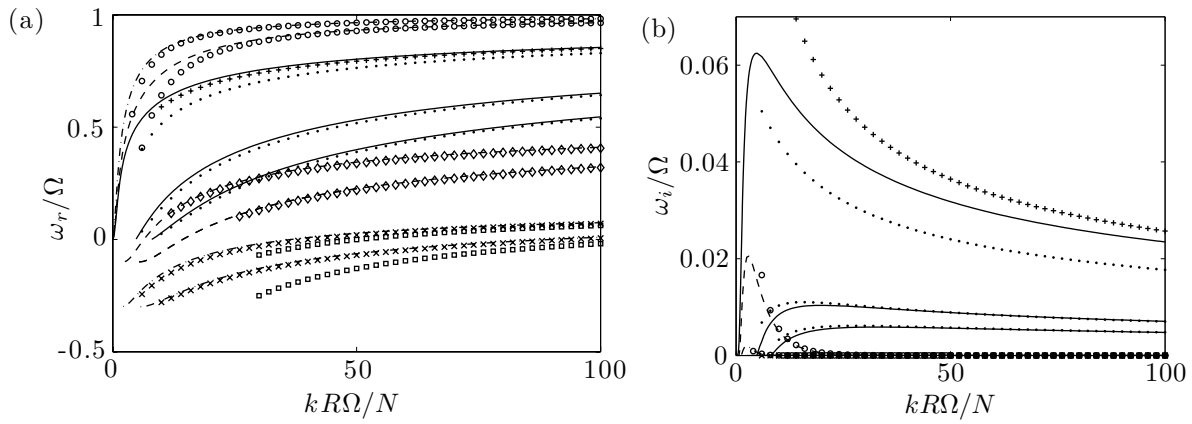

FIG. 10. Similar to figure 1, but compared with the WKBJ asymptotic results also plotted with symbols: •: two close turning points formula (29) using the reflection coefficient (37), +: two close turning points formula with the Kummer function (35), ∘: single turning point formula (26), ⋄: two separate turning points formula (29) with the reflection coefficient (33), ×: single turning point formula (29), □: single turning point formula (31).

the case (I) is unstable). The dotted lines represent the predictions of the formula (29) together with the reflection coefficient (37) for two close turning points (case IIa). We see that the agreement is good except for the first branch because the double turning point is too close to the boundary $r = R$. Instead of the WKBJ formula (29) with (37), the solution (35) of the local equation (34) can be used directly in the dispersion relation (8) to circumvent this problem. This refined approximation is in better agreement for large $\tilde{k}$ as shown by the symbols +. The symbols ⋄ represent the asymptotic dispersion relation (29) with the reflection coefficient (33) for two well-separated turning points, a configuration prevaling for the next branches for $f/\Omega = 0.1$. They are also in good agreements with numerical results.

The asymptotic dispersion relation (29) together with the reflection coefficient (37) for two close turning points is further tested in figure 11 for the second branch for small rotation. We see that the agreement is very good for large vertical wavenumber. It can be noticed that the growth rate is strongly reduced even if the Coriolis parameter is only of order $f/\Omega \sim O(0.01)$.

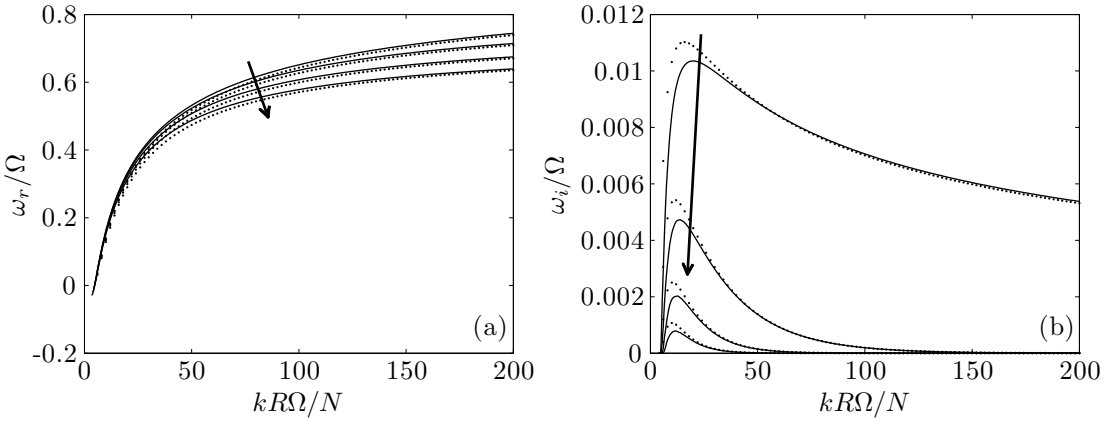

FIG. 11. (a) Frequency and (b) growth rate of the second branch for $m = 1$ for $f/\Omega = [0, 0.01, 0.02, 0.03]$. Solid lines and dotted lines are numerical and asymptotic results using the formula (29) and (37), respectively. f increases in the direction of the arrows.

V. ANTICYCLONIC ROTATION

A. Competition between the radiative and centrifugal instabilities

We now investigate the effect of an anticyclonic rotation ($f < 0$). According to the Rayleigh criterion[21,22], the Rankine vortex is unstable to the centrifugal instability when f is negative in the range $-2 < f/\Omega < 0$ (i.e. $Ro < -1$) since the Rayleigh discriminant $\phi = (f + \zeta)(2 + 2U_\theta/r)$ is negative. However, we shall show that the radiative instability continues to exist when f is slightly negative so that there is a competition between the radiative and centrifugal instabilities.

Figure 12 shows the growth rate of the first and second branches for $m = 1$ for $f/\Omega = [0, -0.005, -0.01, -0.015]$. As soon as f is non-zero, the growth rates increases with $\tilde{k}$ as $\tilde{k} \to \infty$ unlike for $f = 0$ because of the centrifugal instability. However, the peak of the radiative instability at finite $\tilde{k}$ remains present. In order to understand this behaviour, the local equation (34) around two close turning points and the resulting reflection coefficient $\tilde{\mathcal{R}}_2$ (37) can be used since they remain valid for $f < 0$ provided that $-\frac{3\pi}{2} < arg(a) < \frac{\pi}{2}$. Dotted lines in figure 12 represent the asymptotic growth rates obtained by inserting the reflection coefficient (37) into the asymptotic dispersion relation (29). They are in good agreements with the numerical results for all the values of f investigated.

For very large $\tilde{k}$, (29) can be further expanded in powers of $\tilde{k}$ and gives the same result

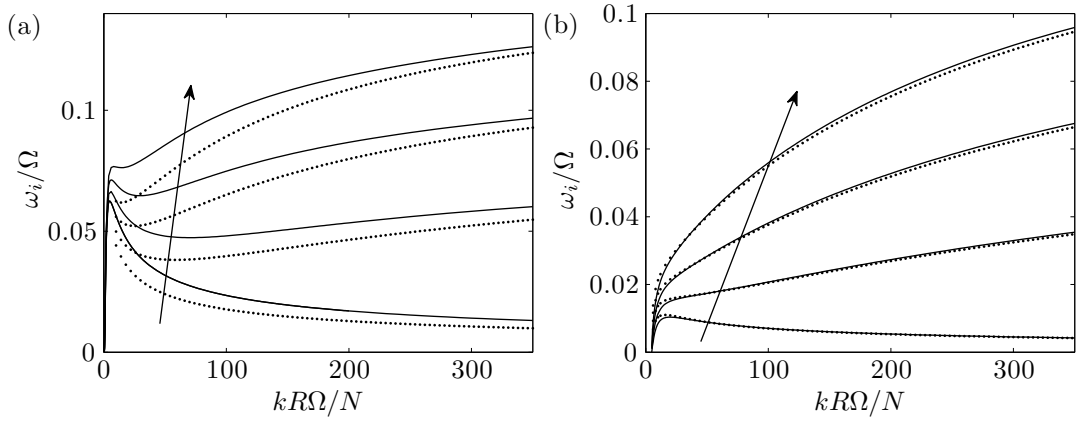

FIG. 12. Growth rate of (a) the first branch and (b) the second branch for $m = 1$ for $f/\Omega = [0, -0.005, -0.01, -0.015]$. Solid lines and dotted lines represent numerical and asymptotic results using the formula (29) and (37), respectively. f decreases from zero in the direction of the arrow.

as (31) with $\mathcal{R} = \tilde{\mathcal{R}}_2$. Since f is negative, there are now two imaginary terms in (31), the second term $\sqrt{f(f+2\Omega)}$ which corresponds to the maximum growth rate of the centrifugal instability as $\tilde{k} \to \infty$

$$\omega_i = \sqrt{-f(f+2\Omega)}, \tag{39}$$

and the last term involving β which is responsible for the radiative instability and reaches a maximum at finite $\tilde{k}$ and decays to zero as $\tilde{k} \to \infty$. This proves that there is coexistence of the centrifugal and radiative instabilities.

In order to investigate the competition between these two instabilities, figure 13 shows their maximum growth rates as a function of the inverse of the Rossby number. The growth rate peak at finite $\tilde{k}$ is associated to the maximum growth rate of the radiative instability whereas the maximum growth rate of the centrifugal instability is $\sqrt{-f(f+2\Omega)}$. The centrifugal instability becomes quickly the most dangerous instability for negative Ro but, interestingly, the radiative instability dominates the centrifugal instability when $Ro \lesssim -400$.

B. Results for $f/\Omega = O(-1)$

We now investigate larger negative values of f such that $f/\Omega = O(-1)$. Figure 14 shows a typical example of the frequency and growth rate for $m = 1$ for $f/\Omega = -0.4$. The frequency of the first branch starts from $\omega_r = (m-1)\Omega = 0$ at $\tilde{k} = 0$ and increases with $\tilde{k}$, like for cyclonic rotation. However, there is now another branch which starts from $\omega_r = |f|$

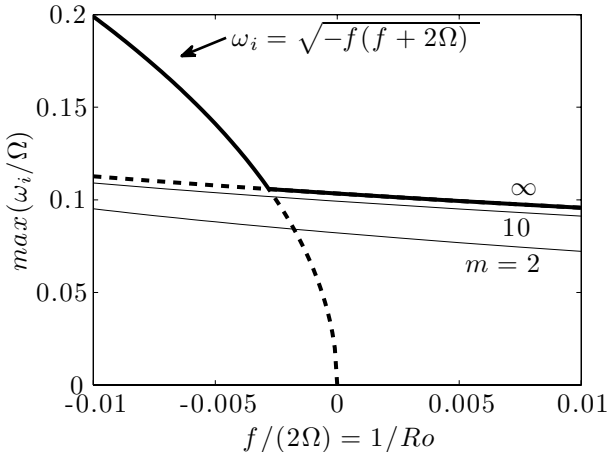

FIG. 13. Maximum growth rate of the radiative instability and the centrifugal instability as a function of the Rossby number $Ro = 2\Omega/f$. Solid lines are numerical results of the maximum growth rate of the radiative instability and bold lines are maximum growth rates obtained from (14) for the radiative instability and from (39) for the centrifugal instability, respectively.

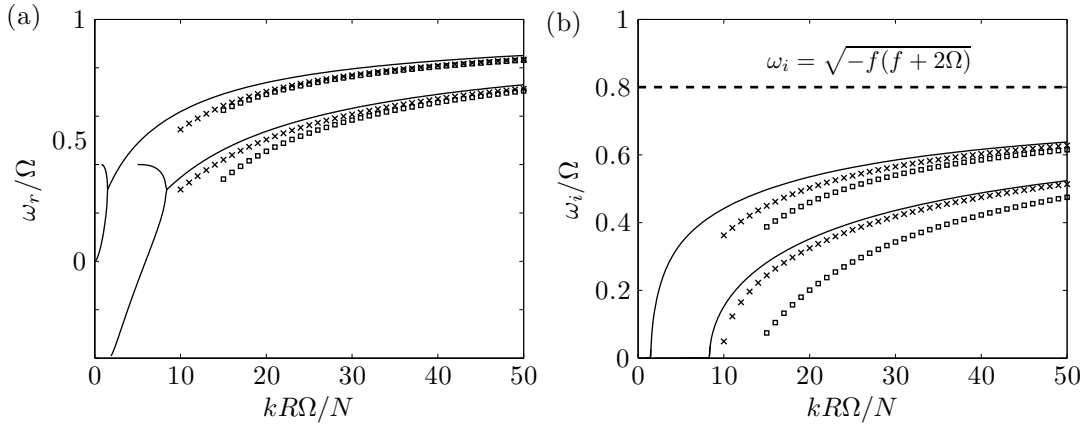

FIG. 14. (a) Frequency and (b) growth rate of the first two branches for $m = 1$ for $f/\Omega = -0.4$. Solid lines are numerical results and symbols are asymptotic results as follows: $\times$: Eq. (29), $\square$: Eq. (43). The thick dashed line in (b) represent the maximum growth rate at $\tilde{k} \to \infty$.

at non-zero $\tilde{k}$ and decreases with $\tilde{k}$ (figure 14a). Hence, these two branches meet at a finite wavenumber and the centrifugal instability appears above this wavenumber (figure 14 b). The same behaviour is observed for the next branches which starts from $\omega_r = |f|$ and $\omega_r = -|f|$: the growth rate becomes positive when they meet. The numerical results for the centrifugal instability are compared to asymptotic results (symbols) obtained from a WKBJ analysis in the complex plane. Indeed, for non-zero azimuthal wavenumber, the growth rate

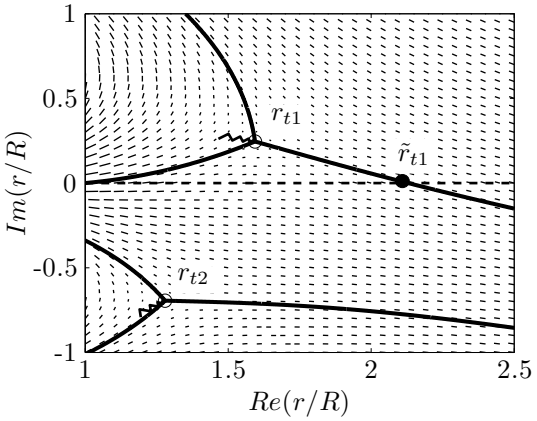

FIG. 15. Examples of the Stokes lines (heavy solid lines) network for $m = 1$ and $kR\Omega/N = 10$ for $f/\Omega = -0.1$ and $\omega/\Omega = 0.412 + 0.140i$. The dashed line and the symbols $\circ$ and $\bullet$ represent the real r-axis, the turning points r_{t1}, r_{t2} and the point $\tilde{r}_{t1}$ where the Stokes line emitted from r_{t1} meets the real r-axis, respectively. The zigzag lines show the branch cut. The short lines indicate the direction of the vectors $(Im(\sqrt{\Delta}), Re(\sqrt{\Delta}))$ which are parallel to the Stokes lines.

and frequency of the centrifugal instability for large $\tilde{k}$ are comparable so that the function $\Delta(r)$ is complex on the real r-axis. Hence, we need to determine the location of the turning points in the complex plane and to consider the Stokes line defined by:

$$Re\left(\int_{r_t}^{r} \sqrt{\Delta(t)}dt\right) = 0. \tag{40}$$

These lines delimit the regions of the complex plane where a given WKBJ approximation is valid[18,23,24].

Figure 15 shows an example of the configuration of turning points and the network of Stokes lines. There are always two turning points but as f decreases from zero, one turning point r_{t2} moves far away from the real axis and no Stokes line emanating from it cross the real axis when $|f|$ is sufficiently large (figure 15a). Therefore, only the turning point r_{t1} which remains close to the real axis needs to be considered. Let $\tilde{r}_{t1}$ denotes the point where the Stokes line emitted from r_{t1} crosses the real axis. In order to construct an eigenmode, we choose the exponentially decaying solution for $r > \tilde{r}_{t1}$

$$p(r) = C\frac{\Delta^{1/4}}{r^{1/2}} \exp\left(-\tilde{k}\int_{r_{t1}}^{r} \sqrt{\Delta}dt\right). \tag{41}$$

The matching solution in the region $R < r < \tilde{r}_{t1}$ is

$$p(r) = Ce^{\frac{i\pi}{4}} \frac{(-\Delta)^{1/4}}{r^{1/2}} \left[\exp\left(i\tilde{k}\int_{r}^{r_{t1}} \sqrt{-\Delta}dt\right) - i\exp\left(-i\tilde{k}\int_{r}^{r_{t1}} \sqrt{-\Delta}dt\right)\right], \tag{42}$$

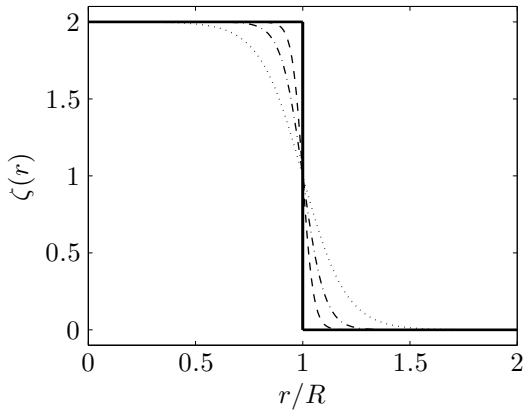

FIG. 16. Axial vorticity of the smoothed Rankine vortex (44) for $\delta = 0$ (solid line), $\delta = 0.05$ (dashed line), $\delta = 0.1$ (dash-dot line) and $\delta = 0.2$ (dotted line).

which is the same as (28). Inserting (42) in the dispersion relation (8) gives the same quantization condition as (29). From (29), we can further express the eigenfrequency in powers of $\tilde{k}$ at leading order

$$\omega = m\Omega + i\sqrt{-f(f+2\Omega)} - \frac{\beta'}{\left(\tilde{k}R\Omega\right)^{2/3}}\ ,\ \beta' = i\frac{\left[\frac{3\Omega^2}{\sqrt{2}}\left(n-\frac{1}{4}\right)\pi\left(-f - im\sqrt{-f(f+2\Omega)}\right)\right]^{2/3}}{\sqrt{-f(f+2\Omega)}}, \tag{43}$$

which is essentially the same as (31). As seen in Fig. 14, these asymptotic results predict well the frequency and growth rate of the centrifugal instability for large $\tilde{k}$. In the particular case of the axisymmetric mode $m = 0$, the solution of (7) for $r > R$ can be found analytically as discussed in the Appendix.

For strong anticyclonic rotation: $f \leq -2\Omega$ (i.e. $-1 \leq Ro < 0$), the Rankine vortex is centrifugally stable but Park and Billant [13] have found that the radiative instability also exists in this regime when the azimuthal wavenumber is larger than 2. The properties of the radiative instability for large m are very similar to those for cyclonic rotation[13].

VI. STABILITY OF THE SMOOTHED RANKINE VORTEX

The Rankine vortex is an idealized solution of the Euler equation with a discontinuity of vorticity. In order to investigate the stability of a vortex with a more realistic profile with continuous vorticity, we have considered the smoothed Rankine vortex proposed by Schecter

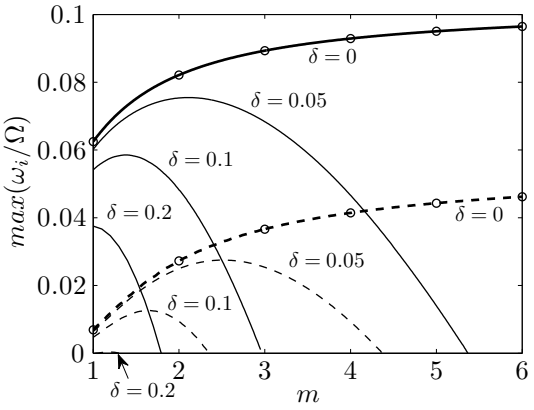

FIG. 17. Maximum growth rate $max(\omega_i)$ of the first branch as a function of the azimuthal wavenumber m for $\delta = [0, 0.05, 0.1, 0.2]$ for $f/\Omega = 0$ (solid lines) and $f/\Omega = 0.2$ (dashed lines). Bold lines represent the limit $\delta = 0$ (i.e. the Rankine vortex).

and Montgomery [8] with axial vorticity

$$\zeta(r) = \Omega \left[1 - \tanh\left(\frac{r/R - 1}{\delta} \right) \right], \tag{44}$$

where δ is a smoothness parameter. This profile tends to the Rankine vortex as $\delta \to 0$ and the vorticity jump becomes smoother as δ increases as illustrated in figure 16. For this continuous profile, we use a classical shooting method to solve the equation (7)[8]. The boundary condition at $r = 0$ is $p(r) \sim r^{|m|}$.

Figure 17 shows the maximum growth rate $max(\omega_i)$ as a function of the azimuthal wavenumber m for different values of smoothness parameter δ. While the maximum growth rate of the Rankine vortex is reached for $m \to \infty$, the maximum growth rate of the smoothed Rankine vortex occurs at finite azimuthal wavenumber m_{max} which decreases as δ increases. This behaviour is due to the presence of a critical point. The stabilizing effect of this critical point is related to the vorticity gradient $|\zeta'(r_c)| \sim 1/\cosh^2(1/m\delta)$[8,13]. Therefore, the damping rate is small when $m\delta << 1$ while it is large for $m\delta >> 1$. This implies that the most amplified azimuthal wavenumber should scale like $m_{max} = O(1/\delta)$ as observed in figure 17. This damping term is independent of f/Ω and thus it reduces the growth rate by approximately the same amount regardless of the values of f/Ω as seen in figure 17.

VII. CONCLUSIONS

We have investigated the effect of the planetary rotation on the instabilities and waves sustained by a columnar vortex in a strongly stratified and rotating fluid. For the Rankine vortex, the radiative instability is stabilized in the presence of cyclonic rotation and its maximum growth rate vanishes below a critical Rossby number which depends on m: $Ro = 2/m$. The maximum growth rate ω_i increases with the azimuthal wavenumber m and is about $\omega_i \sim 0.1\Omega$ for $m >> 1$ for $Ro = \infty$ and exponentially small for $Ro = O(1)$. The instability mechanism can be understood by means of a WKBJ analysis for large rescaled vertical wavenumber k/N. In the presence of cyclonic rotation, the size of the potential barrier around the critical point is increased so that the over-reflection is reduced explaining the stabilization of the radiative instability. In some frequency ranges and below a critical Rossby number, there exist neutral waves. Some of them have a large frequency of order $O(|f|)$ and thereby are not captured by the quasi-geostrophic equation. In the presence of anticyclonic rotation, the vortex is centrifugally unstable in the range $-2 < f/\Omega < 0$. However for slightly negative $f/\Omega \lesssim 0$ (i.e. $Ro \lesssim -400$), the radiative instability is more unstable than the centrifugal instability. Unlike the Rankine vortex, the continuous smoothed Rankine vortex is most unstable at a finite azimuthal wavenumber which depends on the smoothness of the profile.

Appendix: Centrifugal instability of the axisymmetric mode: $m = 0$

For $m = 0$, the solution of (7) can be found analytically outside the vortex core $r > R$ in the form[25]

$$p(r) \sim \left[\frac{1-\nu}{r} K_\nu\left(\tilde{k} r\sqrt{f^2-\omega^2}\right) - \tilde{k}\sqrt{f^2-\omega^2} K_{\nu-1}\left(\tilde{k} r\sqrt{f^2-\omega^2}\right)\right], \qquad \text{(A.1)}$$

where K_ν is the modified Bessel function of the second kind of order ν and $\nu^2 = 1+2fR^2\Omega\tilde{k}^2$. The dispersion relation (8) can be simply expressed as

$$\tilde{k}R\sqrt{(f+2\Omega)^2-\omega^2}\frac{I_0(\tilde{k}R\sqrt{(f+2\Omega)^2-\omega^2})}{I_1(\tilde{k}R\sqrt{(f+2\Omega)^2-\omega^2})} + \tilde{k}R\sqrt{f^2-\omega^2}\frac{K_{\nu-1}(\tilde{k}R\sqrt{f^2-\omega^2})}{K_\nu(\tilde{k}R\sqrt{f^2-\omega^2})} + \nu - 1 = 0. \qquad \text{(A.2)}$$

For cyclonic rotation, the eigenmode which satisfies the outgoing wave boundary condition as $r \to \infty$ increases exponentially with r (see also Billant and Le Dizès[6]). In contrast,

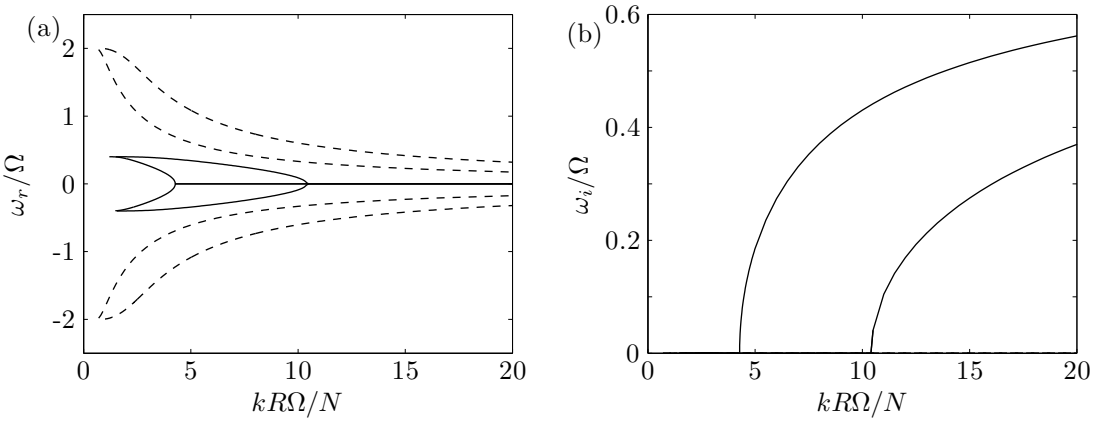

FIG. 18. (a) Frequency and (b) growth rate of the first two branches for $m = 0$ as a function of the rescaled vertical wavenumber $kR\Omega/N$ for $f/\Omega = -0.4$ (solid lines), $f/\Omega = -2$ (dashed lines).

for anticyclonic rotation, there exist eigenmodes which decay as $r \to \infty$. In the range $-2\Omega < f < 0$ (i.e. $Ro < -1$), there is a centrifugal instability as shown in Sec. **V**.

Figure 18 shows the frequency and the growth rate for $f/\Omega = -0.4$ (centrifugally unstable) and $f/\Omega = -2$ (centrifugally stable). We see that there are two frequency branches: one starts from $\omega = f$ at non-zero $\tilde{k}$ and increases with $\tilde{k}$ while the other starts at $\omega = -f$ and decreases with $\tilde{k}$ (figure 18a). For $f/\Omega = -0.4$, these frequency branches meet at a finite $\tilde{k}$ and become unstable for larger $\tilde{k}$ when they meet while for $f/\Omega = -2$, they do not meet and remains neutral whatever $\tilde{k}$ (figure 18b).

REFERENCES

[1]L. Kelvin, "Vibrations of a columnar vortex," Philos. Mag. **10**, 155 (1880).

[2]P. G. Saffman, *Vortex Dynamics* (Cambridge University Press, Cambridge, 1992).

[3]D. Fabre, D. Sipp, and L. Jacquin, "Kelvin waves and the singular modes of the Lamb-Oseen vortex," J. Fluid Mech. **551**, 235–274 (2006).

[4]X. Riedinger, P. Meunier, and S. Le Dizès, "Instability of a vertical columnar vortex in a stratified fluid," Exp. Fluids. **49**, 673–681 (2010).

[5]X. Riedinger, S. Le Dizès, and P. Meunier, "Radiative instability of the flow around a rotating cylinder in a stratified fluid," J. Fluid Mech. **672**, 130–146 (2011).

[6]P. Billant and S. Le Dizès, "Waves on a columnar vortex in a strongly stratified fluid," Phys. Fluids **21**, 106602 (2009).

[7]S. Le Dizès and P. Billant, "Radiative instability in stratified vortices," Phys. Fluids **21**, 096602 (2009).

[8]D. A. Schecter and M. T. Montgomery, "Damping and pumping of a vortex Rossby wave in a monotonic cyclone: Critical layer stirring versus inertia-buoyancy wave emission," Phys. Fluids **26**, 1334 (2004).

[9]D. A. Schecter and M. T. Montgomery, "Conditions That Inhibit the Spontaneous Radiation of Spiral Inertial-Gravity waves from an Intense Mesocale Cyclone," J. Atmos. Sci. **63**, 435 (2006).

[10]D. A. Schecter, "The Spontaneous Imbalance of an Atmospheric Vortex at High Rossby Number," J. Atmos. Sci. **65**, 2498 (2008).

[11]R. Ford, "The instability of an axisymmetric vortex with monotonic potential vorticity in rotating shallow water," J. Fluid Mech. **280**, 303–334 (1994).

[12]E. Broadbent and D. W. Moore, "Acoustic destabilization of vortices," Philos. Trans. R. Soc. London, Ser. A **290**, 353 (1979).

[13]J. Park and P. Billant, "Radiative instability of an anticyclonic vortex in a stratified rotating fluid," J. Fluid Mech. **707**, 381–392 (2012).

[14]W. D. Smyth and J. C. McWilliams, "Instability of an Axisymmetric Vortex in a Stably Stratified, Rotating Environment," Theoret. Comput. Fluid Dynamics **11**, 305–322 (1998).

[15]T. Miyazaki and H. Hanazaki, "Baroclinic instabliity of Kirchhoff's elliptic vortex," J. Fluid Mech. **261**, 273–303 (1994).

[16]S. Le Dizès and X. Riedinger, "The strato-rotational instability of Taylor-Couette and Keplerian flows," J. Fluid Mech. **660**, 147–161 (2010).

[17]S. Le Dizès and L. Lacaze, "An asymptotic description of vortex Kelvin modes," J. Fluid Mech. **542**, 69–96 (2005).

[18]C. M. Bender and S. A. Orszag, *Advanced Mathematical Methods for Scientists and Engineers* (McGraw-Hill, New York, 1978).

[19]M. Abramowitz and I. A. Stegun, *Handbook of Mathematical Functions* (Dover, New York, 1965).

[20]L. Parras and S. Le Dizès, "Temporal instability modes of supersonic round jets," J. Fluid Mech. **662**, 173–196 (2010).

[21]Lord Rayleigh, "On the Dynamics of Revolving Fluids," Proc. Roy. Soc. London, *A* **94**, 148–154 (1917).

[22]R. C. Kloosterziel and G. J. F. van Heijst, "An experimental study of unstable barotropic vortices in a rotating fluid," J. Fluid Mech. **223**, 1–24 (1991).

[23]F. W. J. Olver, *Asymptotics and Special Functions* (Academic, 1974).

[24]P. Billant and F. Gallaire, "Generalized Rayleigh criterion for non-axisymmetric centrifugal instabilities," J. Fluid Mech. **542**, 365–379 (2005).

[25]A. Lazar, A. Stegner, and E. Heifetz, "Inertial instability of intense stratified anticyclones. Part I: Generalized stability criterion," submitted to J. Fluid Mech. (2012).

2 Stability of the cyclonic Lamb-Oseen vortex

In this section, we consider the Lamb-Oseen vortex as a base flow. The Lamb-Oseen vortex is an exact solution of the Navier-Stokes equations (Saffman, 1992). Due to the viscosity, the vortex diffuses and the radius of the vortex core R increases in time. But in this thesis, we neglect the viscous effects on the base flow so that the radius of the vortex core R does not change. Using R and $2\pi R^2/\Gamma$ as characteristic length and time scales where Γ is the circulation, this frozen Lamb-Oseen vortex has a non-dimensional azimuthal velocity profile

$$U_\theta(r) = \frac{1 - e^{-r^2}}{r}. \tag{3.1}$$

The Lamb-Oseen vortex is continuous everywhere and we apply the boundary conditions such that the perturbations are non-singular at the vortex center $r = 0$ and they vanish or propagate outward as $r \to \infty$.

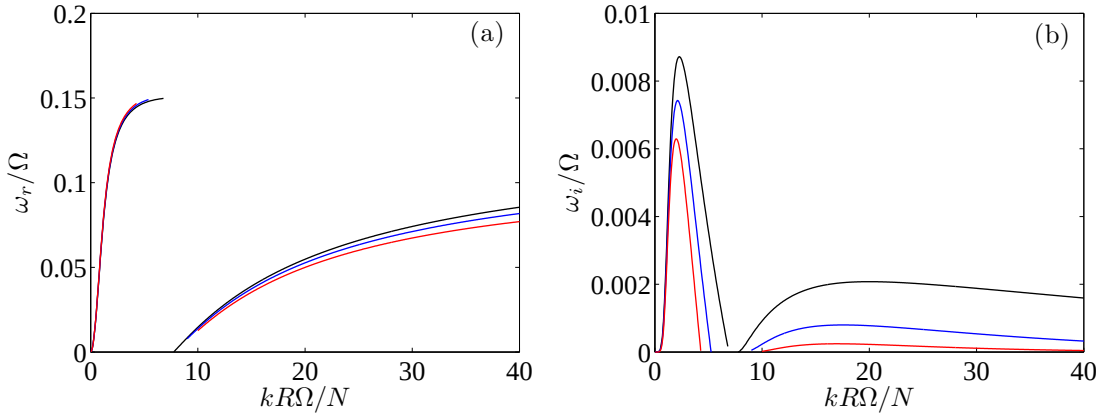

Figure 3.1: (a) Frequency and (b) growth rate of the Lamb-Oseen vortex for $m = 1$ for $f/\Omega = 0$ (black), $f/\Omega = 0.004$ (blue) and $f/\Omega = 0.008$ (red).

Figure 3.1 shows the frequency and the growth rate of the Lamb-Oseen vortex for $m = 1$ for $f/\Omega = [0, 0.004, 0.008]$. As found by Le Dizès & Billant (2009), the Lamb-Oseen vortex is unstable to the radiative instability in a stratified fluid while it is stable in homogeneous fluids (Fabre *et al.*, 2006). Without background rotation (i.e. $f/\Omega = 0$), the frequency of the first branch starts from $\omega_r = 0$ at $k = 0$ and increases with $\tilde{k}$ up to $\omega_r \approx 0.15\Omega$ for $\tilde{k} \approx 8$. The second branch starts at $\tilde{k} \approx 8$ and its frequency increases with $\tilde{k}$. The maximum growth rate is obtained for the first branch as $\omega_i \approx 0.009\Omega$ around $\tilde{k} \approx 2$. In presence of background rotation, we clearly see that the growth rate decreases as f increases (figure 3.1b). Like for the Rankine vortex, the growth rate of the second branch decreases more rapidly as f increases than that of the first branch.

Figure 3.2 shows the maximum growth rate of the first two branch as a function of the inverse of the Rossby number. The maximum growth rate decreases exponentially as f increases. Compared to the Rankine vortex, the Lamb-Oseen vortex is stabilized more rapidly as the Rossby number Ro decreases (i.e. the Coriolis parameter f increases).

We can understand this by looking at the epicyclic frequencies and the critical frequency. Figure 3.3 shows the epicyclic frequencies and the critical frequency for $m = 1$ for $f/\Omega = [0, 0.004, 1]$. They resemble the epicyclic frequencies of the Rankine vortex so that the structure

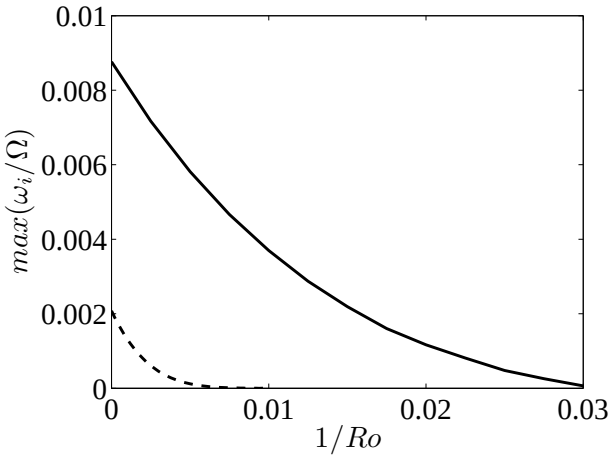

Figure 3.2: Maximum growth rate of the first branch (solid line) and the second branch (dashed line) of the Lamb-Oseen vortex as a function of the inverse of the Rossby number for $m = 1$.

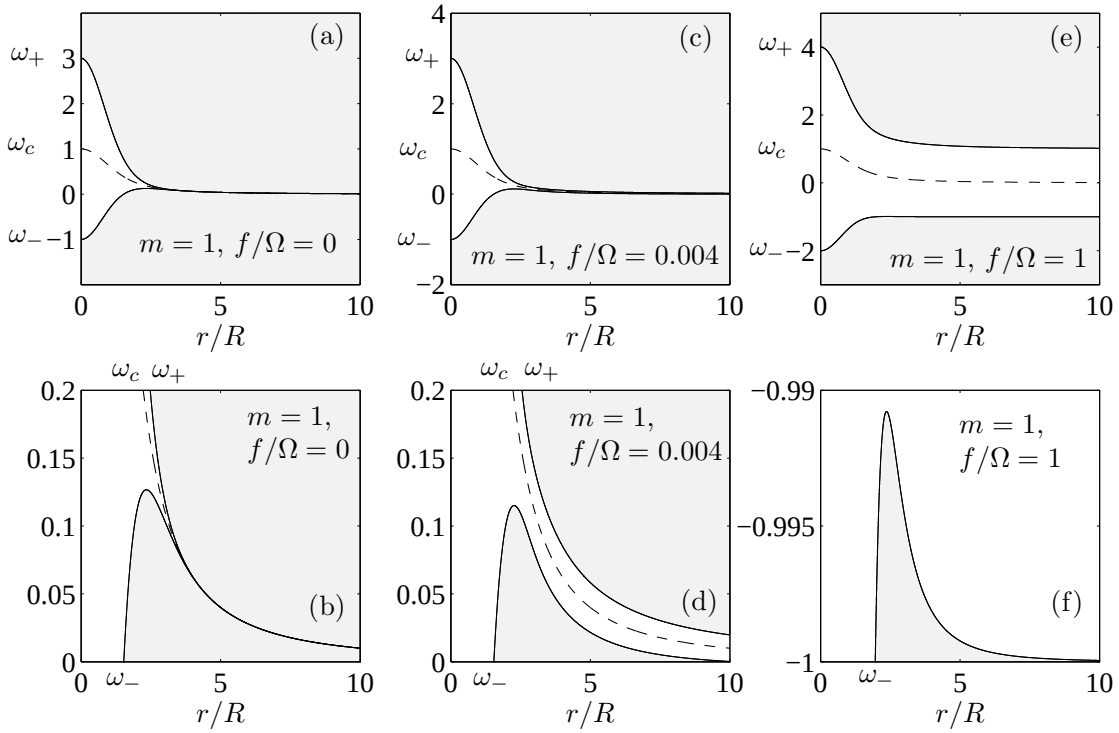

Figure 3.3: Epicyclic frequencies $\omega_\pm$ and critical frequency ω_c for different Coriolis parameters for $m = 1$. (b), (d), (f) zoom in the region of bounded waves of (a), (c), (e), respectively.

of the eigenmodes is very similar as well. In contrast to the Rankine vortex, there exists a finite size potential barrier even when there is no rotation (i.e. $f/\Omega = 0$) and there is a singularity at the critical point r_c (figure 3.3a,b). As we have seen for the Rankine vortex, the stabilizing effect of the potential barrier increases with its size. The singularity at the critical point r_c has also a stabilizing effect which is proportional to the gradient of the vorticity $|Z_c'|$ at the critical point (Schecter *et al.*, 2000, 2002). The critical point has a stabilizing effect for the Lamb-Oseen vortex since $Z_c' < 0$ while it has no effect for the Rankine vortex since $Z_c' = 0$. The radiative instability for the Lamb-Oseen vortex is weaker than for the Rankine vortex because of these two stabilizing effects (Schecter & Montgomery, 2004, 2006; Schecter, 2008).

As f increases, the epicyclic frequency ω_+ increases while ω_- decreases (figure 3.3c,d). Therefore, the potential barrier widens like for the Rankine vortex leading to the stabilization of the radiative instability. When f is sufficiently large such that $min(\omega_+) = f > max(\omega_-)$, the potential barrier extends towards infinity and the solutions become evanescent everywhere (figure 3.3e,f). The evanescent solutions can not satisfy the boundary conditions except when there is a critical point r_c. Here, we present a critical point analysis which matches the WKBJ approximations and the Frobenius series around r_c.

We recall the WKBJ approximation for the pressure

$$p(r) \sim \frac{\Delta^{1/4}}{r^{1/2}} \left[A \exp\left\{ \tilde{k} \int_{r_c}^{r} \sqrt{\Delta(t)} dt \right\} + B \exp\left\{ -\tilde{k} \int_{r_c}^{r} \sqrt{\Delta(t)} dt \right\} \right], \tag{3.2}$$

for $r > r_c$. In the presence of a critical point, this WKBJ approximation breaks down since some terms of order $O(1)$ in the equation (2.24) are no longer negligible around the critical point r_c. Around r_c, we approximate $s \sim s'(r_c)\epsilon\tilde{r}$ where $\tilde{r} = (r - r_c)/\epsilon$ and $\epsilon = 1/\left(\tilde{k}\sqrt{\Delta(r_c)}\right)$. Then, the equation (2.24) simplifies to

$$\frac{d^2 p}{d\tilde{r}^2} - \left(1 + \frac{\delta}{\tilde{r}}\right) p = O(\epsilon), \tag{3.3}$$

where $\delta = \frac{Z_c'(f+2\Omega_c)}{r_c \Omega_c'(f+Z_c)}\epsilon$. Although δ is a priori of order ϵ, we do not neglect the term $O(\delta)$ in (3.3) since it determines the logarithmic behaviour of $p(\tilde{r})$ around the critical point r_c. For $\tilde{r} \to \infty$, the pressure $p(\tilde{r})$ has an asymptotic solution $p(\tilde{r}) \sim A_1 \exp(\tilde{r}) + B_1 \exp(-\tilde{r})$ which matches the WKBJ approximation (3.2) with $A_1 = A\Delta_c^{1/4}/r_c^{1/2}$ and $B_1 = B\Delta_c^{1/4}/r_c^{1/2}$. Then, we solve the equation (3.3) for $|\tilde{r}| << 1$ using the Frobenius series $p(\tilde{r}) = \sum_{n=0}^{\infty} a_n \tilde{r}^{n+x_1}$. The two solutions of (3.3) are

$$p_1(\tilde{r}) = \tilde{r}\left[1 + \sum_{n=1}^{\infty} a_n \tilde{r}^n\right], \quad p_2(\tilde{r}) = -\delta p_1(\tilde{r}) \log(\tilde{r}) - \sum_{n=0}^{\infty} b_n \tilde{r}^n \tag{3.4}$$

where $a_1 = \delta/2$, $a_2 = 1/6 + \delta^2/12, \ldots$, $b_0 = 1$, $b_1 = a_1, \ldots$ and C_1, C_2 are constants. We clearly see that there is a logarithmic singularity when $\delta \neq 0$. By deforming the integration path above the critical point since $\Omega_c' < 0$, we have for $\tilde{r} < 0$: $\log(\tilde{r}) = \log(|-\tilde{r}|) + i\pi$ (see figure 3.4a and Schecter *et al.*, 2002; Le Dizès, 2004; Billant, 2010). The WKBJ approximation for $r < r_c$ is therefore

$$p(r) \sim \frac{\Delta^{1/4}}{r^{1/2}} \left[C \exp\left\{ \tilde{k} \int_{r}^{r_c} \sqrt{\Delta(t)} dt \right\} + D \exp\left\{ -\tilde{k} \int_{r}^{r_c} \sqrt{\Delta(t)} dt \right\} \right]. \tag{3.5}$$

where

$$C = \left(-\frac{i\pi}{2}\delta\right) A + \left(1 - \frac{i\pi}{2}\delta\right) B \ , \ D = \left(1 + \frac{i\pi}{2}\delta\right) A + \left(\frac{i\pi}{2}\delta\right) B. \tag{3.6}$$

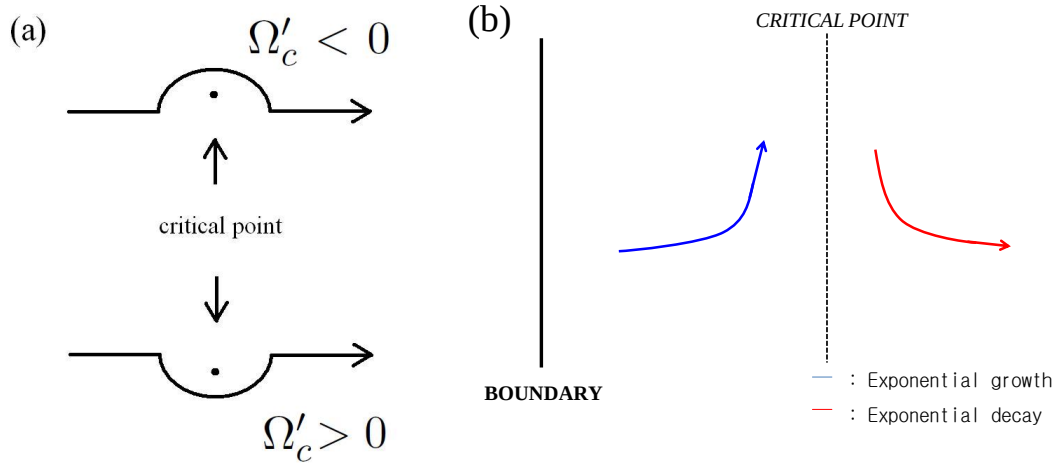

Figure 3.4: (a) Contour deformation around the critical point depending on the sign of $\Omega'(r_c)$ for the numerical integration. (b) Logarithmic behaviour around the critical point r_c.

In the absence of critical point (i.e. $\delta = 0$), $A = D$ and $B = C$ so that no combination of the constants satisfies the boundary conditions. On the other hand, when there is a critical point (i.e. $\delta \neq 0$), we can satisfy the boundary conditions by putting $A = 0$ and $C = 0$ (i.e. exponentially decaying for $r > r_c$ and increasing for $r < r_c$: see figure 3.4b). This implies $1 - i\pi\delta/2 = 0$, showing that δ should be of order unity. The dispersion relation is therefore

$$\tilde{k}\sqrt{\Delta(r_c)} = i\pi \frac{Z'_c(f + 2\Omega_c)}{2r_c\Omega'_c(f + Z_c)}. \tag{3.7}$$

Figure 3.5 shows the frequency and the growth rate of the first branch for $m = 1$ for $f/\Omega = [1, 2]$. The growth rate is strongly negative due to the singularity at r_c and decreases as $\tilde{k}$ increases. We see that the asymptotic dispersion relation (3.7) is in good agreement with the numerical results when $\tilde{k}$ is sufficiently large.

Although the first branch is stable for large f due to the critical point, the next branches for $m = 1$ become neutral with a ring structure: a wave region trapped between two evanescent regions (figure 3.3f). The whole branches are neutral when there is no critical point: $max(\omega_-) < min(\omega_c) = 0$ corresponding to $f \gtrsim 0.0721\Omega$. We can obtain the asymptotic dispersion relation for these modes

$$\tilde{k} \int_{r_{t1}}^{r_{t2}} \sqrt{-\Delta} dt = \frac{1}{2}(n + 1)\pi, \tag{3.8}$$

where r_{t1}, r_{t2} are turning points and n is the branch number. From the equation (3.8), we see that as $\tilde{k} \to \infty$, the two turning points should be close and Δ should tend to zero at leading order in $\tilde{k}$ which implies that the frequency ω_r tends to $\omega_r = max(\omega_-)$ as $\tilde{k} \to \infty$.

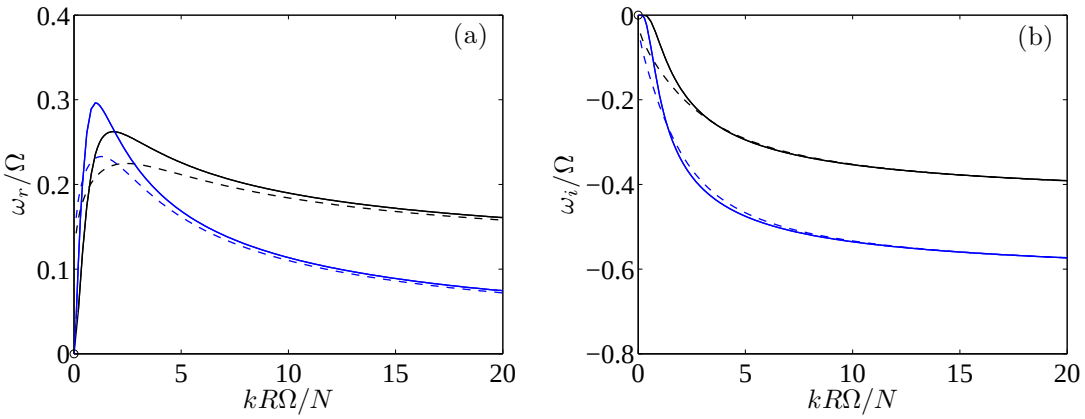

Figure 3.5: (a) Frequency and (b) growth rate of the first branch of the Lamb-Oseen vortex for $m = 1$ for $f/\Omega = 1$ (black) and $f/\Omega = 2$ (blue). Solid lines are numerical results and dashed lines are asymptotic results from (3.1), respectively.

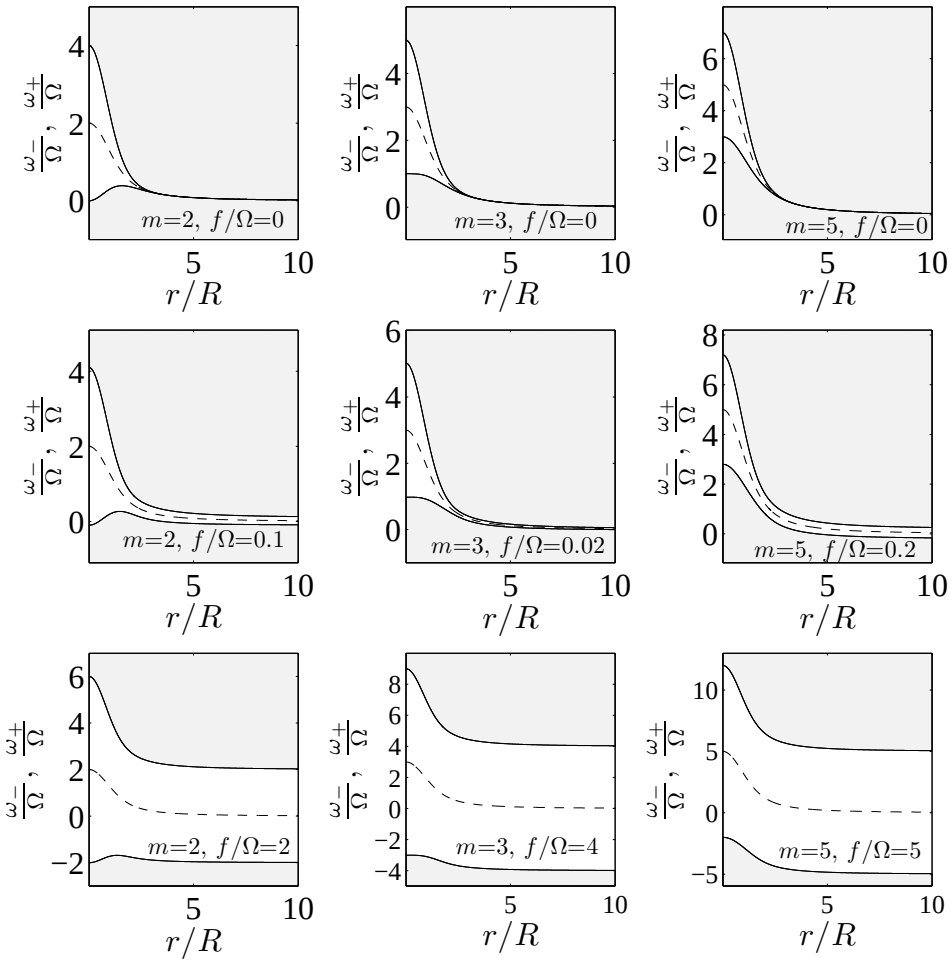

Figure 3.6: Epicyclic frequencies $\omega_\pm$ and critical frequency ω_c for the azimuthal wavenumbers $m = [2, 3, 5]$.

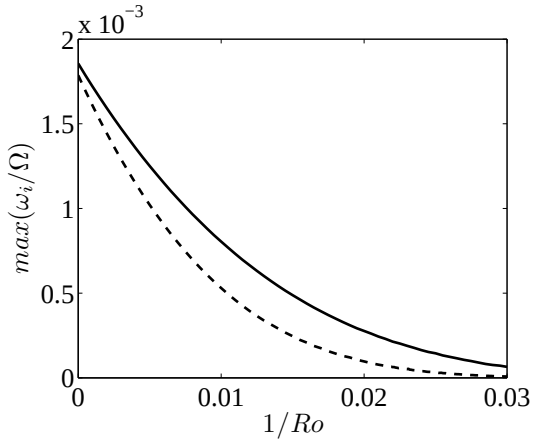

Figure 3.7: Maximum growth rate of the first ring mode (solid line) and the second ring mode (dashed line) of the Lamb-Oseen vortex as a function of the inverse of the Rossby number for $m = 2$.

Figure 3.6 shows examples of the epicyclic frequencies $\omega_{\pm}$ and the critical frequency ω_c for higher azimuthal wavenumbers $m = [2, 3, 5]$ for different Coriolis parameters. We see that the epicyclic frequencies and the critical frequency are similar to those for $m = 1$ so that we expect that the stabilization as f increases also holds for $m > 1$. For example, figure 3.7 shows the maximum growth rate for $m = 2$ as a function of the inverse of Rossby number $1/Ro$. For $m = 2$, neutral ring modes also exist like for $m = 1$ but for $m \geq 3$, the waves are now trapped between the turning points and the vortex center $r = 0$. They correspond therefore to core modes and their asymptotic dispersion relation is

$$\tilde{k} \int_0^{r_t} \sqrt{-\Delta} dt = \frac{1}{2}(m + n + 1)\pi. \tag{3.9}$$

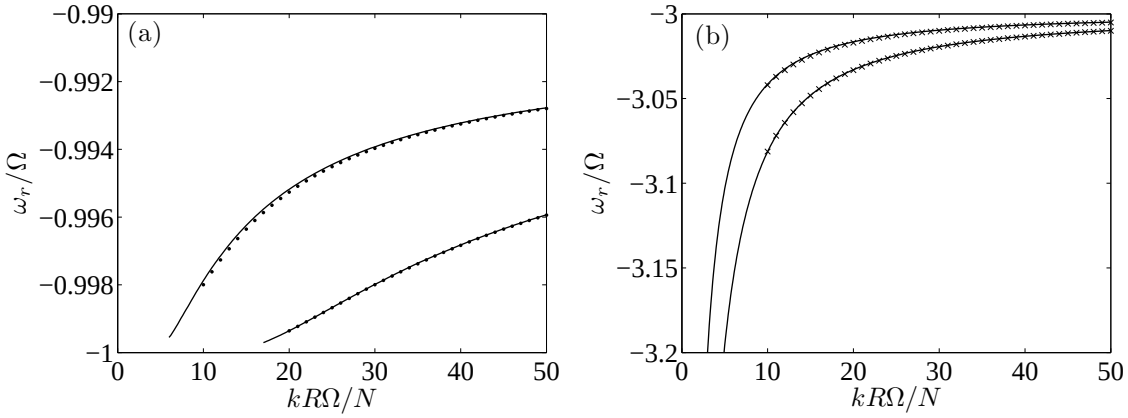

Figure 3.8: Frequency of the first two trapped modes of the Lamb-Oseen vortex for (a) $m = 1$, $f/\Omega = 1$ (ring mode) and (b) $m = 3$, $f/\Omega = 4$ (core mode). Solid lines are numerical results and symbols are asymptotic results: ·, (3.6); ×, (3.7).

Figure 3.8 shows the frequency of the neutral trapped modes for the next branches for $(m, f/\Omega) = (1, 1)$ and $(m, f/\Omega) = (3, 4)$ which correspond to a ring mode and a core mode,

respectively. The agreement between the numerical results and the asymptotic dispersion relations is good for large $\tilde{k}$. We found that the frequency of the next branches of the Lamb-Oseen vortex start from $\omega_r = min(\omega_-) = f$ and tends to $\omega_r = max(\omega_-)$ as $k \to \infty$ like for the Rankine vortex.

Chapter 4

Effect of strong anticyclonic rotation with $-1 < Ro < 0$

1 Radiative instability of an anticyclonic vortex in a stratified rotating fluid

Article published in Journal of Fluid Mechanics.

J. Fluid Mech. (2012), *vol.* 707, *pp.* 381–392.
doi:10.1017/jfm.2012.286

Radiative instability of an anticyclonic vortex in a stratified rotating fluid

Junho Park† and Paul Billant

LadHyX, CNRS, École Polytechnique, F-91128 Palaiseau CEDEX, France

(Received 28 February 2012; revised 30 April 2012; accepted 11 June 2012;
first published online 27 July 2012)

In strongly stratified fluids, an axisymmetric vertical columnar vortex is unstable because of a spontaneous radiation of internal waves. The growth rate of this radiative instability is strongly reduced in the presence of a cyclonic background rotation $f/2$ and is smaller than the growth rate of the centrifugal instability for anticyclonic rotation, so it is generally expected to affect vortices in geophysical flows only if the Rossby number $Ro = 2\Omega/f$ is large (where Ω is the angular velocity of the vortex). However, we show here that an anticyclonic Rankine vortex with low Rossby number in the range $-1 \leqslant Ro < 0$, which is centrifugally stable, is unstable to the radiative instability when the azimuthal wavenumber $|m|$ is larger than 2. Its growth rate for $Ro = -1$ is comparable to the values reported in non-rotating stratified fluids. In the case of continuous vortex profiles, this new radiative instability is shown to occur if the potential vorticity of the base flow has a sufficiently steep radial profile. The most unstable azimuthal wavenumber is inversely proportional to the steepness of the vorticity jump. The properties and mechanism of the instability are explained by asymptotic analyses for large wavenumbers.

Key words: rotating flows, stratified flows, vortex instability

1. Introduction

When a vortex evolves in a fluid that can support waves, it can be unstable and spontaneously emit waves. Such radiative instability has been shown to occur in compressible fluids with the emission of acoustic waves (Broadbent & Moore 1979), as well as shallow-water or rotating stratified fluids with the radiation of inertia–gravity waves (Ford 1994; Schecter & Montgomery 2004, 2006; Schecter 2008; Billant & Le Dizès 2009; Le Dizès & Billant 2009). The instability comes from the coupling between the vortical waves sustained by the vortex and an outer wave field. Radiative instability has recently been thoroughly investigated in the case of a non-rotating stratified fluid. By means of a WKBJ analysis, Billant & Le Dizès (2009) and Le Dizès & Billant (2009) have shown that the instability can be understood as an over-reflection process. Riedinger, Le Dizès & Meunier (2010) have investigated the effect of Reynolds and Froude numbers on the radiative instability of a Lamb–Oseen vortex. Riedinger, Le Dizès & Meunier (2011) have also provided clear experimental evidence for the radiative instability in the case of flow around a rotating vertical cylinder in a stratified fluid.

The effect of planetary rotation has been analysed in the case of a cyclonic rotation (Schecter & Montgomery 2004, 2006; Le Dizès & Riedinger 2010). The growth

† Email address for correspondence: junho.park@ladhyx.polytechnique.fr

rate of the radiative instability decreases with the Rossby number and becomes exponentially small in the quasi-geostrophic limit (Vanneste & Yavneh 2004, 2007). In the presence of anticyclonic rotation, the centrifugal instability, which is stronger, occurs when $Ro < -1$. Hence, it is generally concluded that the radiative instability will not affect real vortices in the oceans and atmosphere if the Rossby number is smaller than unity (Schecter & Montgomery 2004; Le Dizès & Riedinger 2010). However, we show in this paper that the radiative instability can occur on a columnar anticyclonic vortex with a non-negligible growth rate when $-1 < Ro < 0$, i.e. in the centrifugally stable regime. Interestingly, this range of Rossby numbers corresponds to many large-scale vortices observed in the oceans such as, for example, the 'Meddies' (Ménesguen *et al.* 2009).

The paper is organized as follows. The problem is formulated in § 2. In § 3, we explain why radiative instability can be expected to occur in the range $-1 \leqslant Ro < 0$ above a critical azimuthal wavenumber. In §§ 4 and 5, the stability of the Rankine vortex and the smoothed Rankine vortex are investigated.

2. Problem formulation

We consider an axisymmetric vortex with velocity components $(0, U_\theta(r), 0)$ in a cylindrical coordinate system (r, θ, z) which is rotating about the vertical axis at angular velocity $\Omega_b = f/2$, where f is the Coriolis parameter. The fluid is assumed to be inviscid and stably stratified with a constant Brunt–Väisälä frequency N. We subject this vortex to infinitesimally small three-dimensional perturbations of velocity $\tilde{\boldsymbol{u}} = (\tilde{u}_r, \tilde{u}_\theta, \tilde{u}_z)$, pressure $\tilde{p}$ and density $\tilde{\rho}$, written in the form $(\tilde{\boldsymbol{u}}, \tilde{p}, \tilde{\rho}) = (\boldsymbol{u}(r), p(r), \rho(r))\mathrm{e}^{-\mathrm{i}\omega t + \mathrm{i}kz + \mathrm{i}m\theta} + \text{c.c.}$, where ω is the complex frequency, m the azimuthal wavenumber and k the vertical wavenumber. Under the Boussinesq approximation, the linearized equations of momentum, density conservation and continuity for the perturbations can be reduced to a single equation for the pressure perturbation p:

$$\frac{\mathrm{d}^2 p}{\mathrm{d}r^2} + \left(\frac{1}{r} - \frac{\Delta'}{\Delta}\right)\frac{\mathrm{d}p}{\mathrm{d}r} + \left[-\frac{k^2}{N^2 - s^2}\Delta - \frac{m^2}{r^2} + \frac{m\Delta}{rs}\left(\frac{f + 2U_\theta/r}{\Delta}\right)'\right] p(r) = 0, \quad (2.1)$$

where $\Delta(r) = (f + \zeta)(f + (2U_\theta/r)) - s^2$, $\zeta = (1/r)(\mathrm{d}/\mathrm{d}r)(rU_\theta)$ is the axial vorticity of the vortex, $s = -\omega + mU_\theta/r$ is the Doppler-shifted frequency, and the prime denotes differentiation with respect to r (Smyth & McWilliams 1998). Due to the symmetry $\omega(k, m) = \omega(-k, m) = -\omega^*(-k, -m)$, we consider hereafter only positive k and m. Moreover, we assume that the fluid is strongly stratified, so the hydrostatic approximation can be applied: $N \gg |s|$ (i.e. $N^2 - s^2 \approx N^2$). This implies that (2.1) depends on k and N only through the rescaled vertical wavenumber $\tilde{k} = k/N$ owing to the self-similarity of strongly stratified fluids (Billant & Chomaz 2001). This assumption also implies that there is no singularity where $|s| = N$.

In the following, we first consider as the basic state the Rankine vortex, $U_\theta(r) = \Omega r$ for $r < R$ and $U_\theta(r) = \Omega R^2/r$ for $r > R$, where Ω is constant and R is the radius of the vortex core. A continuous smoothed Rankine vortex will be considered next in § 5. The boundary conditions are that the perturbations are non-singular at the vortex centre $r = 0$ and decay exponentially or radiate energy outward as $r \to \infty$. In the case of the Rankine vortex, we also apply the kinematic and the dynamic conditions at the boundary of the vortex core $r = R$: $u_{r_{in}}(R) = u_{r_{out}}(R)$ and $p_{in}(R) = p_{out}(R)$, respectively. The subscripts '*in*' and '*out*' denote the solution for $r < R$ and $r > R$, respectively. By using the relation $u_r \sim -\mathrm{i}\{sp' + (m/r)(f + (2U_\theta/r))p\}/\Delta$ derived from the horizontal

momentum equations, these boundary conditions give the dispersion relation in terms of p:

$$\frac{p'_{out}(R)}{p_{out}(R)} = \frac{\Delta_{out}(R)}{\Delta_{in}(R)}\frac{p'_{in}(R)}{p_{in}(R)} - \frac{m(f+2\Omega)}{Rs(R)}\left[1 - \frac{\Delta_{out}(R)}{\Delta_{in}(R)}\right]. \tag{2.2}$$

Note that $\Delta_{in}(R) \neq \Delta_{out}(R)$, since there is a discontinuity of the axial vorticity $\zeta(r)$ for the Rankine vortex. The non-singular solution of (2.1) inside the vortex core ($r < R$) is

$$p_{in}(r) \sim \mathrm{J}_m(\tilde{k}r\sqrt{(-\omega + m\Omega)^2 - (f+2\Omega)^2}), \tag{2.3}$$

where J_m is the Bessel function of the first kind of order m. When ω is real, the function J_m has a wave behaviour when $|-\omega + m\Omega| > |f + 2\Omega|$ and increases exponentially when $|-\omega+m\Omega| < |f+2\Omega|$. Outside the vortex core ($r > R$), (2.1) needs to be integrated numerically. The integration is performed inward, starting far outside the vortex core $r \gg R$ from the asymptotic solution, which satisfies the boundary condition for $r \to \infty$,

$$p_{out}(r) \sim \mathrm{H}_m^{(1)}(\tilde{k}r\sqrt{\omega^2 - f^2}), \tag{2.4}$$

where $\mathrm{H}_m^{(1)}$ is the Hankel function of the first kind of order m. For real ω, $\mathrm{H}_m^{(1)}$ behaves like an outgoing wave when $|\omega| > |f|$ and decreases exponentially with r when $|\omega| < |f|$. Starting from an initial estimate for ω, the secant method is used to find the value of ω which satisfies the dispersion relation (2.2).

3. Preliminary discussion

In the present paper, we shall consider anticyclonic background rotation in the range $-1 \leqslant Ro < 0$, where $Ro = 2\Omega/f$ is the Rossby number. In this range, the Rankine vortex is stable with respect to the centrifugal instability since the Rayleigh discriminant $\phi = (f + \zeta)(f + 2U_\theta/r)$ is positive for all radii (Kloosterziel & van Heijst 1991). However, we shall show that radiative instability can occur. Its existence can be anticipated thanks to a WKBJ analysis for large rescaled axial wavenumber $\tilde{k} = k/N$ following Le Dizès & Lacaze (2005), Billant & Le Dizès (2009) and Le Dizès & Billant (2009). For large $\tilde{k}$, the WKBJ approximation of the solution of (2.1) is

$$p(r) = A\frac{(-\Delta)^{1/4}}{r^{1/2}}\mathrm{e}^{\mathrm{i}\tilde{k}\int_{r_t}^{r}\sqrt{-\Delta(t)}\,\mathrm{d}t} + B\frac{(-\Delta)^{1/4}}{r^{1/2}}\mathrm{e}^{-\mathrm{i}\tilde{k}\int_{r_t}^{r}\sqrt{-\Delta(t)}\,\mathrm{d}t}, \tag{3.1}$$

where (A, B) are constants (Bender & Orszag 1978). This approximation is valid everywhere except in the neighbourhood of the so-called turning point r_t, where $\Delta(r_t) = 0$. From (3.1), we see that the WKBJ approximation is wavelike if $\Delta < 0$ while it is exponentially decreasing or growing if $\Delta > 0$. The sign of Δ can be easily determined by plotting the epicyclic frequencies $\omega_\pm(r) = mU_\theta/r \pm \sqrt{(f+\zeta)(f+2U_\theta/r)}$ (Le Dizès & Lacaze 2005). When the frequency ω lies in the interval $\omega_- < \omega < \omega_+$, Δ is positive; otherwise Δ is negative. Le Dizès & Billant (2009) have shown that a condition for the existence of radiative instability is the presence of two intervals where Δ is negative, i.e. where the WKBJ approximation is wavelike, one of which extends towards infinity. These two regions should be separated by a third region, where Δ is positive and which contains a critical radius r_c where $s(r_c) = 0$, i.e. where the azimuthal phase velocity ω_c/m is equal to the angular velocity $U_\theta(r_c)/r_c$. When these conditions are fulfilled, the group velocity reverses

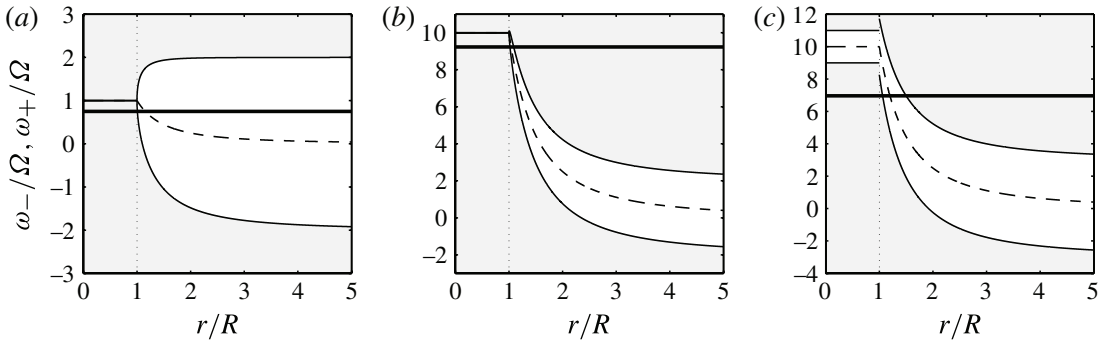

FIGURE 1. Epicyclic frequencies ω_- and ω_+ (solid lines) and critical frequency ω_c (dashed lines) as a function of r for (*a*) $(m, Ro) = (1, -1)$, (*b*) $(m, Ro) = (10, -1)$, and (*c*) $(m, Ro) = (10, -2/3)$. The regions where the WKBJ approximations are wavelike (i.e. $\Delta < 0$) are shaded. Dotted lines represent the boundary of the vortex core. Thick solid lines show examples of the frequency ω_r.

at r_c, so an incident wave propagating from the inner region where $\Delta < 0$ toward the outer one is over-reflected at the critical radius, leading to unstable eigenmodes.

Figure 1 shows the frequencies $\omega_\pm$ and ω_c for different examples of m and Ro. The regions where Δ is negative are shaded. For $m = 1$ and $Ro = -1$ (figure 1*a*), we see that there is never co-existence of two regions where $\Delta < 0$ for a given frequency ω. This remains the case for any Rossby number in the range $[-1, 0]$, so radiative instability is not expected to exist for $m = 1$. In contrast, for $m = 10$ and $Ro = -1$ (figure 1*b*) and $Ro = -2/3$ (figure 1*c*), there exist two wave regions ($\Delta < 0$) separated by a region where $\Delta > 0$ and which contains the critical frequency ω_c (dashed lines) for the examples of frequency indicated by a bold line. For arbitrary m and Ro, it is easy to deduce that such a radiative configuration can exist only if $\omega_+(\infty) < \omega < \max(\omega_-)$, because ω_- always decreases monotonically with r for the Rankine vortex. The first inequality $\omega_+(\infty) < \omega$ ensures that there exists a radiating wave at infinity whereas the second inequality $\omega < \max(\omega_-)$ implies that there are at least two wave regions. Using the expressions of the epicyclic frequencies $\omega_\pm$ for the Rankine vortex, this gives

$$-\frac{2}{Ro} < \frac{\omega}{\Omega} < m + \frac{2}{Ro} + 2. \tag{3.2}$$

Hence, a condition for the existence of radiative instability is $\omega_+(\infty) < \max(\omega_-)$, i.e. $Ro < -4/(m + 2)$. Therefore, radiative instability should exist for large axial wavenumber in the range $-1 \leqslant Ro < 0$ only if $m > 2$. We shall now integrate (2.1) numerically in order to check these predictions. The detailed derivation of the complete WKBJ approximations in the different regions is postponed to the Appendix.

4. Stability of the Rankine vortex

4.1. *Numerical results for* $Ro = -1$

In figure 2, we show the frequency and growth rate for $m = 1$ and $m = 10$ at $Ro = -1$. These two azimuthal wavenumbers are typical of the two different behaviours that can be encountered when m is varied. As anticipated in § 3, the azimuthal wavenumber $m = 1$ is neutral, whereas for $m = 10$ the growth rate is positive (figure 2*b*). For both azimuthal wavenumbers, there is an infinite number of branches which differ by the number of zeros of the eigenfunction inside the vortex core. The first branch

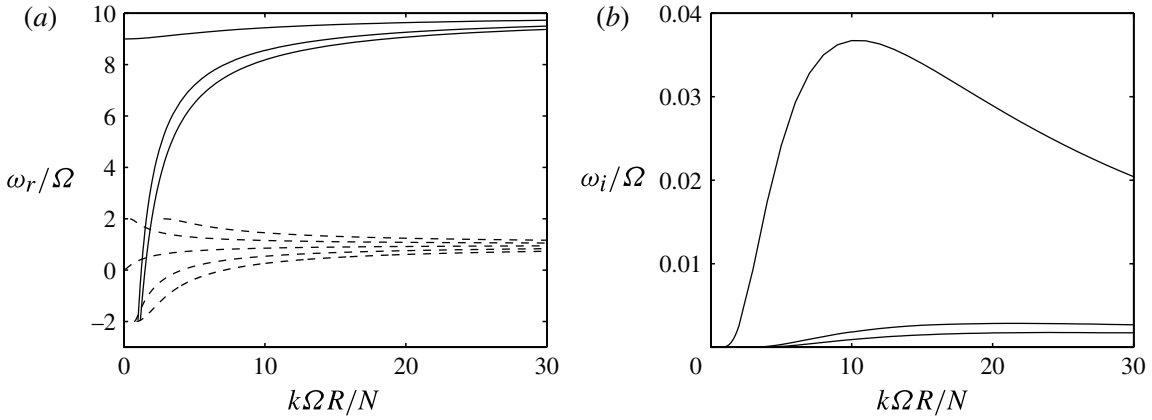

FIGURE 2. (*a*) Frequency ω_r and (*b*) growth rate ω_i as a function of the rescaled vertical wavenumber $k\Omega R/N$ at $Ro = -1$. Dashed lines and solid lines are numerical results for $m = 1$ and $m = 10$, respectively. Only the first three branches are shown.

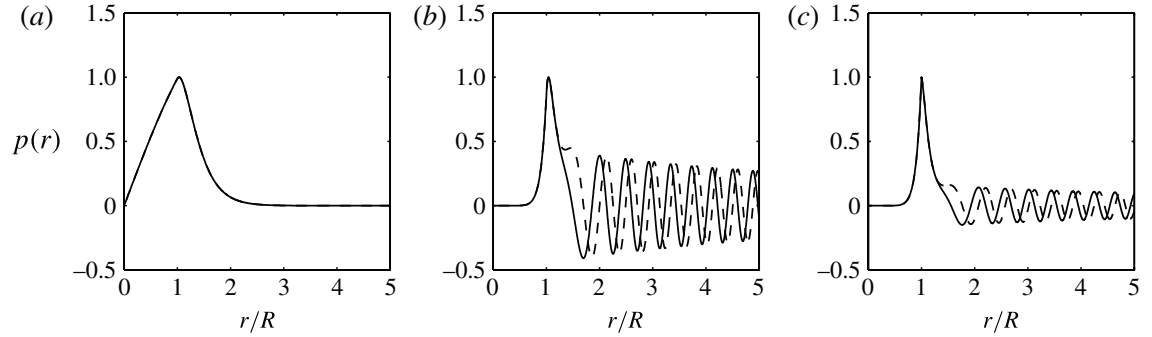

FIGURE 3. Eigenfunctions $p(r)$ for (*a*) $(m, Ro) = (1, -1)$, (*b*) $(m, Ro) = (10, -1)$, and (*c*) $(m, Ro) = (10, -2/3)$ for the first branch at $kR\Omega/N = 2$. The solid and dashed lines are the real part and imaginary part, respectively.

starts at $k = 0$ from the two-dimensional dispersion relation $\omega = (m - 1)\Omega$, and tends to $m\Omega$ as k increases regardless of Ro and m. In contrast, the next branches start at a finite axial wavenumber $k > 0$ and $\omega/\Omega = \omega_-(\infty)/\Omega = 2/Ro$ and tend to $\omega/\Omega = \omega_-(0)/\Omega = m + (2/Ro + 2)$ as $k \to \infty$. This frequency range corresponds to the configurations for which there exist a confined inner wave region. For $m = 1$, there is another family of branches which start from $\omega/\Omega = \omega_+(\infty)/\Omega = -2/Ro$ and tend to $\omega/\Omega = \omega_+(0)/\Omega = m - (2/Ro + 2)$ as $k \to \infty$. This family of branches exists only if $m - (2/Ro + 2) < -2/Ro$ (i.e. only if $m < 2$). As seen in figure 2(*b*), the first branch for $m = 10$ is the most unstable and the growth rate of the next branches is much smaller, and only positive when ω_r is in the range (3.2), i.e. only when there exist two wave regions (figure 1*b*).

Some examples of pressure eigenfunctions for the first branch for $m = 1$ and $m = 10$ for $Ro = -1$ are displayed in figures 3(*a*) and 3(*b*). A radiating inertia–gravity wave train is clearly visible outside the vortex core for $m = 10$ (figure 3*b*) in contrast to $m = 1$ (figure 3*a*).

4.2. *Variation with the azimuthal wavenumber*

Figure 4 shows the frequency ω_r and growth rate ω_i of the first branch (i.e. the most unstable branch) for several azimuthal wavenumbers from $m = 1$ to $m = 50$

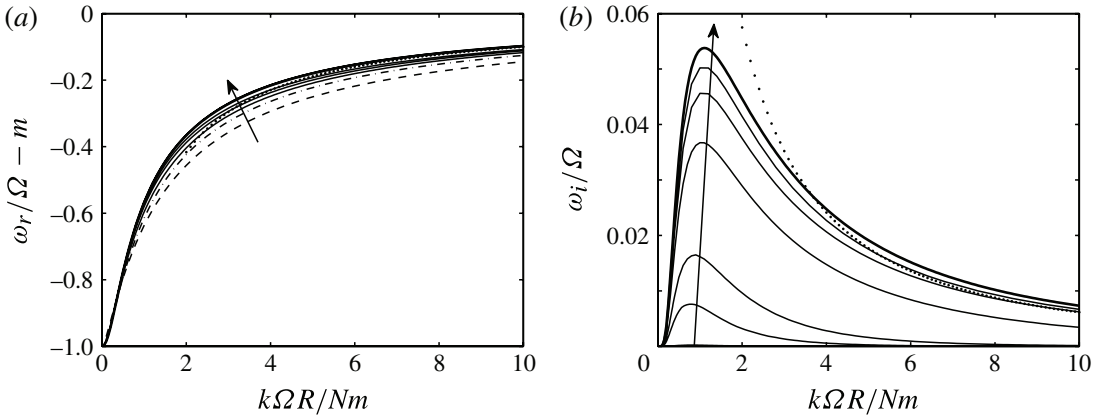

FIGURE 4. (*a*) Rescaled frequency ($\omega_r/\Omega - m$) and (*b*) growth rate ω_i as a function of rescaled vertical wavenumber $k\Omega R/(Nm)$ at $Ro = -1$. The dashed line, dot-dashed line and solid lines are numerical results for $m = 1$, $m = 2$ and $m = [3, 4, 5, 10, 20, 50]$. The arrows indicate an increase of m. The bold and dotted lines are asymptotic results for large m (4.2) and for both large $\tilde{k}$ and m (A 6) for $m = 20$, respectively.

for $Ro = -1$. Following Le Dizès & Riedinger (2010), the frequency and vertical wavenumber have been rescaled as $\omega_r/\Omega - m$ and $kR\Omega/(Nm)$. With these scalings, the frequency of every azimuthal wavenumber collapses approximately on the same curve (figure 4*a*). As seen in figure 4(*b*), the growth rate is positive only if $m \geqslant 3$, as predicted in § 3, and increases monotonically with m. Le Dizès & Riedinger (2010) (see also Candelier, Le Dizès & Millet 2012) have shown that the limit $m \to \infty$ can be analysed asymptotically by introducing the rescaled variables: $\bar{r} = m(r/R - 1)$, $\omega_0 = \omega/\Omega - m$, $k_1 = kR\Omega/(Nm)$ where $(\bar{r}, \omega_0, k_1)$ and Ro are assumed to be of order one. For large m, (2.1) then becomes at leading order

$$\frac{\mathrm{d}^2 p}{\mathrm{d}\bar{r}^2} - \frac{1}{\bar{\Delta}}\frac{\mathrm{d}\bar{\Delta}}{\mathrm{d}\bar{r}}\frac{\mathrm{d}p}{\mathrm{d}\bar{r}} + \left[-k_1^2\bar{\Delta} - 1 - 8\left(\frac{1+Ro}{Ro\,\bar{\Delta}}\right)\right] p = O\left(\frac{1}{m}\right), \tag{4.1}$$

where $\bar{\Delta}(\bar{r}) = 4(1+Ro)/Ro^2 - (\omega_0 + 2\bar{r})^2$. This equation is valid around $\bar{r} \sim O(1)$ (i.e. $r \sim R$) and it has to be solved numerically except for the particular value $Ro = -1$, where an analytical solution can be found:

$$p(\bar{r}) = C\mathrm{e}^{-\mathrm{i}\bar{z}}[M(a, b, 2\mathrm{i}\bar{z}) + \gamma U(a, b, 2\mathrm{i}\bar{z})], \tag{4.2}$$

where C is a constant, $\bar{z} = k_1(\omega_0 + 2\bar{r})^2/4$, $a = -1/4 - \mathrm{i}/(8k_1)$, $b = -1/2$, and M and U denote the Kummer functions (Abramowitz & Stegun 1965). If one imposes $\gamma = -\Gamma(-1/2)\exp^{\mathrm{i}\pi a}/\Gamma(-a - 1/2)$, where Γ is the Gamma function, then (4.2) matches the outgoing wave (2.4) as $\bar{r} \to \infty$.

The results obtained by using the asymptotic solution (4.2) in the dispersion relation (2.2) are shown by bold lines in figure 4. We see that the numerical results tend to these asymptotic results as m increases. The maximum growth rate in the limit $m \to \infty$ is $\omega_i \approx 0.053\Omega$ and is reached for $kR\Omega/(Nm) \approx 1$. It is worth pointing out that this growth rate is of the same order of magnitude as the values computed in non-rotating stratified fluids (Billant & Le Dizès 2009) and for the flow around a rotating cylinder in strongly stratified fluids in the range $Ro > 0$ (Le Dizès & Riedinger 2010; Riedinger *et al.* 2011). Note, however, that the first branch is absent in the case of the flow around a rotating cylinder because of the different boundary condition on the cylinder.

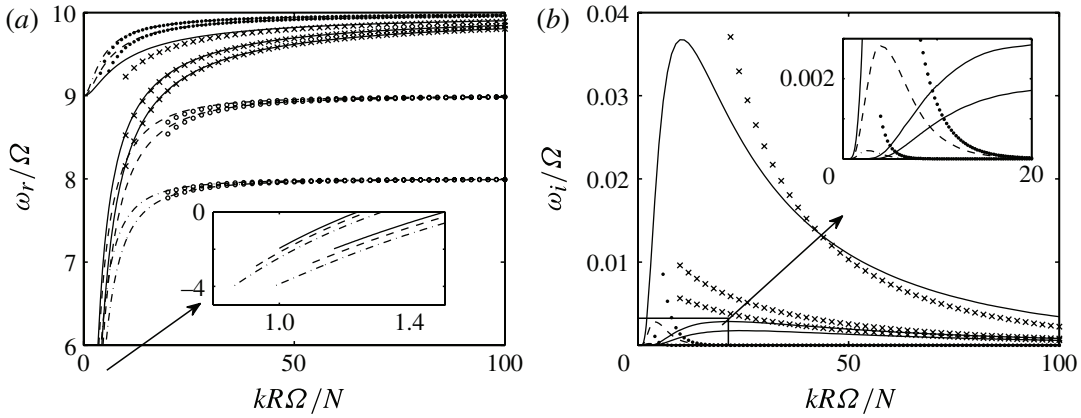

FIGURE 5. (*a*) Frequency ω_r and (*b*) growth rate of the first three branches for $m = 10$ for different Rossby numbers: solid lines, $Ro = -1$; dashed lines, $Ro = -2/3$; dot-dashed lines, $Ro = -1/2$. Symbols represent the WKBJ predictions for large $\tilde{k}$ (• (A 3), ∘ (A 4)) and for both large $\tilde{k}$ and m (× (A 6)). The inset in (*a*) shows the region around $\omega/\Omega = 2/Ro$ and the inset in (*b*) shows the region around $k = 0$. For $Ro = -2/3$ and $Ro = -1/2$, only the growth rate of the first branch is displayed because the growth rate of the next branches is too small.

4.3. *Effect of the Rossby number*

Figure 5 shows the frequency and the growth rate of the first three branches for three different Rossby numbers, $Ro = -1, -2/3$ and $-1/2$, for the typical azimuthal wavenumber $m = 10$. In figure 5(*a*), we can see that the frequency of the first branch lies in the range $[(m-1)\Omega, m\Omega]$ independently of Ro. This is observed for all the azimuthal wavenumbers. In contrast, the frequency range of the next branches depends on Ro, and corresponds when $m \geqslant 3$ to the range $\omega_-(\infty) < \omega < \omega_-(0)$, for which a confined inner wave region exists, as discussed in § 4.1. The frequency predicted by the WKBJ analyses that are performed in the Appendix are plotted by symbols in figure 5(*a*). The asymptotic and numerical frequencies are in good agreement for large vertical wavenumber $\tilde{k}$. The growth rate predicted by the WKBJ analyses is plotted with the same symbols in figure 5(*b*). It is in good agreement with the numerical growth rate only for large axial wavenumber.

The maximum growth rate as a function of Ro is plotted in figure 6. We can see that it decreases quickly when Ro is increased from $Ro = -1$ and becomes very small when $Ro \gtrsim -0.4$. The maximum growth rate is always attained by the first branch regardless of the Rossby number. Since the frequency of the first branch is always in the range $(m-1)\Omega < \omega < m\Omega$, we can deduce by considering the epicyclic frequencies $\omega_\pm$ that there is only a single outer wave region and no inner wave region for the first branch when $-2/3 \leqslant Ro < -2/m$ for any m (see the example in figure 1*c*). Quite strikingly, the growth rate remains positive for $Ro \geqslant -2/3$ and there is a strong wave emission (figure 3*c*). As explained in the Appendix, there is actually a second wave region concealed in the vorticity jump at $r = R$. When $Ro > -2/m$, there is no outer wave region and the growth rate is purely zero.

5. Stability of the smoothed Rankine vortex

We now investigate the stability of a more realistic vortex profile with a continuous vorticity profile. More specifically, we consider the smoothed Rankine

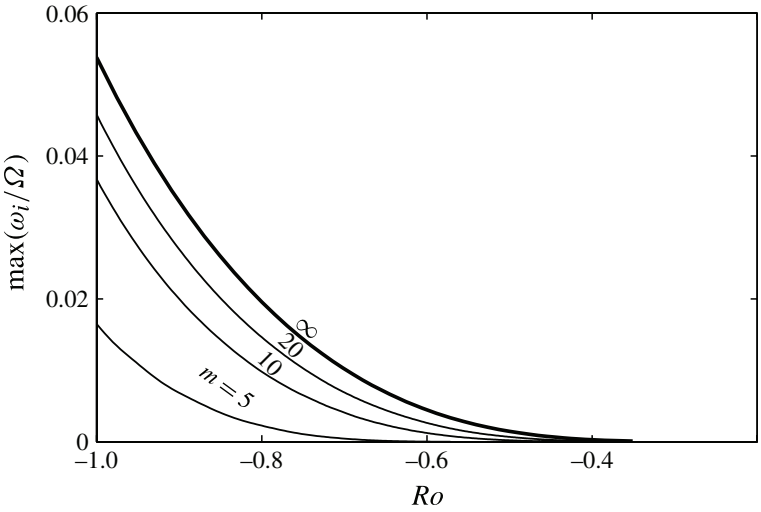

FIGURE 6. Maximum growth rate $\max(\omega_i)$ of the first branch as a function of Ro for different m. The bold line shows the limit $m = \infty$ computed from (4.1).

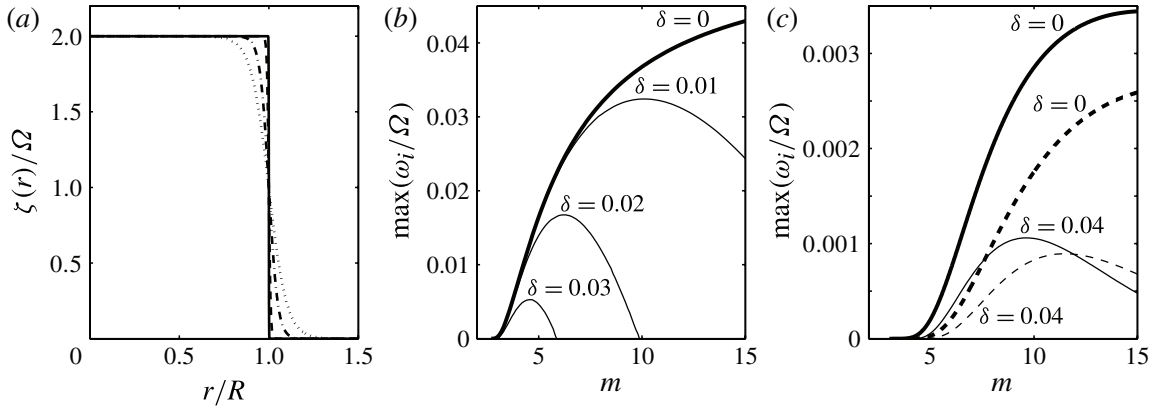

FIGURE 7. (*a*) Vertical vorticity of the smoothed Rankine vortex (5.1) for $\delta = 0.001$ (solid lines), $\delta = 0.01$ (dashed lines), $\delta = 0.05$ (dot-dashed lines) and $\delta = 0.1$ (dotted lines). (*b*) Maximum growth rate $\max(\omega_i)$ of the first branch as a function of m for different values of δ for $Ro = -1$. (*c*) Maximum growth rate $\max(\omega_i)$ of the second branch (solid lines) and the third branch (dashed lines) as a function of m for $\delta = 0$ and $\delta = 0.04$ for $Ro = -1$. The bold lines in (*b,c*) represent the limit $\delta = 0$ (i.e. the Rankine vortex).

vortex introduced by Schecter & Montgomery (2004) with axial vorticity

$$\zeta(r) = \Omega \left[1 - \tanh\left(\frac{r/R - 1}{\delta}\right)\right], \tag{5.1}$$

where δ is a smoothness parameter. As illustrated in figure 7(*a*), the vorticity jump becomes smoother as δ increases from zero. For this profile, a classical shooting method is used to solve (2.1) (see Schecter & Montgomery 2004). The numerical integration is started at $r = 0$ using the asymptotic behaviour $p(r) \sim r^{|m|}$.

Figure 7(*b*) shows the maximum growth rate of the first branch as a function of m for different values of δ for $Ro = -1$. We see that high azimuthal wavenumbers are stabilized for finite δ, so the most amplified azimuthal wavenumber m_{max} becomes

finite. The value of m_{max} decreases rapidly with δ (figure 7*b*) so that the first branch becomes stable for all m when $\delta > 0.038$. A similar stabilization is observed for the second and third branches (figure 7*c*). However, the stabilizing effect tends to decrease with the branch number for a given value of δ. Thus, the most amplified wavenumber m_{max} increases with the branch number, as shown in figure 7(*c*) for $\delta = 0.04$.

This stabilization is due to the presence of a singularity at the critical radius r_c where $\omega = mU_\theta(r_c)/r_c$ as soon as δ is non-zero. As discussed in Schecter & Montgomery (2004), this singularity has a stabilizing effect whose magnitude is proportional to the vorticity gradient at the critical radius $|\zeta'(r_c)|$. This vorticity gradient can be estimated by using the fact that the critical point is approximately located at $r_c \approx R\sqrt{m\Omega/\omega_r}$ for small δ. From figure 4, we also see that the frequency of the most unstable mode is $\omega_r \approx (m - 0.5)\Omega$ independently of m. Thus, for large m, the vorticity gradient is about $|\zeta'(r_c)| \approx \Omega/(R\delta\cosh^2(0.25/(m\delta)))$. This implies that the damping rate is small when $m\delta \ll 1$ and large of order $O(1/\delta)$ when $m\delta \gg 1$. This explains why the most amplified azimuthal wavenumber scales as $m_{max} = O(1/\delta)$ (figure 7*b*). The damping rate is smaller for the next branches because the critical radius is located farther from $r = R$ where the vorticity gradient is smaller, since the frequency ω_r of the most amplified mode is slightly smaller than for the first branch.

It seems that this stabilizing effect can render the vortex completely stable or neutral for sufficiently large vorticity smoothness. For example, we have investigated the stability of the Lamb–Oseen vortex whose vorticity profile is very smooth. A Chebyshev spectral stability code (Antkowiak & Brancher 2007) has been used in order not to miss any unstable mode. Although the growth rates are generally very small, we have always found that they are negative for the range of axial and azimuthal wavenumbers investigated.

6. Conclusion and discussion

The stability of the Rankine vortex and the smoothed Rankine vortex has been investigated in a strongly stratified and rotating fluid in the anticyclonic range, $-1 \leqslant Ro < 0$, which is stable to the centrifugal instability. For the Rankine vortex, the azimuthal wavenumbers $m \geqslant 3$ are unstable, whereas $m = [0, 1, 2]$ are neutral. The maximum growth rate is $\omega_i \approx 0.05\Omega$, and is reached in the limit of infinite azimuthal wavenumber and for $Ro = -1$. The maximum growth rate decreases when the Rossby number is increased from $Ro = -1$ and becomes negligible when $Ro \gtrsim -0.4$. By means of WKBJ analyses, we have shown that this instability originates from the radiation of inertia–gravity waves. In the case of the smoothed Rankine vortex, a critical layer stabilizes the radiative instability all the more when the vorticity profile is smooth, as reported by Schecter & Montgomery (2004). In sharp contrast with the Rankine vortex, the most amplified azimuthal wavenumber is finite, and scales in inverse proportion to the smoothness parameter δ.

This radiative instability may operate on anticyclonic geophysical vortices such as the Meddies since the e-folding time $T = 1/\omega_i$ can be as low as 10 days if we take a typical turnover time of 2–7 days (Bower, Armi & Ambar 1997). However, geophysical eddies have a small vertical size, and it would be important to determine whether the radiative instability can operate on such a non-columnar vortex. The stability of other basic flows such as Taylor–Couette flow will also be investigated in the future.

Acknowledgements

We thank two anonymous referees for their thoughtful comments. This work was supported by the National Research Agency (ANR 2011 Blanc SIMI 5-6 012-02).

Appendix. WKBJ analysis

In this appendix, we solve (2.1) for the unstable azimuthal wavenumbers, i.e. $m \geqslant 3$, by means of a WKBJ analysis for large vertical wavenumbers following Billant & Le Dizès (2009) and Le Dizès & Billant (2009). As summarized in § 3, the first condition for the existence of radiative instability is the presence of a region extending towards infinity where the WKBJ approximation (3.1) is wavelike. Thus, we first assume that $\Delta < 0$ for $r \to \infty$. In order to satisfy the boundary condition, we choose that the WKBJ approximation corresponds to an outgoing wave for $r \to \infty$. Therefore, we set $B = 0$ for $r > r_t$ in (3.1). In the neighbourhood of the turning point r_t where the WKBJ approximation breaks down, (2.1) approximates at leading order to

$$\frac{\mathrm{d}^2 p}{\mathrm{d}\tilde{r}^2} - \frac{1}{\tilde{r}}\frac{\mathrm{d}p}{\mathrm{d}\tilde{r}} + \tilde{r}p = O(\epsilon), \tag{A 1}$$

where $\epsilon = 1/\left(-\Delta'(r_t)\tilde{k}^2\right)^{1/3}$ and $\tilde{r} = (r - r_t)/\epsilon$. Note that $\epsilon > 0$ since $\Delta'(r_t) < 0$. The solution of (A 1) is $p(\tilde{r}) = a_1 \mathrm{Ai}'(-\tilde{r}) + b_1 \mathrm{Bi}'(-\tilde{r})$, where Ai and Bi denote Airy functions and a_1 and b_1 are constants. From the asymptotic behaviour of the Airy functions for $\tilde{r} \to +\infty$ and $\tilde{r} \to -\infty$, we find the WKBJ approximation in the region $(r < r_t)$ that matches the outgoing wave for $r > r_t$ as

$$p(r) \sim A\mathrm{e}^{-\mathrm{i}\pi/4}\frac{\Delta^{1/4}}{r^{1/2}}\left[\frac{1}{2}\mathrm{e}^{-\tilde{k}\int_r^{r_t}\sqrt{\Delta(t)}\,\mathrm{d}t} + \mathrm{i}\mathrm{e}^{\tilde{k}\int_r^{r_t}\sqrt{\Delta(t)}\,\mathrm{d}t}\right]. \tag{A 2}$$

When there is no other turning point between R and r_t, the approximation (A 2) remains valid until $r = R$ and can be directly inserted into the dispersion relation (2.2). This is the case when the frequency is such that $\max(\omega_+(\infty), \omega_-(R_+)) < \omega_r < \omega_+(R_+)$ (see § 3 and figure 1*c*). The dispersion relation can be solved explicitly by means of an expansion in powers of $\tilde{k}$. For the first branch for $-2/3 \leqslant Ro < -2/m$, the solution (2.3) in the vortex core is always exponential, giving at leading order

$$\frac{\omega_r}{\Omega} = m - \frac{\alpha}{\tilde{k}R\Omega}, \quad \frac{\omega_i}{\Omega} = \frac{\alpha^2}{2m}\sqrt{\frac{2}{Ro}\left(\frac{2}{Ro}+2\right)}\frac{W}{\tilde{k}R\Omega}, \tag{A 3}$$

where $\alpha = 2m/(|2/Ro| + \sqrt{2(2/Ro+2)/Ro})$ and $W = \exp(-2\tilde{k}\int_R^{r_t}\sqrt{\Delta(t)}\,\mathrm{d}t)$. Equation (A 3) shows that the frequency of the first branch tends to $m\Omega$ as $\tilde{k} \to \infty$ and its growth rate is of order $O(W/\tilde{k})$. It is in good agreement with the numerical results, as shown by the filled circles in figure 5. Remarkably, the growth rate ω_i is positive even if there is apparently a single wave region. In fact, there is also an infinitely small wave region at $r = R$ due to the vorticity jump of the Rankine vortex. This can be seen by considering the limit $\Delta' \gg 1$ in (2.1). When $Ro > -2/m$, the first branch has zero growth rate since there is no turning point, but the frequency ω_r remains identical to (A 3) for large $\tilde{k}$. For the next branches, the solution (2.3) in the vortex core is wavelike, yielding at leading order in $\tilde{k}$

$$\frac{\omega_r}{\Omega} = m + \left(\frac{2}{Ro}+2\right) + \frac{\beta^2}{2(2/Ro+2)}\frac{1}{(\tilde{k}R\Omega)^2}, \tag{A 4}$$

where β satisfies $\beta + \arctan(m/\beta) = \pi(n + (2m+1)/4)$ and n is the branch number. In this case, the growth rate is found to be of higher order, $O(W/\tilde{k}^3)$, and is thus much smaller than for the first branch. Equation (A 4) is plotted with open circles in figure 5.

When the frequency is in the range $\omega_-(\infty) < \omega_r < \omega_-(R_+)$, the solution (A 2) is no longer valid at $r = R$ because there is a second turning point (see § 3 and figure 1*c*). When m is large, this second turning point r_{t2} is close to the first one r_{t1} and also close to the vortex radius $r = R$, so classical WKBJ approximation with two separate turning points (Bender & Orszag 1978) is not accurate. A better approximation can be obtained by considering the local equation around the radius $r_o = R\sqrt{m^2/(2/Ro + m\omega/\Omega)}$ where Δ is maximal (i.e. $\Delta'(r_o) = 0$):

$$\frac{\mathrm{d}^2 p}{\mathrm{d}\tilde{r}^2} - \frac{2\tilde{r}}{\tilde{r}^2 - \lambda}\frac{\mathrm{d}p}{\mathrm{d}\tilde{r}} + (\tilde{r}^2 - \lambda)p = O(\epsilon), \tag{A 5}$$

where $\epsilon = R\,(r_o/R)^{3/4}\,/\,(2m\tilde{k}R\Omega)^{1/2}$, $\lambda = \tilde{k}R\Omega\{2(1+m^2)/Ro^2 + 2m\omega/(Ro\Omega)\}/(2/Ro + m\omega/\Omega)^{3/2}$ and $\tilde{r} = (r - r_o)/\epsilon$ with $\tilde{r} = O(1)$. The solution of (A 5) is

$$p(\tilde{r}) \sim \mathrm{e}^{\mathrm{i}\tilde{r}^2/2}\left[(1+\mathrm{i}\tilde{r}^2)U\left(\frac{\mathrm{i}\lambda+3}{4}, \frac{3}{2}, -\mathrm{i}\tilde{r}^2\right) + \frac{\mathrm{i}(\mathrm{i}\lambda+3)}{2}\tilde{r}^2 U\left(\frac{\mathrm{i}\lambda+7}{4}, \frac{5}{2}, -\mathrm{i}\tilde{r}^2\right)\right] \tag{A 6}$$

where U denotes the Kummer function (Abramowitz & Stegun 1965). This solution matches the outgoing wave as $\tilde{r} \to \infty$. When r_o is close to $r = R$, (A 6) can be directly inserted into the dispersion relation (2.2) and provides a good prediction for the frequency and the growth rate for large $\tilde{k}$ and m, as shown by the dotted lines in figure 4 and crosses in figure 5.

REFERENCES

Abramowitz, M. & Stegun, I. A. 1965 *Handbook of Mathematical Functions*. Dover.

Antkowiak, A. & Brancher, P. 2007 On vortex rings around vortices: an optimal mechanism. *J. Fluid Mech.* **578**, 295–304.

Bender, C. M. & Orszag, S. A. 1978 *Advanced Mathematical Methods for Scientists and Engineers*. McGraw-Hill.

Billant, P. & Chomaz, J.-M. 2001 Self-similarity of strongly stratified inviscid flows. *Phys. Fluids* **13**, 1645.

Billant, P. & Le Dizès, S. 2009 Waves on a columnar vortex in a strongly stratified fluid. *Phys. Fluids* **21**, 106602.

Bower, A., Armi, L. & Ambar, I. 1997 Lagrangian observations of Meddy formation during a Mediterranean undercurrent seeding experiment. *J. Phys. Oceanogr.* **27**, 2545–2575.

Broadbent, E. & Moore, D. W. 1979 Acoustic destabilization of vortices. *Phil. Trans. R. Soc. Lond. Ser.* A **290**, 353.

Candelier, J., Le Dizès, S. & Millet, C. 2012 Inviscid instability of a stably stratified compressible boundary layer on an inclined surface. *J. Fluid Mech.* **694**, 524–539.

Ford, R. 1994 The instability of an axisymmetric vortex with monotonic potential vorticity in rotating shallow water. *J. Fluid Mech.* **280**, 303–334.

Kloosterziel, R. C. & van Heijst, G. J. F. 1991 An experimental study of unstable barotropic vortices in a rotating fluid. *J. Fluid Mech.* **223**, 1–24.

Le Dizès, S. & Billant, P. 2009 Radiative instability in stratified vortices. *Phys. Fluids* **21**, 096602.

Le Dizès, S. & Lacaze, L. 2005 An asymptotic description of vortex Kelvin modes. *J. Fluid Mech.* **542**, 69–96.

Le Dizès, S. & Riedinger, X. 2010 The strato-rotational instability of Taylor–Couette and Keplerian flows. *J. Fluid Mech.* **660**, 147–161.

MÉNESGUEN, C., HUA, B. L., PAPENBERG, C., KLAESCHEN, D., GÉLI, L. & HOBBS, R. 2009 Effect of bandwidth on seismic imaging of rotating stratified turbulence surrounding an anticyclonic eddy from field data and numerical simulations. *Geophys. Res. Lett.* **36**, L00D05.

RIEDINGER, X., LE DIZÈS, S. & MEUNIER, P. 2010 Viscous instability of a Lamb–Oseen vortex in a stratified fluid. *J. Fluid Mech.* **645**, 255–278.

RIEDINGER, X., LE DIZÈS, S. & MEUNIER, P. 2011 Radiative instability of the flow around a rotating cylinder in a stratified fluid. *J. Fluid Mech.* **672**, 130–146.

SCHECTER, D. A. 2008 The spontaneous imbalance of an atmospheric vortex at high Rossby number. *J. Atmos. Sci.* **65**, 2498.

SCHECTER, D. A. & MONTGOMERY, M. T. 2004 Damping and pumping of a vortex Rossby wave in a monotonic cyclone: critical layer stirring versus inertia–buoyancy wave emission. *Phys. Fluids* **26** (5), 1334.

SCHECTER, D. A. & MONTGOMERY, M. T. 2006 Conditions that inhibit the spontaneous radiation of spiral inertia–gravity waves from an intense mesoscale cyclone. *J. Atmos. Sci.* **63**, 435.

SMYTH, W. D. & MCWILLIAMS, J. C. 1998 Instability of an axisymmetric vortex in a stably stratified, rotating environment. *Theor. Comput. Fluid Dyn.* **11**, 305–322.

VANNESTE, J. & YAVNEH, I. 2004 Exponentially small inertia–gravity waves and the breakdown of quasigeostrophic balance. *J. Atmos. Sci.* **61**, 211–223.

VANNESTE, J. & YAVNEH, I. 2007 Unbalanced instabilities of rapidly rotating stratified shear flows. *J. Fluid Mech.* **584**, 373–396.

2 Stability of the stratified Taylor-Couette flow

2.1 Analogy between the Rankine vortex and the Taylor-Couette flow

In this section, we consider the Taylor-Couette flow in a stratified fluid. The Taylor-Couette flow is the flow between two rotating co-axial cylinders and has an angular velocity $\Omega(r) = A + B/r^2$ where A and B are detailed as (2.9) in chapter 2. In fact, this flow resembles the absolute angular velocity of the Rankine vortex in a rotating fluid outside the vortex core: $\Omega_b + R^2\Omega/r^2$. By matching the equations of motions, it can be shown that these two flows are equivalent if the Rossby number is

$$Ro = \frac{\Omega}{\Omega_b} = \frac{B}{R_i^2 A} = \frac{1-\mu}{\mu - \eta^2}, \tag{4.1}$$

where $\mu = \Omega_o/\Omega_i$ and $\eta = R_i/R_o$ are the two control parameters of the Taylor-Couette flow. Although the boundary conditions for the Rankine vortex and the Taylor-Couette flow are different, their stability properties are therefore expected to be similar.

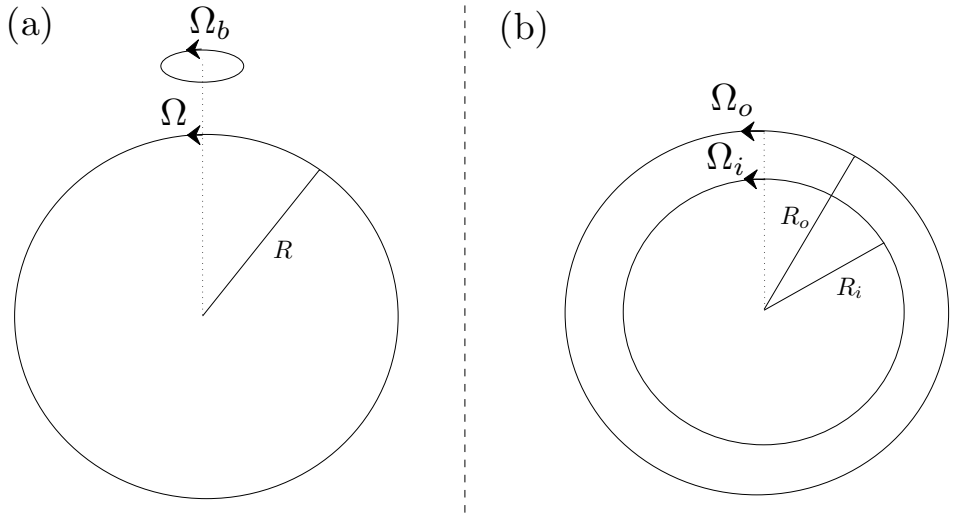

Figure 4.1: Analogy between (a) the Rankine vortex in a rotating frame and (b) the Taylor-Couette flow.

From (4.1), we see that the regime of cyclonic rotation $Ro > 0$ corresponds to $\eta^2 < \mu < 1$ whereas the regime of anticyclonic rotation $Ro < 0$ corresponds to $\mu < \eta^2$ or $\mu > 1$. In particular, the regime $Ro < -1$, corresponds to $\mu < \eta^2$ which are the regimes of the centrifugal instability according to the Rayleigh criterion (Lord Rayleigh, 1917; Kloosterziel & van Heijst, 1991). In contrast, the ranges $-1 < Ro < 0$ and $\mu > 1$ are equivalent and centrifugally stable.

Yavneh *et al.* (2001) and Molemaker*et al.* (2001) have shown that the stratorotational instability for the Taylor-Couette flow exists in the regime $\eta^2 < \mu < 1$ which is clearly related to the radiative instability in the cyclonic regime $Ro > 0$ (Le Dizès & Riedinger, 2010). On the other hand, there is no study of the Taylor-Couette flow in the regime $\mu > 1$ while we found that the radiative instability for the Rankine vortex still exists in the corresponding anticyclonic regime $-1 < Ro < 0$. Thus, in the following section, we investigate the stability of the Taylor-Couette flow in a stratified fluid in the regime $\mu > 1$.

2.2 The stably stratified Taylor-Couette flow is always unstable except for solid-body rotation

Article submitted to Journal of Fluid Mechanics.

Under consideration for publication in J. Fluid Mech. 1

The stably stratified Taylor-Couette flow is always unstable except for solid-body rotation

JUNHO PARK†, AND PAUL BILLANT
LadHyX, CNRS, Ecole Polytechnique, F-91128, Palaiseau Cedex, France

(Received ?; revised ?; accepted ?. - To be entered by editorial office)

The stability of the flow between two concentric cylinders is studied numerically and analytically when the fluid is stably stratified. We show that such flow is unstable when the angular velocity $\Omega(r)$ increases along the radial direction, a regime never explored before. The instability is highly non-axisymmetric and involves the resonance of two families of inertia-gravity waves like for the strato-rotational instability. The growth rate is maximum when only the outer cylinder is rotating and goes to zero when $\Omega(r)$ is constant. The sufficient condition for linear, inviscid instability derived previously: $d\Omega^2/dr < 0$ is therefore extended to $d\Omega^2/dr \neq 0$, meaning that only the regime of solid-body rotation is stable in stratified fluids. A WKBJ analysis in the inviscid limit, confirmed by the numerical results, shows that the instability occurs only when the Froude number is below a critical value and only for a particular band of azimuthal wavenumbers. It is also demonstrated that the instability originates from a reversal of the radial group velocity of the waves, or equivalently from a wave over-reflection phenomenon. The instability persists in presence of viscous effects.

Key words:

1. Introduction

The Taylor-Couette flow is a canonical and popular flow that has led to a very large number of studies and significant advances in the understanding of fluid stability and transitions to chaos and turbulence (Andereck *et al.* 1986; Dubrulle *et al.* 2005*a*). It consists in the sheared flow between two independently rotating concentric cylinders. The base flow is steady and axisymmetric with angular velocity,

$$\Omega(r) = A + \frac{B}{r^2}, \tag{1.1}$$

with $A = (r_o^2\Omega_o - r_i^2\Omega_i)/(r_o^2 - r_i^2)$ and $B = r_i^2 r_o^2(\Omega_i - \Omega_o)/(r_o^2 - r_i^2)$, where (r_i, r_o) and (Ω_i, Ω_o) are the radius and the angular velocity of the inner and outer cylinder, respectively.

According to the Rayleigh criterion, such base flow is unstable to the centrifugal instability in an inviscid fluid if the angular momentum decreases in the radial direction: $d(r^2\Omega)/dr < 0$ or equivalently $\mu < \eta^2$ where $\mu = \Omega_o/\Omega_i$ and $\eta = r_i/r_o$ are the two classical control parameters of the Taylor-Couette flow. The Rayleigh criterion remains valid in the presence of a stable density stratification along the axial (vertical) direction

† Email address for correspondence: junho.park@ladhyx.polytechnique.fr

(Ooyama 1966; Billant & Gallaire 2005). Such flow which combines horizontal shear and vertical stratification is of high interest in geophysics and astrophysics: for example, the stratified Taylor-Couette flow serves as a model for instabilities in equatorial oceans (Hua *et al.* 1997*b*), or in Keplerian flows in accretion disks (Dubrulle *et al.* 2005*b*).

Early studies of the stratified Taylor-Couette flow have been mostly performed when the outer cylinder is at rest ($\mu = 0$) (Withjack & Chen 1974; Hua *et al.* 1997*a*; Boubnov *et al.* 1995; Caton *et al.* 2000). They reported that the stratification in viscous fluid stabilizes the flows as one might intuitively expect since the buoyancy force is restoring. Surprisingly, Yavneh *et al.* (2001) and Molemaker *et al.* (2001) have however shown that the Taylor-Couette flow with sufficiently strong stratification remains unstable beyond the Rayleigh threshold $\mu = \eta^2$. They found that a sufficient condition for inviscid instability in stratified fluids is actually $d\Omega^2/dr < 0$ corresponding to $\mu < 1$. The dominant instability beyond the Rayleigh line ($\eta^2 < \mu < 1$) is non-axisymmetric and therefore different from the axisymmetric Taylor vortices of the centrifugal instablity. This instability, now referred as the Strato-Rotational Instability (SRI) (Dubrulle *et al.* 2005*b*), comes from the resonant interaction between two boundary-trapped waves on each cylinder (Yavneh *et al.* 2001; Molemaker *et al.* 2001; Le Dizès & Riedinger 2010). However, Le Dizès & Riedinger (2010) have found that the flow remains unstable when the outer cylinder is absent but the SRI transforms to a radiative instability (Le Dizès & Billant 2009; Billant & Le Dizès 2009; Riedinger *et al.* 2010; Riedinger *et al.* 2011). Stability analysis (Shalybkov & Rüdiger 2005) and experiments (Le Bars & Le Gal 2007) have shown that the threshold for the SRI in viscous fluids is $\mu \approx \eta$ so that the flow is stable for $\eta \lesssim \mu < 1$.

Even though the condition $d\Omega^2/dr < 0$ ($\mu < 1$) has been proposed as only a sufficient condition for inviscid instability in stratified fluids (Yavneh *et al.* 2001; Molemaker *et al.* 2001), the regime where the angular velocity increases with r ($\mu > 1$) has been generally thought to be stable for the stratified Taylor-Couette flow (Yavneh *et al.* 2001; Molemaker *et al.* 2001; Le Dizès & Riedinger 2010). To our knowledge, however, this regime has not been explored. Nevertheless, Vanneste & Yavneh (2007) have studied the stability of the rotating stratified horizontal plane Couette flow in a channel which shares many similarities with the stratified Taylor-Couette flow. In particular, anticyclonic and cyclonic shears correspond to $\mu < 1$ and $\mu > 1$, respectively. Interestingly, they have shown by means of an asymptotic analysis in the limit of small Rossby number that such plane Couette flow is unconditionally unstable, i.e. for both anticyclonic and cyclonic shears, However, the growth rate is reported to be much smaller in the cyclonic case than in the anticyclonic case.

Another related study concerns the stability of a columnar vertical Rankine vortex in a stratified rotating fluid. Park & Billant (2012*a*) have shown that such vortex is unstable to a radiative instability in the centrifugally stable anticyclonic regime: $-1 < Ro < 0$, where $Ro = \Omega_v/\Omega_b$ is the Rossby number with Ω_v the angular velocity in the vortex core and Ω_b the angular velocity of the background rotation (Note that the meanings of "anticyclonic" for a vortex and for the plane Couette flow differ Vanneste & Yavneh (2007)). The potential flow outside the vortex core has linearized perturbation equations equivalent to those of the Taylor-Couette flow if the Rossby number is set to

$$Ro = \frac{1-\mu}{\mu-\eta^2}. \tag{1.2}$$

This relation shows that the regime $\mu > 1$ for the Taylor-Couette flow corresponds to $-1 \leqslant Ro < 0$ for a vortex. Although the boundary conditions completely differ between

the two flows, this suggests that the regime $\mu > 1$ might be unstable since the radiative and SRI instabilities are closely related (Le Dizès & Riedinger 2010).

In this paper, we shall show that the stratified Taylor-Couette flow for $\mu > 1$ is indeed also unstable to the SRI. In contrast to the plane Couette flow (Vanneste & Yavneh 2007), the growth rates in the regime $\mu < 1$ and $\mu > 1$ are comparable. Strikingly, we shall see that the stratified inviscid Taylor-Couette flow is stable only in the limit of solid-body rotation ($\mu = 1$).

The paper is organized as follows. The problem is formulated in §2. A typical example of instability is first described in §3. In §4, a WKBJ asymptotic analysis explains the instability mechanism and provides general conditions for instability. The effects of the main parameters of the problem are investigated numerically in §5.

2. Problem formulation

We consider the linear stability of the base flow (1.1) in a stratified fluid with a constant Brunt-Väisälä frequency $N = \sqrt{-(g/\rho_0)\partial\bar{\rho}/\partial z}$, where g is the gravity, $\bar{\rho}(z)$ the basic density profile along the vertical direction z and ρ_0 a reference density. The perturbations of velocity $\mathbf{u}' = (u_r', u_\theta', u_z')$ in cylindrical coordinates (r, θ, z), pressure p' and density ρ' are written in the form $(\mathbf{u}', p', \rho') = (u_r(r), u_\theta(r), u_z(r), p(r), \rho(r))\mathrm{e}^{\mathrm{i}(kz+m\theta-\omega t)} + \text{c.c.}$, where ω is the complex eigenfrequency, m the azimuthal wavenumber and k the vertical wavenumber. Under the Boussinesq approximation, the linearized equations of momentum, continuity and density conservation for the perturbations are

$$\mathrm{i}su_r - 2\Omega u_\theta = -\frac{1}{\rho_0}\frac{\mathrm{d}p}{\mathrm{d}r} + \nu\left[\nabla^2 u_r - \frac{u_r}{r^2} - \frac{2\mathrm{i}m}{r^2}u_\theta\right], \tag{2.1}$$

$$\mathrm{i}su_\theta + Zu_r = -\frac{\mathrm{i}mp}{\rho_0 r} + \nu\left[\nabla^2 u_\theta - \frac{u_\theta}{r^2} + \frac{2\mathrm{i}m}{r^2}u_r\right], \tag{2.2}$$

$$\mathrm{i}su_z = -\frac{\mathrm{i}k}{\rho_0}p - \frac{g}{\rho_0}\rho + \nu\nabla^2 u_z, \tag{2.3}$$

$$\frac{1}{r}\frac{\mathrm{d}(ru_r)}{\mathrm{d}r} + \frac{\mathrm{i}mu_\theta}{r} + \mathrm{i}ku_z = 0, \tag{2.4}$$

$$\mathrm{i}s\rho - \frac{N^2\rho_0}{g}u_z = D\nabla^2\rho, \tag{2.5}$$

where $s = -\omega + m\Omega$ is the Doppler-shifted frequency, $Z = \frac{1}{r}\frac{\mathrm{d}}{\mathrm{d}r}(r^2\Omega)$ the axial vorticity of the base flow, $\nabla^2 = \frac{\mathrm{d}^2}{\mathrm{d}r^2} + \frac{1}{r}\frac{\mathrm{d}}{\mathrm{d}r} - (k^2 + \frac{m^2}{r^2})$ the Laplacian operator, ν the kinematic viscosity and D the molecular diffusivity of the stratifying agent. The boundary conditions are $u_r = u_\theta = u_z = \frac{\mathrm{d}\rho}{\mathrm{d}r} = 0$ at both cylinders $r = r_i, r_o$. Due to the symmetry $\omega(k, m) = \omega(-k, m) = -\omega^*(-k, -m)$, we consider hereafter only positive k and m.

In the inviscid and non-diffusive limit $\nu = D = 0$, the equations (2.1)-(2.5) can be reduced to a single equation for the radial velocity u_r:

$$\frac{\mathrm{d}^2 u_r}{\mathrm{d}r^2} + \left(\frac{1}{r} - \frac{Q'}{Q}\right)\frac{\mathrm{d}u_r}{\mathrm{d}r} + \left[-\frac{k^2}{N^2 - s^2}\Delta - \frac{m^2}{r^2} - \frac{mrQ}{s}\left(\frac{Z}{r^2 Q}\right)' + Q\left(\frac{1}{rQ}\right)'\right]u_r = 0, \tag{2.6}$$

where $Q(r) = m^2/r^2 - k^2 s^2/(N^2 - s^2)$, $\Delta(r) = \phi - s^2$, $\phi = 2Z\Omega$ is the Rayleigh discriminant and the prime denotes differentiation with respect to r. In this limit, the boundary conditions reduce to $u_r = 0$ at $r = r_i, r_o$. The equation (2.6) has been solved

by a shooting method. The numerical integration is started from both cylinders toward a fitting point r_f using the boundary conditions and an initial guess ω. The Wronskian $W_k = u_r(r_f^+)u_r'(r_f^-) - u_r(r_f^-)u_r'(r_f^+)$ is computed from the two distinct values $(u_r(r_f^+), u_r'(r_f^+))$ and $(u_r(r_f^-), u_r'(r_f^-))$ on either side of r_f. An iterative secant method is used to find the value of ω for which the Wronskian vanishes (Schecter & Montgomery 2004).

The equations (2.1)-(2.5) have been solved by the Chebyshev collocation spectral method (Antkowiak & Brancher 2004; Fabre & Jacquin 2004). The five equations (2.1)-(2.5) are first reduced to three equations for (u_r, u_θ, ρ) which can be written into the compact form:

$$\omega \mathbf{B} \begin{pmatrix} u_r \\ u_\theta \\ \rho \end{pmatrix} = \mathbf{A} \begin{pmatrix} u_r \\ u_\theta \\ \rho \end{pmatrix}, \tag{2.7}$$

where $\mathbf{A}$ and $\mathbf{B}$ are differential operator matrices (For details, see Park (2012)). The continuity equation implies that the boundary condition $u_z = 0$ at $r = r_i, r_o$ transforms to $\frac{\mathrm{d}u_r}{\mathrm{d}r} = 0$ for this reduced system. The linear mapping

$$r = \frac{r_i - r_o}{2}\zeta + \frac{r_i + r_o}{2} \tag{2.8}$$

is used to map the Chebyshev domain $\zeta = 1 \to -1$ into $r = r_i \to r_o$. An advantage of this linear mapping is that the collocation points are concentrated near each cylinder so that boundary modes can be easily captured. The number of collocation points for the spectral method is chosen from 80 to 120 points depending on the control parameters. The spurious modes are eliminated by using a convergence criterion based on the spectral residual (Fabre & Jacquin 2004).

The seven control parameters of the problem $(\Omega_i, \Omega_o, r_i, r_o, N, \nu, D)$ can be expressed in terms of five independent non-dimensional numbers:

$$\mu = \frac{\Omega_o}{\Omega_i}, \quad \eta = \frac{r_i}{r_o}, \quad F = \frac{\Omega_o}{N}, \quad Re = \frac{\Omega_o r_o (r_o - r_i)}{\nu}, \quad Sc = \frac{\nu}{D}, \tag{2.9}$$

where F is the Froude number, Re the Reynolds number and Sc the Schmidt number. In contrast to Shalybkov & Rüdiger (2005) or Le Dizès & Riedinger (2010), the Froude number and Reynolds number are based on the angular velocity Ω_o of the outer cylinder since we shall consider the limiting case where the inner cylinder is at rest. For the same reason, it is convenient to use the inverse of the usual velocity ratio μ

$$\lambda = \frac{1}{\mu} = \frac{\Omega_i}{\Omega_o}. \tag{2.10}$$

3. Illustrative example of instability

Figure 1 displays one example of the frequency (figure 1a) and growth rate (figure 1b) when the inner cylinder is at rest $\lambda = 0$ ($\mu = \infty$), with the gap ratio $\eta = 0.8$, the azimuthal wavenumber $m = 14$, in a strongly stratified inviscid fluid: $F = 0.05$ and $Re = \infty$. Two families of branches can be easily identified in the frequency plot (figure 1a). In each family, there is an infinite number of branches which can be labelled by the number of oscillations of the radial eigenfunction (indicated for the first three branches of each family in figure 1a). As seen in figure 1(b), the growth rate is positive in the neighborhood of each crossing points of the frequency branches. The maximum growth rate is reached in the first band which corresponds to the crossing of the first branch of each family.

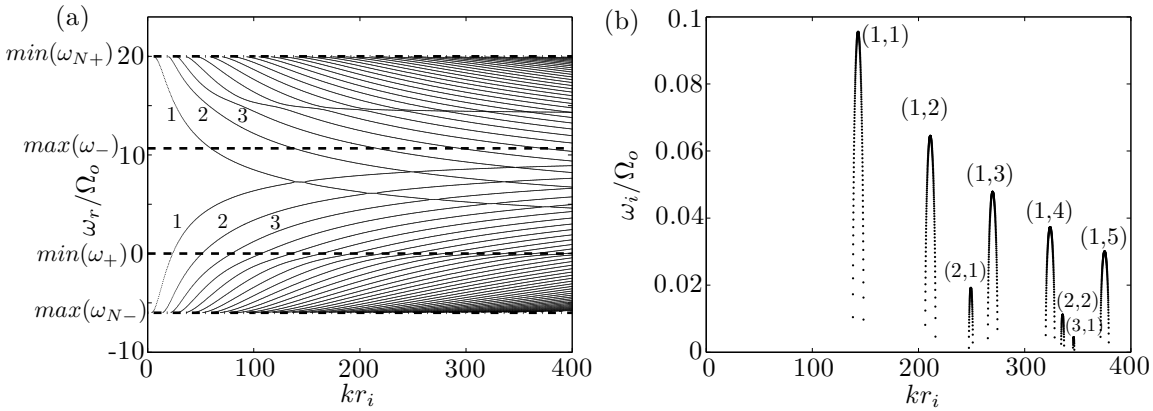

FIGURE 1. (a) Frequency ω_r and (b) growth rate ω_i as a function of the vertical wavenumber kr_i for $\lambda = 0$, $m = 14$, $\eta = 0.8$, $F = 0.05$ and $Re = \infty$. In (b), the labels (n_1, n_2) denote the branch number of the first (n_1) and the second family (n_2) indicated in (a).

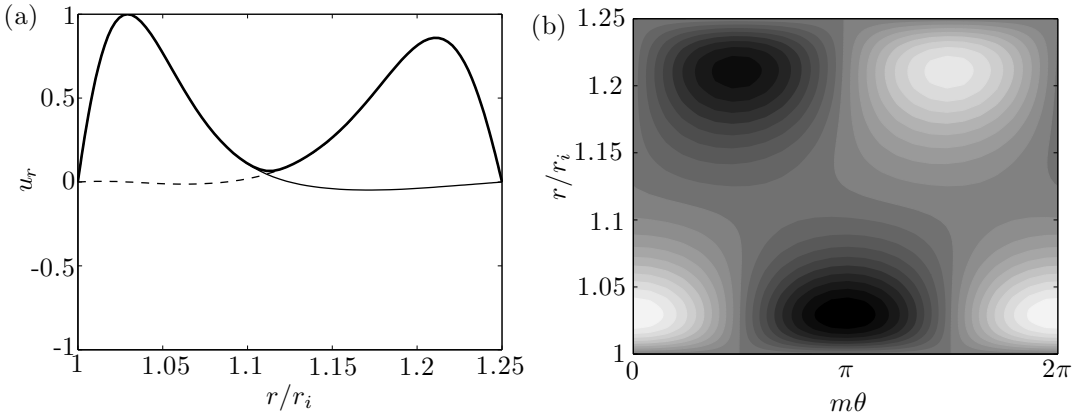

FIGURE 2. (a) Eigenfunction u_r in radial direction r for $\lambda = 0$, $m = 14$, $\eta = 0.8$, $F = 0.05$, $Re = \infty$ and $kr_i = 143$ corresponding to the maximum of the peak (1,1) in figure 1(b). The solid, dashed and thick solid lines are the real, imaginary and absolute parts, respectively. (b) Contour plot of the eigenfunction $Re[u_r(r)\exp(im\theta)]$ in the horizontal plane (r, θ) for the same parameters as in (a). The contour interval is 0.1.

Figure 2 displays the corresponding most unstable eigenmode. We can clearly identify two modes close to each cylinder with an azimuthal phase shift around $\pi/2$ (figure 2b). This structure is reminiscent of the SRI one that consists in two boundary trapped waves on each cylinder (Yavneh *et al.* 2001; Molemaker *et al.* 2001).

4. Asymptotics and instability mechanism

4.1. *The WKBJ approximation*

The instability observed in the previous section can be explained by means of a WKBJ analysis for large axial wavenumber k following Le Dizès & Billant (2009), Billant & Le Dizès (2009) and Le Dizès & Riedinger (2010). This will allow us to explain the instability mechanism and to obtain general necessary conditions for instability. For $k >> 1$, the solution of the inviscid equation (2.6) can be approximated by (Bender & Orszag 1978):

$$u_r = \frac{Q^{1/2}}{r^{1/2}\beta^{1/4}}\left[A_+ \exp\left(ik\int_{r_t}^{r}\sqrt{\beta(t)}dt\right) + A_- \exp\left(-ik\int_{r_t}^{r}\sqrt{\beta(t)}dt\right)\right], \qquad (4.1)$$

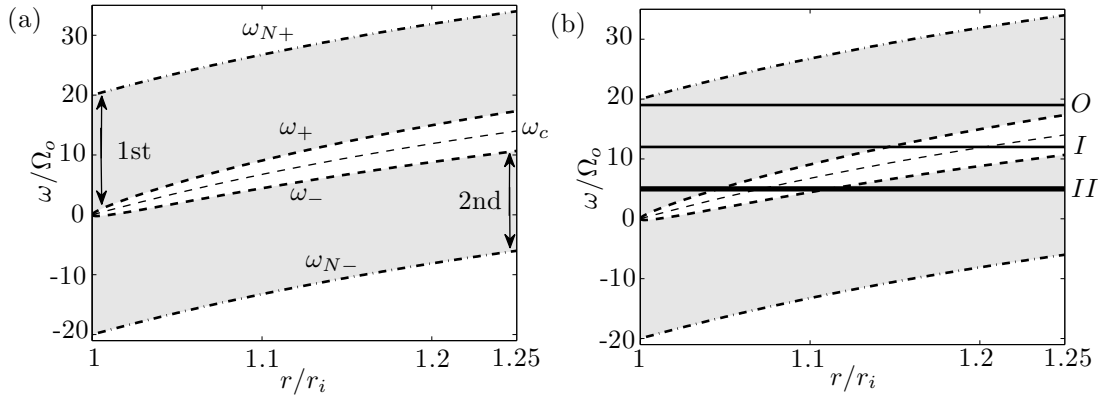

FIGURE 3. Sign of β for the same parameters as figure 1. The epicyclic frequencies $\omega_\pm$ and the critical frequencies $\omega_{N\pm}$ are plotted by thick dashed and thick dot-dashed lines, respectively. The critical frequency $\omega_c = m\Omega$ at which $s = 0$ is also plotted by dashed lines. The regions where the solutions are wavelike ($\beta > 0$) are shaded. The plot (b) is similar to (a) except that solid lines show examples of the frequency ω_r for which there is no turning point (O), one turning point (I) or two turning points (II).

where $A_\pm$ are constants,

$$\beta = \frac{s^2 - \phi}{N^2 - s^2}. \tag{4.2}$$

and r_t is a turning point where $\beta(r_t) = 0$. The WKBJ approximations are wavelike if β is real and positive while they have an exponential behaviour if $\beta < 0$.

Figure 3 shows the sign of β as a function of r and ω for the same parameters as figure 1. The sign of β^2 changes at characteristic frequencies called the epicyclic frequencies $\omega_\pm(r) = m\Omega \pm \sqrt{\phi}$ for which $s^2 = \phi$ (Le Dizès & Lacaze 2005), and the critical frequencies $\omega_{N\pm} = m\Omega \pm N$ for which $N^2 = s^2$. These characteristic frequencies generally increase with r since Ω increases with r when the outer cylinder rotates faster than the inner cylinder. Two distinct wave regions (shaded) can be seen in figure 3. Non-singular inertia-gravity waves can exist if their frequency lies in the interval $max(\omega_{N-}) < \omega < min(\omega_{N+})$. Just above and below this interval, waves can also exist but they are singular at the critical radius where $|s| = N$ so that they will be dampled by diffusive effects. When $\omega_r > max(\omega_{N+})$ or $\omega_r < min(\omega_{N-})$, the WKBJ approximations are exponential everywhere so that they can not satisfy the boundary conditions on both cylinders.

In figure 3(b), the horizontal solid lines show three different examples of frequency ω_r which can be categorized depending on the number of turning points r_t. The WKBJ approximations can be wavelike throughout the gap $r_i < r < r_o$ like for the frequency labelled O in figure 3(b) or can contain an evanescent region delimited by one or two turning points like for the examples of frequency labelled I and II, respectively. For each of these configurations, we can derive a dispersion relation by using classical connection formula at the turning points (Bender & Orszag 1978) and by imposing the boundary conditions at $r = r_i, r_o$. These analyses are performed in appendix B and we give here only the final results. For the case O (no turning point), the dispersion relation is simply

$$\exp\left(2ik\int_{r_i}^{r_o}\beta(t)dt\right) = 1, \quad \int_{r_i}^{r_o}\beta(t)dt = \frac{n\pi}{k}, \tag{4.3}$$

where n is a non-zero integer. For the case I, the WKBJ approximations are wavelike

between the inner cylinder r_i and a turning point r_{t1}. The dispersion relation is then

$$K(r_i, r_{t1}) = -\mathrm{i}\left[\frac{2 + \mathrm{i}X(r_{t1}, r_o)}{2 - \mathrm{i}X(r_{t1}, r_o)}\right], \tag{4.4}$$

where

$$K(r_a, r_b) = \exp\left(2\mathrm{i}k\int_{r_a}^{r_b}\sqrt{\beta(t)}dt\right), \quad X(r_a, r_b) = \exp\left(-2k\int_{r_a}^{r_b}\sqrt{-\beta(t)}dt\right). \tag{4.5}$$

Alternatively, there exists a configuration (labelled I') where the wave region is enclosed between a turning point r_{t2} and the outer cylinder r_o . This configuration is absent in figure 3 but it exists for other parameter values. The corresponding WKBJ dispersion relation is

$$K(r_{t2}, r_o) = -\mathrm{i}\left[\frac{2 + \mathrm{i}X(r_i, r_{t2})}{2 - \mathrm{i}X(r_i, r_{t2})}\right]. \tag{4.6}$$

Finally, in case II, the evanescent region is enclosed between two turning points r_{t1}, r_{t2} leading to

$$\left(K(r_i, r_{t1}) + \mathrm{i}\alpha\right)\left(K(r_{t2}, r_o) + \mathrm{i}\alpha\right) = (1 - \alpha^2)K(r_i, r_{t1})K(r_{t2}, r_o), \tag{4.7}$$

where $\alpha = \left(4 + X(r_{t1}, r_{t2})\right) / \left(4 - X(r_{t1}, r_{t2})\right)$. Note that these dispersion relations are valid only when the turning points are well-separated and sufficiently far from the boundaries.

The asymptotic dispersion relations (4.4) and (4.7) are compared to the numerical results in figure 4 which is otherwise the same as figure 1. We see that the asymptotic and numerical frequencies are always in excellent agreement. The locations of the growth rate peaks are also very well predicted, but their amplitudes tend to be over-estimated in the asymptotics. The growth rate is non-zero only in the configuration II, i.e. only when there exists a wave region attached to each cylinder and separated by an evanescent region.

The instability can be understood further from (4.7) by considering that the evanescent regions is large. In this limit, $X(r_{t1}, r_{t2})$ is very small so that α tends to unity. In the limit $\alpha = 1$, (4.7) reduces to

$$\left(K(r_i, r_{t1}) + \mathrm{i}\right)\left(K(r_{t2}, r_o) + \mathrm{i}\right) = 0. \tag{4.8}$$

Thus, the dispersion relation is satisfied either if

$$K(r_i, r_{t1}) = -\mathrm{i} \quad \text{or if} \quad K(r_{t2}, r_o) = -\mathrm{i}. \tag{4.9a, b}$$

These two relations correspond to the two distinct families of frequency branches in figure 1(a) and 4(a). (4.9a) and (4.9b) correspond to neutral waves attached to the inner cylinder and to the outer cylinder, respectively.

Since the instability occurs when two branches cross, we consider now a frequency ω_0 and a vertical wavenumeber k_0 where the two dispersion relations (4.9a,b) are satisfied simultaneously. We also consider the first order correction due to the small parameter $X(r_{t1}, r_{t2})$. Thus, the parameter α reads $\alpha = 1 + \epsilon^2/2 + \ldots$, where $\epsilon = \sqrt{X(r_{t1_0}, r_{t2_0})}$ and where quantities with a subscript 0 are evaluated with the leading order frequency ω_0 and wavenumber k_0. Similarly, the frequency ω and vertical wavenumber k can be expanded in the form

$$\omega = \omega_0 + \epsilon\omega_1 + \epsilon^2\omega_2 + \ldots, \tag{4.10a}$$

$$k = k_0 + \epsilon k_1 + \epsilon^2 k_2 + \ldots. \tag{4.10b}$$

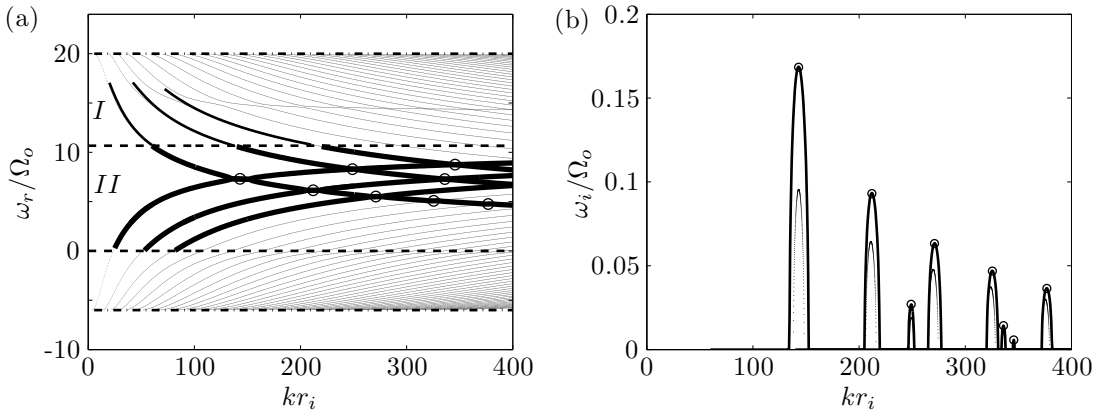

FIGURE 4. Same as figure 1 except that the asymptotic dispersion realtions (4.4) for the case I and (4.7) for the case II are also plotted by solid lines. The asymptotic maximum growth rate (4.14) is also shown with empty circles.

The dispersion relation (4.7) then reduces to (4.8) at leading order in ϵ. The order $O(\epsilon)$ is satisfied identically and at order $O(\epsilon^2)$, we have

$$[k_1 h(r_i, r_{t1_0}) + k_0\omega_1 h_\omega(r_i, r_{t1_0})]\,[k_1 h(r_{t2_0}, r_o) + k_0\omega_1 h_\omega(r_{t2_0}, r_o)] = \frac{1}{4}, \tag{4.11}$$

where

$$h(r_a, r_b) = \int_{r_a}^{r_b} \sqrt{\beta_0}dt, \quad h_\omega(r_a, r_b) = \int_{r_a}^{r_b} \frac{\partial\sqrt{\beta_0}}{\partial\omega}dt. \tag{4.12}$$

This gives ω_1 as

$$\omega_1 = -\frac{k_1}{2k_0}\left(\frac{h\,(r_i, r_{t1_0})}{h_\omega\,(r_i, r_{t1_0})} + \frac{h\,(r_{t2_0}, r_o)}{h_\omega\,(r_{t2_0}, r_o)}\right) \tag{4.13}$$
$$\pm\frac{1}{2k_0}\sqrt{\left(\frac{h\,(r_i, r_{t1_0})}{h_\omega\,(r_i, r_{t1_0})} - \frac{h\,(r_{t2_0}, r_o)}{h_\omega\,(r_{t2_0}, r_o)}\right)^2 k_1^2 + \frac{1}{h_\omega\,(r_i, r_{t1_0})\,h_\omega\,(r_{t2_0}, r_o)}}.$$

From (4.13), we see that a necessary and sufficient condition for instability (i.e. ω_1 imaginary) is that $h_\omega\,(r_i, r_{t1_0})\,h_\omega\,(r_{t2_0}, r_o) < 0$. In this case, the maximum growth rate is reached when $k_1 = 0$ and is

$$\omega_{i,max} = \mathrm{Im}(\epsilon\omega_1) = \frac{\sqrt{X(r_{t1_0}, r_{t2_0})}}{2k_0}\sqrt{\frac{-1}{h_\omega\,(r_i, r_{t1_0})\,h_\omega\,(r_{t2_0}, r_o)}}. \tag{4.14}$$

As seen by the symbols in figure 4(b), the growth rate (4.14) coincides almost exactly with the maximum of the peaks predicted by (4.7). In figure 5, a close-up view of the region around the resonance (1,1) between the first branches of each family is shown. We can clearly see that the resonance occurs when the frequency of the two families of waves (4.9a) and (4.9b) cross. The asymptotic frequency and growth rate from (4.13) are almost superposed to those from the asymptotic dispersion relation (4.7).

Therefore, a sufficient condition for instability is that $\frac{\partial\sqrt{\beta_0}}{\partial\omega}$ is of opposite sign in the intervals $[r_i, r_{t1_0}]$ and $[r_{t2_0}, r_o]$. As shown in Le Dizès & Billant (2009), the quantity $\frac{\partial\sqrt{\beta_0}}{\partial\omega}$ is related to the radial group velocity of the waves. The local radial wavenumber of the first term in the WKBJ approximation (4.1) is $l_r = k_0\sqrt{\beta_0}$ so that the group velocity is

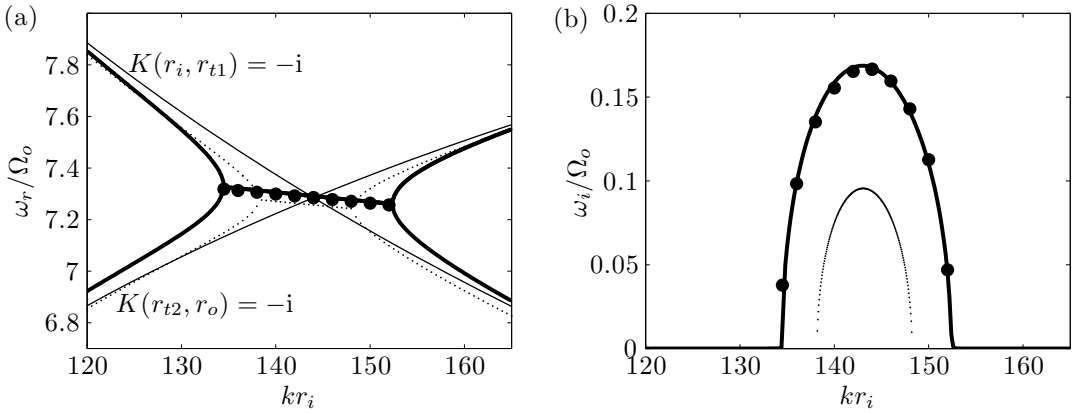

FIGURE 5. (a) Frequency and (b) growth rate as a function of the vertical wavenumber kr_i around the resonance (1,1) between the first branches of each family for the same parameters as in figure 4. Dotted and solid lines are numerical results and asymptotic results from (4.9), respectively. Thick solid lines show the asymptotic dispersion relation (4.7) and filled circles show (4.13).

indeed

$$v_g = \frac{\partial \omega}{\partial l_r} = 1/\left(k_0 \frac{\partial \sqrt{\beta_0}}{\partial \omega}\right). \tag{4.15}$$

Hence, the condition for instability is that the group velocity of the first WKBJ approximation in (4.1) is reversed between the two intervals $[r_i, r_{t1_0}]$ and $[r_{t2_0}, r_2]$. In other words, a wave propagating radially inward for $r < r_{t1_0}$ transforms to a wave propagating outward for $r > r_{t2_0}$ so that the evanescent region acts a wave source. Since $\partial\sqrt{\beta_0}/(\partial\omega) = s_0(\phi - N^2)/(\sqrt{\beta_0}\left(N^2 - s_0^2\right)^2)$, this requires that there exists a critical point r_c where $s_0(r_c) = 0$ between the two turning points r_{t1_0} and r_{t2_0}. As seen in figure 3, this is indeed the case since the critical frequency $\omega_c = m\Omega$ is enclosed between the epicyclic frequencies ω_-, ω_+. A similar instability condition has been derived by Le Dizès & Billant (2009) for the radiative instability.

The instability can be also explained in terms of over-reflection. When $max(\omega_{N-}) < \omega_r < min(\omega_{N+})$ and $N^2 > \phi$, the first WKBJ approximation in (4.1) corresponds for $r < r_{t1}$ to a wave propagating toward r_{t1} since its group velocity is positive because $s < 0$. Conversely, the second term of (4.1) corresponds to the reflected wave at r_{t1}. The reflection coefficient at r_{t1} is therefore $\mathcal{R}_1 = \left|A_-^2/A_+^2\right|$. Furthermore, the boundary condition at $r = r_i$ implies that

$$\mathcal{R}_1 = 1/\left|K^2(r_i, r_{t1})\right|. \tag{4.16}$$

For $r > r_{t2}$, the group velocity is reversed so that the reflection coefficient at r_{t2} is $\mathcal{R}_2 = \left|A_+^2/A_-^2\right|$ and, similarly, the boundary condition at $r = r_o$ implies

$$\mathcal{R}_2 = \left|K^2(r_{t2}, r_o)\right|. \tag{4.17}$$

The previous asymptotic analysis for $\alpha = 1 + \epsilon^2/2 + \ldots$ shows that when $k_1 = 0$,

$$K(r_i, r_{t1}) = K_0(r_i, r_{t1_0})\left[1 + 2\mathrm{i}k_0\epsilon\omega_1 h_\omega\left(r_i, r_{t1_0}\right) + O(\epsilon^2)\right], \tag{4.18a}$$

$$K(r_{t2}, r_o) = K_0(r_{t2_0}, r_o)\left[1 + 2\mathrm{i}k_0\epsilon\omega_1 h_\omega\left(r_{t2_0}, r_o\right) + O(\epsilon^2)\right]. \tag{4.18b}$$

Since $h_\omega\left(r_i, r_{t1_0}\right) > 0$, $h_\omega\left(r_{t2_0}, r_o\right) < 0$, and $|K_0(r_i, r_{t1_0})| = |K_0(r_{t2_0}, r_o)| = 1$, we see that $|K(r_i, r_{t1})|$ is lower than unity whereas $|K(r_{t2}, r_o)|$ is larger than unity. Hence, the

reflection coefficients $\mathcal{R}_1$ and $\mathcal{R}_2$ are both larger than unity meaning that incident waves are over-reflected at the turning points r_{t1} and r_{t2}.

In contrast, when there is a single turning point, the dispersion relations (4.4) and (4.6) imply that $|K(r_i, r_{t1})| = 1$ and $|K(r_{t2}, r_o)| = 1$. Therefore, there is no over-reflection explaining why the waves are neutral in this case.

4.2. *Frequency bands and instability conditions*

In the previous section, we have found that when the evanescent region is large, there exist two decoupled dispersion relations (4.9a,b). They can be rewritten

$$\int_{r_i}^{r_{t1}} \sqrt{\beta(t)}dt = \left(n - \frac{1}{4}\right)\frac{\pi}{k}, \tag{4.19a}$$

$$\int_{r_{t2}}^{r_o} \sqrt{\beta(t)}dt = \left(n - \frac{1}{4}\right)\frac{\pi}{k}, \tag{4.19b}$$

where n is a non-negative integer. These relations are valid as long as there exists at least one turning point. In the absence of turning point, the dispersion relation (4.3) should be used.

The two dispersion relations (4.19) show clearly that there exist two independent families of waves: one trapped between the inner cylinder r_i and $min(r_{t1}, r_o)$ and the other trapped between $min(r_{t2}, r_i)$ and the outer cylinder r_o. As seen in figure 3(a), the first family can exist in the frequency interval

$$min(\omega_+) < \omega < min(\omega_{N+}), \tag{4.20}$$

while the second can exist if the frequency lies in the range

$$max(\omega_{N-}) < \omega < max(\omega_-). \tag{4.21}$$

These two distinct frequency bands correspond exactly to those of the two branch families in figure 1(a). The frequency of the first family starts from $\omega = min(\omega_{N+})$ and decreases to $\omega = min(\omega_+)$ as k increases, whereas the frequency of the second family increases from $\omega = max(\omega_{N-})$ to $\omega = max(\omega_-)$ as k increases.

The main conditions for instability can be derived from the frequency ranges (4.20)-(4.21). First, the conditions of existence of the two wave families: $max(\omega_{N-}) < max(\omega_-)$ and $min(\omega_+) < min(\omega_{N+})$ imply

$$F < \frac{1}{2}\sqrt{\frac{1-\eta^2}{1-\lambda\eta^2}}. \tag{4.22}$$

Therefore, the fluid should be strongly stratified: the critical Froude number is always less than 1/2 for $0 \leqslant \lambda < 1$. The condition (4.22) only applies when $\lambda < 1$. The critical Froude number when $\lambda \geqslant 1$ is derived in appendix A.

Since the instability requires that the branches cross, a second condition is that the two frequency bands (4.20) and (4.21) share a common interval. This requires that $max(\omega_-) > min(\omega_+)$ and $min(\omega_{N+}) > max(\omega_{N-})$, leading to the following conditions for instability:

$$\frac{2}{|1-\sqrt{\lambda}|}\sqrt{\frac{1-\lambda\eta^2}{1-\eta^2}} < m < \frac{2}{F|1-\lambda|}. \tag{4.23}$$

Note that these inequalities also apply when $\lambda > 1$ as discussed in appendix A. This relation shows that only a finite band of azimuthal wavenumbers m are able to satisfy

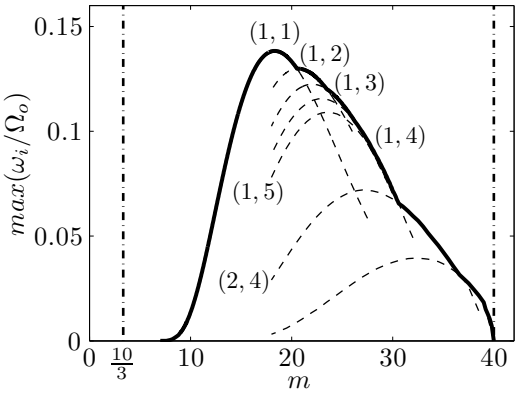

FIGURE 6. Maximum growth rate (bold line) as a function of the azimuthal wavenumber m for $\lambda = 0$, $\eta = 0.8$, $F = 0.05$ and $Re = \infty$. Dashed lines represent the maximum growth rates of the resonance (n_1, n_2) where n_1 and n_2 are the branch number of each family (see figure 1a). Bold dot-dashed lines indicate bounds given by (4.23).

the resonance condition: for example, for the parameters of figure 1, (4.23) gives $10/3 < m < 40$.

Numerical results shown in figure 6 confirm that the maximum growth rate is positive only when m belongs to this interval. The upper azimuthal wavenumber cut-off corresponds exactly to the upper bound predicted by (4.23). The lower cut-off seems around $m \approx 8$, i.e. higher than the lower bound of (4.23). However, the growth rate is exponentially small but non-zero for the azimuthal wavenumbers $4 < m < 8$ because the evanescent region is very large. The growth rate curve reaches a maximum for $m \approx 18$ and exhibits a broken shape because the dominant resonance is not always between the first branch of each family (1,1) but can involve the following branches as indicated in figure 6. The lower bound in (4.23) is always larger than $m = 2$ for $0 \leqslant \lambda < 1$ and increases to infinity as λ tends to unity. The unstable azimuthal wavenumbers are therefore typically larger than for $1 < \lambda < 1/\eta^2$ since the lower bound of (4.23) goes to zero when $\lambda \to 1/\eta^2$ (Yavneh *et al.* 2001; Molemaker *et al.* 2001; Le Dizès & Riedinger 2010).

5. Parametric study

We now study numerically the maximum growth rate of the instability as a function of the main parameters: F, η, Re and λ in the range $0 \leqslant \lambda < 1$.

5.1. *Effect of the Froude number F*

Figure 7(a) shows the maximum growth rate as a function of the azimuthal wavenumber m for $\eta = 0.8$, $\lambda = 0$ and $Re = \infty$ for different Froude numbers. The band of unstable azimuthal wavenumbers widens toward large azimuthal wavenumbers when the Froude number decreases. The upper azimuthal wavenumber cut-off agrees well with the upper bound predicted by (4.23). The lower azimuthal wavenumber cut-off does not vary with the Froude number in agreement with (4.23). The maximum growth rate and most amplified azimuthal wavenumber are almost constant and equal to $max(\omega_i/\Omega_o) \approx 0.14$ and $m_{max} \approx 18$ when $F \lesssim 0.05$ whereas they strongly decreases when F is increased above 0.1 because the upper azimuthal wavenumber cut-off is then lower or comparable to $m_{max} = 18$. The evolution of the maximum growth rate as a function of F is summarized in figure 7(b). The maximum growth rate seems to go to zero around the Froude number $F \approx 0.2$ which is smaller than the critical Froude number $F_c = 0.3$ predicted by

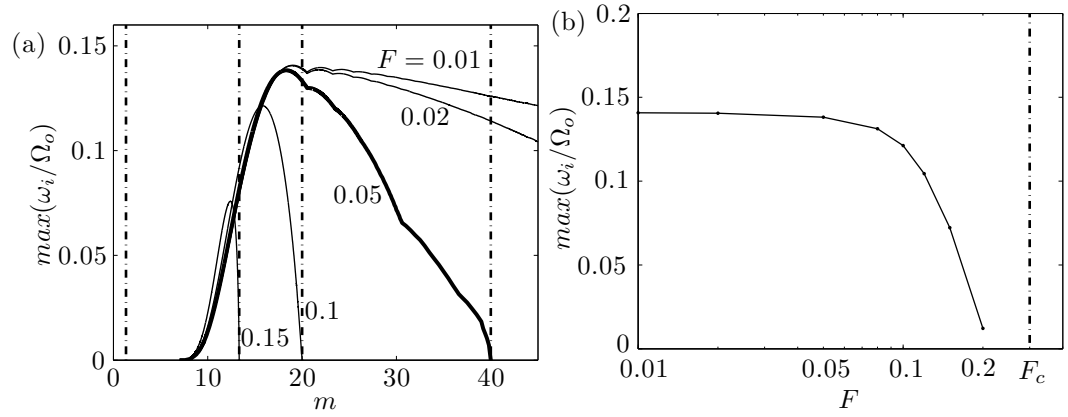

FIGURE 7. (a) Maximum inviscid growth rate as a function of the azimuthal wavenumber m for different Froude numbers $F = [0.01, 0.02, 0.05, 0.1, 0.15]$ for $\lambda = 0$ and $\eta = 0.8$. The dashed dotted lines represent the bound given by (4.23). (b) Maximum growth rate as a function of the Froude number F for $\eta = 0.8$ and $\lambda = 0$. The critical Froude number F_c given by (4.22) is shown by a dashed dotted line.

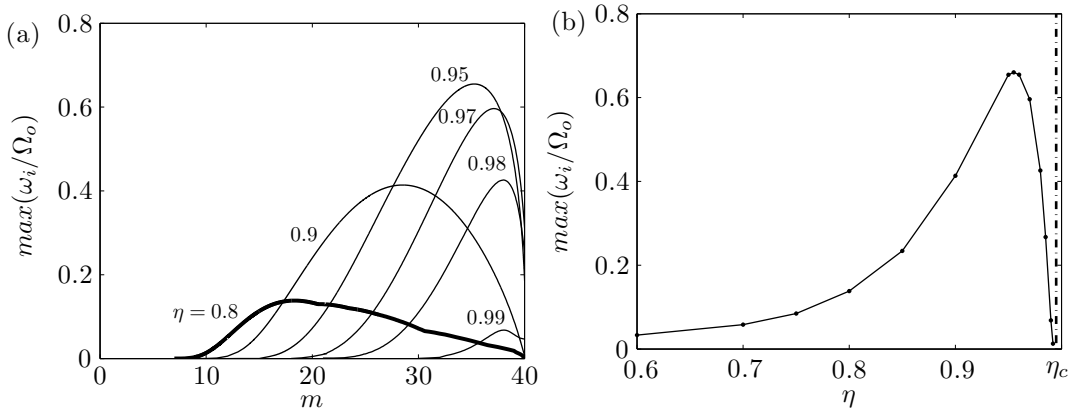

FIGURE 8. (a) Maximum inviscid growth rate as a function of the azimuthal wavenumber m for different gap ratios $\eta = [0.8, 0.9, 0.95, 0.97, 0.98, 0.99]$ for $F = 0.05$ and $\lambda = 0$. (b) Maximum growth rate as a function of the gap ratio η for $F = 0.05$ and $\lambda = 0$. The critical gap ratio η_c is shown by a dashed dotted line.

(4.22). However, the growth rate is likely to be very small but non-zero for $0.2 \lesssim F \leqslant F_c$ because the evanescent region is very large.

5.2. *Effect of the gap ratio η*

Figure 8(a) shows the maximum growth rate as a function of the azimuthal wavenumber for $F = 0.05$, $\lambda = 0$ and $Re = \infty$ for different gap ratios η. When η increases, the band of unstable azimuthal wavenumbers shrinks because the lower cut-off increases whereas the upper cut-off remains constant in agreement with (4.23). Nevertheless, we can notice that the growth rate is not always strictly zero at the upper cut-off $m_c = 40$. This is because this critical azimuthal wavenumber corresponds only to the limit above which the modes have a singularity at the critical point r_N where $|s(r_N)| = N$. The modes thereby start to be damped for $m > m_c$ but if the destabilizing effect due to the resonance is stronger than this damping, the growth rate can remain positive for $m > m_c$. In practice, however, we see that the growth rate decays abruptly near $m = m_c$ and should vanish only slightly above m_c. The maximum growth rate first increases with η but after $\eta > 0.95$ it decreases abruptly. Figure 8(b) summarizes the evolution of the maximum growth rate as a function

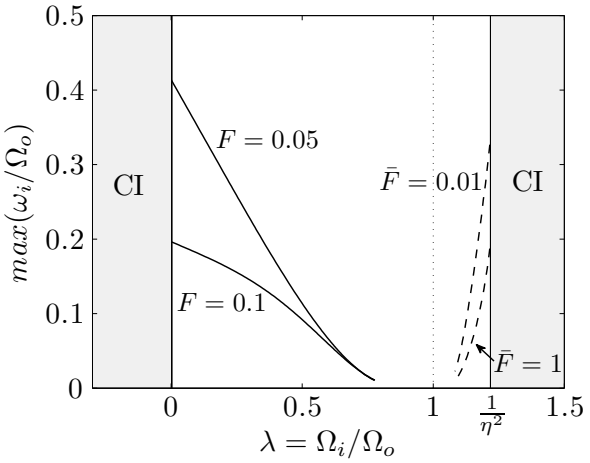

FIGURE 9. Maximum inviscid growth rates of the SRI as a function of $\lambda = 1/\mu = \Omega_i/\Omega_o$ for the Froude numbers $F = 0.05, 0.1$ and for $\eta = 0.9$ (solid lines). Dashed lines show the results of the figure 1 of Molemaker *et al.* (2001) for $\eta = 0.9048$ and the Froude numbers $\bar{F} = 0.01, 1$. Note that the Froude number $\bar{F}$ defined by Molemaker *et al.* (2001) is based on the angular velocity $\bar{\Omega}$ at the middle point $\bar{r} = (r_o + r_i)/2$ and is thus slightly different from the present definition. The regimes of the centrifugal instability (CI) are shaded. The dotted line indicates the limit of solid body rotation $\lambda = 1$.

of the gap ratio η for the same parameters as in (a). The overall maximum growth rate is reached around $\eta_{max} \approx 0.955$. Then, the maximum growth rate goes abruptly to zero for $\eta = \eta_c = \sqrt{(1 - 4F^2)/(1 - 4\lambda F^2)} = 0.995$ as predicted by (4.22).

5.3. *Effect of the angular velocity ratio* λ

Figure 9 shows the maximum growth rate as a function of $\lambda = 1/\mu$ for two different values of F for $\eta = 0.9$. In the range investigated in this paper ($0 < \lambda < 1$), the growth rate is maximum when the inner cylinder is at rest ($\lambda = 0$), and decreases to zero as λ increases to unity. The domain of the other instabilities are also indicated in figure 9. The intervals $\lambda < 0$ and $\lambda > 1/\eta^2$ correspond to the domain of the centrifugal instability. The interval $1 < \lambda < 1/\eta^2$ is the domain of the SRI previously found by Molemaker *et al.* (2001) and Yavneh *et al.* (2001). The growth rate obtained by Molemaker *et al.* (2001) for this regime is also plotted with dashed lines. It is maximum for $\lambda = 1/\eta^2$ and decreases to zero as λ decreases to unity. The growth rate values scaled by the angular velocity of the outer cylinder Ω_o are comparable to those for $0 < \lambda < 1$. Taken all together, we can conclude that the range of instability of the stably stratified Taylor-Couette flow is much wider than previously identified: the growth rate is always positive except in the limit of solid body rotation ($\lambda = 1$). However, it should be noted that the maximum growth rate becomes very small in the neighborhood of $\lambda = 1$.

These results are actually very similar to those for the radiative instability of a columnar vortex in a stratified rotating fluid (Park & Billant 2012*a*,*b*). In the latter case, the radiative instability exists when the Rossby number is $Ro \geqslant -1$ and its growth rate is maximum at both ends of this interval, i.e. for $Ro = -1$ and $Ro = +\infty$, and vanishes in the limit $Ro \to 0$. From the relation (1.2), we see that these three particular values of Ro correspond exactly to those found above for the strato-rotational instability of the stratified Taylor-Couette flow: $\lambda = 0$, $\lambda = 1/\eta^2$ for the growth rate maxima and $\lambda = 1$ for the minimum. Thus, even if the boundary conditions are completely different between the two flows, there is a close correspondance between them and their associated instabilities.

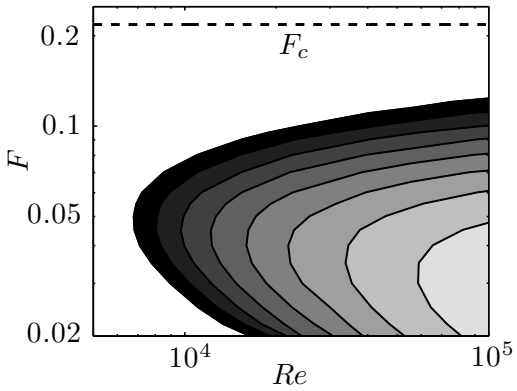

FIGURE 10. Neutral stability curve with contours of maximum growth rate $max(\omega_i/\Omega_o)$ as a function of the Reynolds number Re and Froude number F for $\eta = 0.9$, $\lambda = 0$ and $Sc = 700$. The unstable domain is shaded and the contour interval is 0.05. The dashed line represents the critical Froude number $F_c = 0.218$ given by (4.22).

5.4. *Viscous effect*

Finally, we have investigated the viscous and diffusive effects for one set of parameters: $\lambda = 0$, $\eta = 0.9$, and the Schmidt number $Sc = \nu/D = 700$, where ν is the viscosity and D the diffusivity. This value of the Schmidt number corresponds to the one of salt stratified water generally used in laboratory experiments. Figure 10 shows the maximum growth rate as a function of the Reynolds number $Re = \Omega_o r_o(r_o - r_i)/\nu$ and the Froude number F. The critical Reynolds number Re_c is about $Re_c \approx 7000$ at $F \approx 0.05$. This value of Re_c is higher than the values found for $1 < \lambda < 1/\eta^2$ (Yavneh *et al.* 2001; Le Bars & Le Gal 2007; Shalybkov & Rüdiger 2005) because the associated vertical and azimuthal wavenumbers are larger for $0 \leqslant \lambda < 1$ than for $1 < \lambda < 1/\eta^2$.

6. Conclusion and discussion

In conclusion, we have discovered that the stratified Taylor-Couette flow is also unstable when the outer cylinder rotates faster than the inner cylinder $d\Omega^2/dr > 0$ ($\lambda = 1/\mu = \Omega_i/\Omega_o < 1$). Hence, the sufficient condition for inviscid instability $d\Omega^2/dr < 0$ proposed by Yavneh *et al.* (2001) and Molemaker *et al.* (2001) is extended in an unprecedented manner to $d\Omega^2/dr \neq 0$. The instability mechanism involves the resonance of two families of inertia-gravity waves like for the Strato-Rotational Instability (Yavneh *et al.* 2001; Molemaker *et al.* 2001; Le Dizès & Riedinger 2010). A WKBJ analysis in the inviscid limit shows that this new instability exists only in a given band of relatively large azimuthal wavenumbers and only if the fluid is strongly stratified. The theoretical WKBJ predictions are in very good agreement with the numerical results. The growth rate is independent of the stratification if the Froude number is sufficiently small. In contrast, it depends strongly on the gap ratio and is maximum for a value of η close to unity. The growth rate reaches its maximum when the inner cylinder is at rest $\lambda = 0$ ($\mu = \infty$), and its value is comparable to the one previously computed for $1 < \lambda < 1/\eta^2$ (Yavneh *et al.* 2001; Molemaker *et al.* 2001; Le Dizès & Riedinger 2010). However, the critical Reynolds number for $\lambda < 1$ is typically larger than that for $1 < \lambda < 1/\eta^2$ implying that experimental tests might require set-ups with large diameters in order to have low Froude and high Reynolds numbers at the same time. These conditions are however largely fulfilled in geophysical and astrophysical flows and our study indicates that the Strato-Rotational Instability can operate in a very large variety of conditions. In particular, the new regime of instability is closely related to anticyclonic geophysical vortices

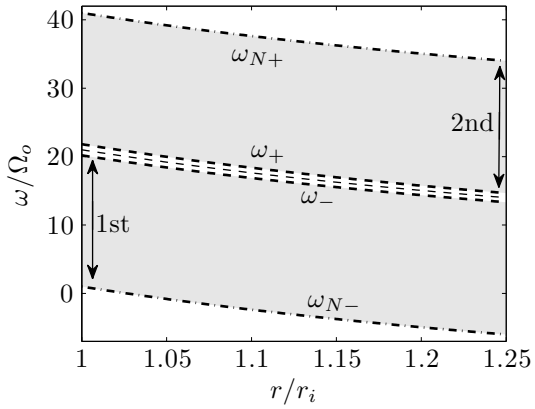

FIGURE 11. Similar to figure 3 except that $\lambda = 1.5$.

in the centrifugally stable regime that are frequently observed in the oceans (Ménesguen *et al.* 2009) and recently shown to be unstable to the radiative instability (Park & Billant 2012*a*).

Appendix A. Conditions for instability in the regime $1 < \lambda < 1/\eta^2$

In this appendix, we derive stability conditions equivalent to (4.22) and (4.23) but in the regime $1 < \lambda < 1/\eta^2$ investigated by Yavneh *et al.* (2001), Molemaker *et al.* (2001) and Le Dizès & Riedinger (2010). The difference with the case $\lambda < 1$ is that the epicyclic and critical frequencies ($\omega_\pm$ and $\omega_{N\pm}$) decrease with r (figure 11). As before, non-singular inertia-gravity waves exist in the two frequency intervals:

$$max(\omega_{N-}) < \omega < max(\omega_-), \tag{A 1a}$$

$$min(\omega_+) < \omega < min(\omega_{N+}), \tag{A 1b}$$

but now the condition of existence of two family of waves is

$$F_i < \frac{1}{2}\sqrt{\frac{\lambda(1-\eta^2)}{1-\lambda\eta^2}}, \tag{A 2}$$

where $F_i = \Omega_i/N = \lambda F$ is the Froude number based on the angular velocity of the inner cylinder. In contrast to the regime $\lambda < 1$, the critical Froude number $F_{i,c}$ is always larger than $1/2$ for $1 < \lambda < 1/\eta^2$ and even goes to infinity as $\lambda \to 1/\eta^2$s o that the instability exists for weaker stratification than in the regime $\lambda < 1$. The band of unstable azimuthal wavenumber remains the same as (4.23). In this case, the lower cut-off goes to zero when $\lambda \to 1/\eta^2$.

Appendix B. Turning point analysis

In this appendix, we perform an analysis which connects the WKBJ approximations of each different regions across the turning points. There exists at most two turning points r_{t1} and r_{t2} with $r_{t1} < r_{t2}$ enclosing an evanescent region $r_{t1} < r < r_{t2}$ (See §4.1). We assume that the two turning points are well separated from each other and from the cylinders $r = r_i, r_o$.

In the first wave region $r_i < r < r_{t1}$, the WKBJ approximation reads

$$u_r = \frac{Q^{1/2}}{r^{1/2}\beta^{1/4}}\left[A_+ \exp\left(ik\int_{r_{t1}}^{r}\sqrt{\beta(t)}dt\right) + A_- \exp\left(-ik\int_{r_{t1}}^{r}\sqrt{\beta(t)}dt\right)\right], \tag{B 1}$$

where A_+ and A_- are constants. As shown in §4.1, the group velocity (4.15) of the first term of (B 1) is positive so that it corresponds to an incident wave toward the turning point r_{t1} Conversely, the second term corresponds to a reflected wave from r_{t1}. Around the turning point r_{t1} where the WKBJ approximation (B 1) is no longer valid, (2.6) approximates at leading order to

$$\frac{\mathrm{d}^2 u_r}{\mathrm{d}\tilde{r}^2} - \tilde{r} u_r = O(\epsilon), \tag{B 2}$$

where $\tilde{r} = (r - r_{t1})/\epsilon$, $\epsilon = 1/\left(\beta'(r_{t1})k^2\right)^{1/3}$. The solution of (B 2) is $u_r = a_1 \mathrm{Ai}(\tilde{r}) + b_1 \mathrm{Bi}(\tilde{r})$ where a_1 and b_1 are constants and Ai and Bi denote the Airy functions. From the asymptotic behaviours of the Airy functions for $\tilde{r} \to -\infty$ and $\tilde{r} \to +\infty$, we obtain the matching WKBJ approximation for $r > r_{t1}$ as follows:

$$u_r = \frac{Q^{1/2}\mathrm{e}^{-\mathrm{i}\pi/4}}{r^{1/2}(-\beta)^{1/4}} \left[B_+ \exp\left(-k \int_{r_{t1}}^{r} \sqrt{-\beta(t)} dt \right) + B_- \exp\left(k \int_{r_{t1}}^{r} \sqrt{-\beta(t)} dt \right) \right], \tag{B 3}$$

where $B_+ = (A_+ + \mathrm{i}A_-)/2$ and $B_- = \mathrm{i}A_+ + A_-$. In the configuration I, the second turning point r_{t2} does not exist and the asymptotic dispersion relation (4.4) is obtained by imposing the boundary conditions $u_r = 0$ at $r = r_i, r_o$ in the approximations (B 1) and (B 3). When the turning point $r = r_{t2}$ is present, (B 3) is again not valid in its neighborhood but a local equation similar to (B 2) can be derived. Its solution is $u_r = c_1 \mathrm{Ai}(-\tilde{r}) + d_1 \mathrm{Bi}(-\tilde{r})$ where c_1 and d_1 are constants. From the asymptotic behaviours of these Airy functions, we obtain the WKBJ approximation for $r > r_{t2}$

$$u_r = \frac{Q^{1/2}}{r^{1/2}\beta^{1/4}} \left[C_+ \exp\left(ik \int_{r_{t2}}^{r} \sqrt{\beta(t)} dt \right) + C_- \exp\left(-ik \int_{r_{t2}}^{r} \sqrt{\beta(t)} dt \right) \right], \tag{B 4}$$

where $C_+ = (Y^2/2)B_+ - (\mathrm{i}/Y^2)B_-$, $C_- = B_-/Y^2 - (\mathrm{i}Y^2/2)B_+$ and $Y = X(r_{t1}, r_{t2})$ where X is defined in (4.5). As explained in §4.1, the first term of (B 4) has now a negative group velocity and so corresponds to an incident wave toward the turning point r_{t2} whereas the second term corresponds to a reflected wave. C_+ and C_- can be also expressed in terms of A_+ and A_- as

$$C_+ = \left(\frac{Y^2}{4} + \frac{1}{Y^2} \right) A_+ + \mathrm{i} \left(\frac{Y^2}{4} - \frac{1}{Y^2} \right) A_-, \;\; C_- = \mathrm{i} \left(\frac{Y^2}{4} - \frac{1}{Y^2} \right) A_+ + \left(\frac{Y^2}{4} + \frac{1}{Y^2} \right) A_-. \tag{B 5}$$

By imposing the boundary conditions in the approximations (B 1) and (B 4), (B 5) leads to the asymptotic dispersion relation (4.7) for the unstable case II. When the turning point r_{t1} does not exist (configuration I'), the asymptotic dispersion relation (4.6) is obtained by imposing the boundary conditions $u_r = 0$ in the approximations (B 4) and (B 3) in which r_{t1} is replaced by r_i.

REFERENCES

Andereck, C. D., Liu, S. S. & Swinney, H. L. 1986 Flow regimes in a circular Couette system with independently rotating cylinders. *J. Fluid Mech.* **164**, 155–183.

Antkowiak, A. & Brancher, P. 2004 Transient energy growth for the Lamb-Oseen vortex. *Phys. Fluids* **16**, L1–L4.

Bender, C. M. & Orszag, S. A. 1978 *Advanced Mathematical Methods for Scientists and Engineers*. New York: McGraw-Hill.

Billant, P. & Gallaire, F. 2005 Generalized Rayleigh criterion for non-axisymmetric centrifugal instabilities. *J. Fluid Mech.* **542**, 365–379.

Billant, P. & Le Dizès, S. 2009 Waves on a columnar vortex in a strongly stratified fluid. *Phys. Fluids* **21**, 106602.

Boubnov, B. M., Gledzer, E. B. & Hopfinger, E. J. 1995 Stratified circular Couette flow: instability and flow regimes. *J. Fluid Mech.* **292**, 333–358.

Caton, F., Janiaud, B. & Hopfinger, E. J. 2000 Stability and bifurcations in stratified Taylor-Couette flow. *J. Fluid Mech.* **419**, 93–124.

Dubrulle, B., Dauchot, O., Daviaud, F., Longaretti, P.-Y., Richard, D. & Zahn, J.-P. 2005*a* Stability and turbulent transport in Taylor-Couette flow from analysis of experimental data. *Phys. Fluids* **17**, 095103.

Dubrulle, B., Marié, L., Normand, Ch., Richard, D., Hersant, F. & Zahn, J. P. 2005*b* An hydrodynamic shear instability in stratified disks. *Astron. Astroph.* **429**, 1–13.

Fabre, D. & Jacquin, L. 2004 Viscous instabilities in trailing vortices at large swirl numbers. *J. Fluid. Mech.* **500**, 239–262.

Hua, B. L., Le Gentil, S. & Orlandi, P. 1997*a* First transitions in circular Couette flow with axial stratification. *Phys. Fluids* **9**, 365.

Hua, B. L., Moore, D. W. & Le Gentil, S. 1997*b* Inertial nonlinear equilibration of equatorial flows. *J. Fluid Mech.* **331**, 345–371.

Le Bars, M. & Le Gal, P. 2007 Experimental Analysis of the Stratorotational Instability in a Cylindrical Couette Flow. *Phys. Rev. Lett.* **99**, 064502.

Le Dizès, S. & Billant, P. 2009 Radiative instability in stratified vortices. *Phys. Fluids* **21**, 096602.

Le Dizès, S. & Lacaze, L. 2005 An asymptotic description of vortex Kelvin modes. *J. Fluid Mech.* **542**, 69–96.

Le Dizès, S. & Riedinger, X. 2010 The strato-rotational instability of Taylor-Couette and Keplerian flows. *J. Fluid Mech.* **660**, 147–161.

Ménesguen, C., Hua, B. L., Papenberg, C., Klaeschen, D., Géli, L. & Hobbs, R. 2009 Effect of bandwidth on seismic imaging of rotating stratified turbulence surrounding an anticyclonic eddy from field data and numerical simulations. *Geophys. Res. Lett.* **36**, L00D05.

Molemaker, M. J., McWilliams, J. C. & Yavneh, I. 2001 Instability and Equilibrium of Centrifugally Stable Stratified Taylor-Couette Flow. *Phys. Rev. Lett.* **86**, 5270.

Ooyama, K. 1966 On the Stability of the Baroclinic Circular Vortex : a Sufficient Criterion for Instability. *J. Atmos. Sci.* **23**, 43–53.

Park, J. 2012 Waves and instabilities on vortices in stratified and rotating fluids. PhD thesis, Ecole Polytechnique.

Park, J. & Billant, P. 2012*a* Radiative instability of an anticyclonic vortex in a stratified rotating fluid. *J. Fluid Mech.* **707**, 381–392.

Park, J. & Billant, P. 2012*b* Waves on a columnar vortex in a strongly-stratified and rotating fluid. *to be submitted to Phys. Fluids* .

Riedinger, X., Le Dizès, S. & Meunier, P. 2011 Radiative instability of the flow around a rotating cylinder in a stratified fluid. *J. Fluid Mech.* **672**, 130–146.

Riedinger, X., Meunier, P. & Le Dizès, S. 2010 Instability of a vertical columnar vortex in a stratified fluid. *Exp. Fluids* **49**, 673–681.

Schecter, D. A. & Montgomery, M. T. 2004 Damping and pumping of a vortex Rossby wave in a monotonic cyclone: Critical layer stirring versus inertia-buoyancy wave emission. *Phys. Fluids* **26** (5), 1334.

Shalybkov, D. & Rüdiger, G. 2005 Stability of density-stratified viscous Taylor-Couette flows. *Astron. Astroph.* **438**, 411–417.

Vanneste, J. & Yavneh, I. 2007 Unbalanced instabilities of rapidly rotating stratified shear flows. *J. Fluid Mech.* **584**, 373–396.

Withjack, E. M. & Chen, C. F. 1974 An experimental study of Couette instability of stratified fluids. *J. Fluid Mech.* **66**, 725–737.

Yavneh, I., McWilliams, J. C. & Molemaker, M. J. 2001 Non-axisymmetric instability of centrifugally stable staratified Taylor-Couette flow. *J. Fluid Mech.* **448**, 1–21.

2.3 Limit $\eta = 0$: transition from the stratorotational instability to the radiative instability

In this section, we consider the limit of the Taylor-Couette flow when the outer cylinder is located at infinity ($\eta = 0$). Since we consider that the angular velocity of the outer cylinder is non-zero and larger than the one of the inner cylinder ($\lambda < 1$), this limit $\eta = 0$ is rather unrealistic. However, such flow can be also regarded as the flow around a cylinder rotating at rate $\Omega_i - \Omega_o$ in a fluid rotating at rate Ω_o. We assume that the fluid is strongly stratified (hydrostatic approximation) and inviscid so that the equations (2.24) and (2.25) in chapter 2 expressed with $\tilde{k} = kF$ are used The shooting method is used to integrate these equations. We apply the boundary condition such that the perturbations vanish or correspond to an outgoing wave as $r \to \infty$. For example, the solution for the pressure is for $r >> R_i$

$$p(r) \sim H_m^{(2)}\left(\tilde{k}r\sqrt{-\Delta_\infty}\right), \tag{4.2}$$

where $H_m^{(2)}$ is the Hankel function of the second kind of order m and $\Delta_\infty = \Delta(r \to \infty)$. We select the second kind of the Hankel function $H_m^{(2)}$ since it has a positive group velocity in the regime $\mu > 1$. Note that for $\Delta_\infty > 0$, (4.2) transforms to an exponentially decaying solution.

2.3.1. Effect of the azimuthal wavenumber m

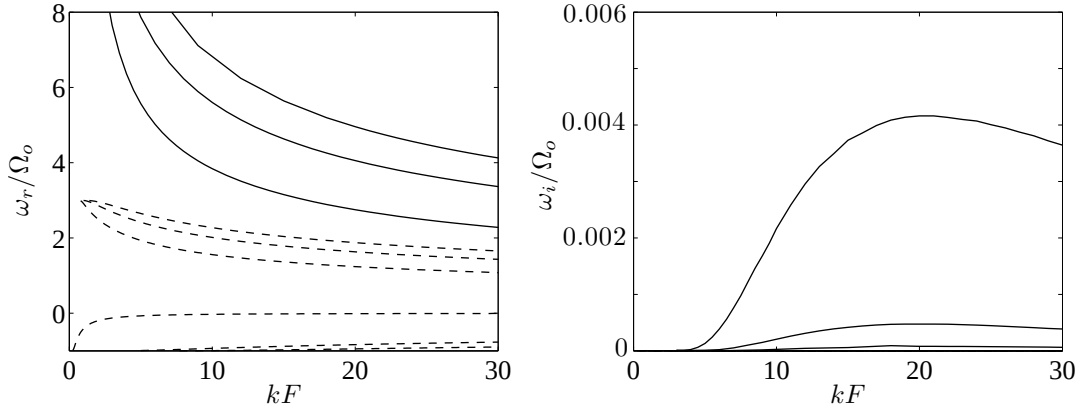

Figure 4.2: (a) Frequency and (b) growth rate as a function of the rescaled vertical wavenumber kF for $\lambda = 0$ and $\eta = 0$ for $m = 1$ (dashed lines) and $m = 15$ (solid lines).

Figure 4.2 shows the frequency and growth rate of the first three branches as a function of the rescaled vertical wavenumber kF for $m = 1$ (dashed lines) and $m = 15$ (solid lines) for $\lambda = 0$ and $\eta = 0$. These two azimuthal wavenumbers are typical examples of the two different behaviours that can be encountered as m varies. There are an infinite number of branches which differ by the number of oscillations near the inner cylinder $r = R_i$. For both azimuthal wavenumbers, there is a family of branches for which the frequency decreases as k increases and tends to $\omega_r = min(\omega_+) = m\lambda + 2\sqrt{\lambda}$ as $k \to \infty$. For $m = 1$, there is also another family of branches where the frequency increases with k and tends to $\omega_r = max(\omega_-) = \sqrt{\lambda}(\sqrt{\lambda} + 2)$ as $k \to \infty$. In figure 4.2(b), we clearly see that the growth rate is positive for $m = 15$ while it is zero for $m = 1$. This agrees with the predictions of the previous section on the band of unstable azimuthal wavenumbers which reduces for $\eta = 0$ and $F = 0$ to $m > 2/|1 - \sqrt{\lambda}|$.

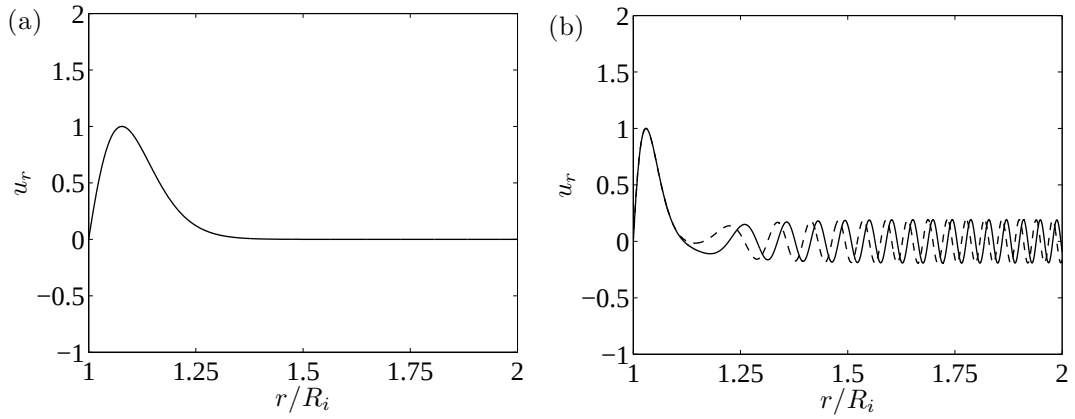

Figure 4.3: Eigenfunction $u_r(r)$ for $k = 20$, $\lambda = 0$ and $\eta = 0$ for (a) $m = 1$ and (b) $m = 15$. The solid and dashed lines are the real and imaginary parts, respectively.

Figure 4.3 shows examples of the radial velocity eigenfunction $u_r(r)$ for the first branch for $k = 20$, $\lambda = 0$ and $\eta = 0$ for (a) $m = 1$ and (b) $m = 15$. We clearly see that for $m = 1$, there is no wave but the solution decays exponentially (figure 4.3a) while there exists a radiating inertia-gravity wave train for $m = 15$ (figure 4.3b).

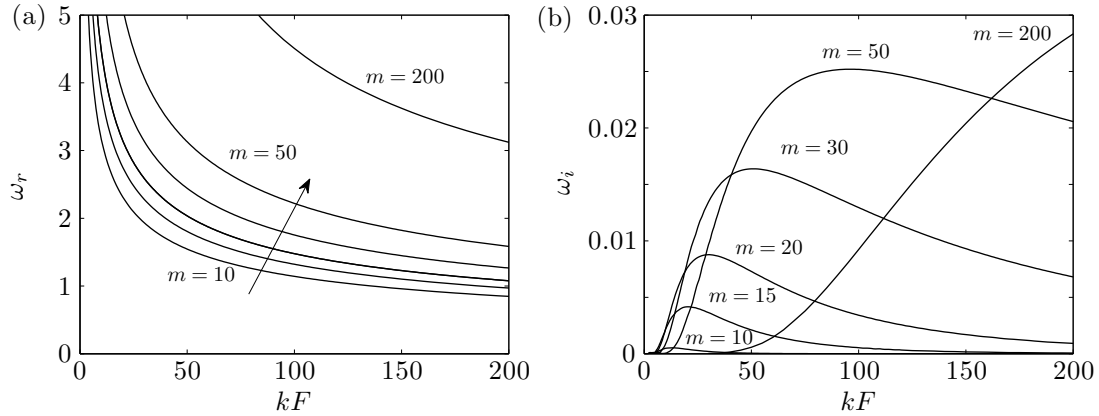

Figure 4.4: (a) Frequency ω_r and (b) growth rate ω_i of the first branch as a function of rescaled vertical wavenumber kF for different azimuthal wavenumbvers m for $\lambda = 0$. Solid lines are numerical results. The azimuthal wavenumber m increases in the direction of the arrows.

Figure 4.4 shows more examples of the frequency and growth rate of the first branch for different azimuthal wavenumbers for $\lambda = 0$. Between the first unstable azimuthal wavenumber $m = 3$ and $m = 10$, the growth rate is very small and lower than $O(10^{-3})$. This is because the potential barrier is very large in this range of azimuthal wavenumbers.

However, for higher m, the growth rate curves increase monotonically with m as observed previously by Le Dizès & Riedinger (2010). Another similarity is that the unstable radial eigenfunctions concentrate near the inner cylinder $r = 1$ as m increases. Following Le Dizès & Riedinger (2010) the limit $m \to \infty$ can be therefore studied asymptotically by introducing the new rescaled variables: $\bar{r} = m(r-1)$, $k_1 = \tilde{k}/m$, $\omega_1 = \omega - m\lambda$ where $(\bar{r}, k_1, \omega_1)$ are assumed to be of order of unity. For large m, the equation (2.25) in chapter 2 approximates at leading

order

$$\frac{\mathrm{d}^2 u_r}{\mathrm{d}\bar{r}^2} - \frac{1}{\bar{Q}}\frac{\mathrm{d}\bar{Q}}{\mathrm{d}\bar{r}}\frac{\mathrm{d}u_r}{\mathrm{d}\bar{r}} + \left[-\bar{Q} - 4k_1^2\lambda + \frac{8k_1^2(\lambda-1)}{\bar{Q}}\right] u_r = O\left(\frac{1}{m}\right), \tag{4.3}$$

where $\bar{Q} = 1 - k_1^2\left\{-\omega_1 + 2(1-\lambda)\bar{r}\right\}^2$. This equation is only valid around $\bar{r} \sim O(1)$ (i.e. around the inner cylinder $r \sim 1$). (4.3) has to be solved numerically except for the particular value $\lambda = 0$ where an analytical solution exists:

$$u_r(\bar{r}) = C\mathrm{e}^{-\mathrm{i}\bar{z}}[U(\alpha,\beta,2\bar{z}) + 2\alpha U(\alpha+1,\beta+1,2\bar{z})], \tag{4.4}$$

where C is a constant, $\bar{z} = k_1^2(\bar{r} - \omega_1/2)^2$, $\alpha = -1/4 - \mathrm{i}/(8k_1)$, $\beta = -1/2$ and U denotes the Kummer's function. We have imposed that (4.4) for $\bar{r} \to \infty$ matches the outgoing wave (4.2).

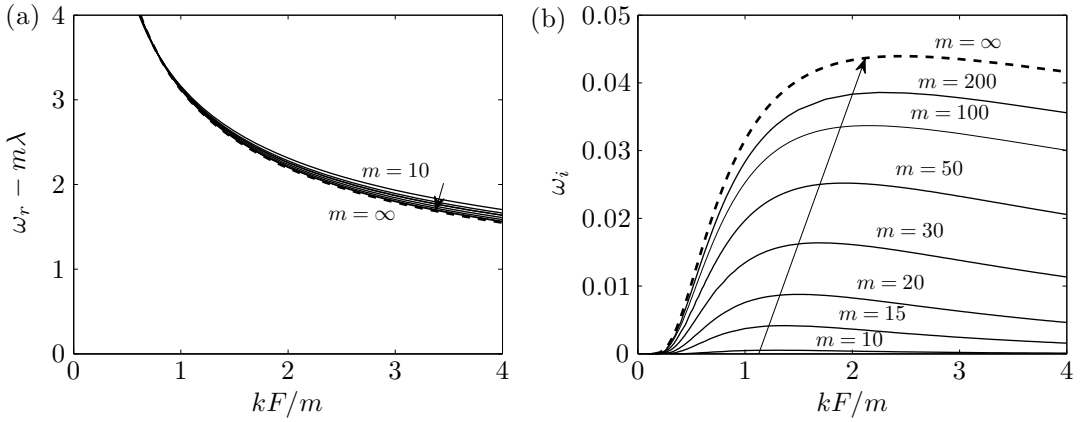

Figure 4.5: Rescaled results of figure 4.4, (a) rescaled frequency $\omega_r - m\lambda$ and (b) growth rate ω_i as a function of rescaled vertical wavenumber kF/m for different azimuthal wavenumbvers m for $\lambda = 0$. Solid lines are numerical results and dashed lines are asymptotic results from (4.4), respectively. Arrows indicate an increase of the azimuthal wavenumber m.

Figure 4.5 shows rescaled results of figure 4.4 together with the asymptotic results obtained from (4.4). We clearly see that the rescaled frequency curves collapse on the asymptotic curve for $m \to \infty$. The growth rate also tends to the asymptotic curve as m increases. The maximum growth rate is $\omega_i \approx 0.042$ obtained for $m \to \infty$ and is reached for $kF/m \approx 2$. This growth rate is of the same order of magnitude as the value computed for the anticyclonic Rankine vortex for the Rossby number $Ro = -1$ in a strongly stratified fluid (Park & Billant, 2012).

2.3.2. Effect of the angular velocity ratio λ

Figure 4.6 shows the maximum growth rate as a function of (a) μ and (b) λ. In figure 4.6(a), the growth rate is scaled by the inner cylinder rotation Ω_i and is plotted as a function of μ for different azimuthal wavenumbers m. We see that the maximum growth rate first decreases exponentially as μ increases from zero, but then it increases exponentially for $\mu > 1$. In figure 4.6(b), the growth rate is now rescaled by the outer cylinder rotation and is plotted as a function of λ in the restricted range $0 < \lambda < 0.1$ for different azimuthal wavenumbers m. We clearly see that the maximum growth rate is reached for $\lambda = 0$ and $m = \infty$, and it decreases exponentially with λ like when η is non zero.

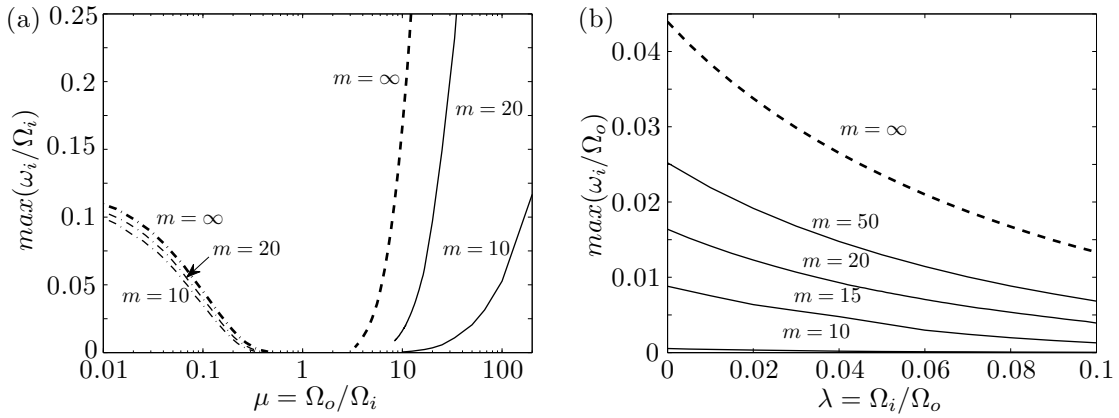

Figure 4.6: (a) Maximum growth rate $max(\omega_i)$ scaled by inner cylinder rotation Ω_i as a function of $\mu = \Omega_o/\Omega_i$ for different azimuthal wavenumbers m. Solid lines are numerical results, dashed line is from the asysmptotic analysis (4.3) for large azimuthal wavenumber $m = \infty$ and dash-dot lines are results from Le Dizès & Riedinger (2010), respectively. (b) Maximum growth rate $max(\omega_i)$ scaled by outer cylinder rotation Ω_o as a function of $\lambda = \Omega_i/\Omega_o$ for different azimuthal wavenumbers m. Solid lines are numerical results and dashed line is from the asymptotic analysis (4.3), respectively.

Chapter 5

Conclusions and perspectives

Conclusions

In this thesis, we have studied the linear stability of columnar vortices and the Taylor-Couette flow in stratified and rotating fluids. Due to the combined effects of the stratification and rotation, there exists inertia-gravity (IG) waves which are at the origin of the instabilities of these two flows.

In chapter 3, we have investigated firstly the stability of the Rankine vortex in a strongly-stratified and rotating fluid. We have found that the radiative instability which exists when the fluid is strongly stratified (Billant & Le Dizès, 2009) is stabilized in the presence of cyclonic rotation ($Ro > 0$). However, the Rankine vortex remains sightly unstable even when the Rossby number is less than unity $Ro < 1$. This stabilization has been explained by means of a WKBJ analysis. When the cyclonic rotation increases, the potential barrier widens so that the IG waves emission and the resulting radiative instability are reduced. In the presence of anticyclonic rotation $Ro < 0$, the Rankine vortex becomes centrifugally unstable if $Ro < -1$ but interestingly, the radiative instability is more dangerous than the centrifugal instability when the anticyclonic rotation is very weak $Ro << -1$. Hence, there is a smooth transition from the radiative instability to the centrifugal instability as Ro increases from $-\infty$. While the maximum growth rate of the radiative instability is obtained at infinite azimuthal wavenumber for the Rankine vortex, vortices with continuous vorticity profiles are most unstable at finite azimuthal wavenumbers. This is due to the damping effect of the singularity at the critical point for continuous vortices. The stabilization by the cyclonic rotation and by the critical point also holds in the case of the Lamb-Oseen vortex. Moreover, we have found that neutral modes exist in the presence of strong cyclonic rotation for both the Rankine vortex and the Lamb-Oseen vortex.

Then, in chapter 4, we have investigated the regime of strong anticyclonic rotation $-1 \leq Ro < 0$ which is centrifugally stable and generally expected to be fully stable. Surprisingly, we have found that the Rankine vortex is still unstable to the radiative instability when the azimuthal wavenumber is sufficiently large. The maximum growth rate is reached in the limit of infinite azimuthal wavenumber like for $Ro > 0$. A WKBJ analysis has shown that this behaviour is due to the fact the size of the potential barrier decreases as the azimuthal wavenumber increases. This radiative instability also occurs on continuous vortices if their vorticity profiles are sufficiently steep. Moreover, the regime $-1 \leq Ro < 0$ for a vortex is analogous to the regime $\mu = \Omega_o/\Omega_i > 1$ for the Taylor-Couette flow. Since this regime in which the outer cylinder rotates faster than the inner cylinder has not been explored before, we have

investigated its stability. We have found that there exists an instability when the stratification is sufficiently strong and for a finite range of non-zero azimuthal wavenumbers. This instability occurs due to the resonance between two families of inertia-gravity waves trapped on each boundary, like for the stratorotational instability in the regime $\mu < 1$ (Molemaker *et al.*, 2001).

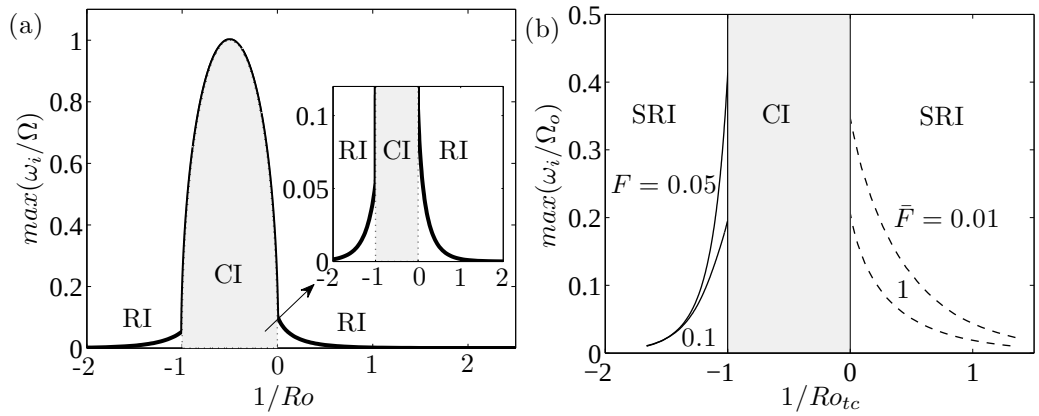

Figure 5.1: (a) Maximum growth rate of the Rankine vortex in a rotating stratified fluid as a function of the inverse of the Rossby number. The region of the centrifugal instability (CI) is shaded and the inset shows the maximum growth rate of the radiative instability (RI). (b) Maximum growth rate of the stratified Taylor-Couette flow as a function of the inverse of the Rossby number for the Taylor-Couette flow $Ro_{tc} = (1-\mu)/(\mu-\eta^2)$, reproduced from the figure 9 in section 2.2 in chapter 4. The region of the centrifugal instability (CI) is shaded and only the growth rate of the stratorotational instability (SRI) is shown.

To summarize, we show in figure 5.1 the maximum growth rate of the Rankine vortex and the Taylor-Couette flow in stratified fluids as a function of the inverse of the Rossby number and the Rossby number $Ro_{tc} = (1-\mu)/(\mu-\eta^2)$, respectively. Due to the radiative instability, the Rankine vortex is unstable for any Rossby number even if the growth rate is very small when $|Ro| \ll 1$. In contrast, only the range $-1 < 1/Ro < 0$ is unstable in homogeneous fluids. Similarly, due to the stratorotational instability, the stratified Taylor-Couette flow is always unstable except in the limit of solid body rotation $\mu = 1$ (i.e. $1/Ro_{tc} \to \pm\infty$ in the figure 5.1b).

Perspectives

Although there are already some experimental results on the radiative instability of the flow around a rotating cylinder in a stratified fluid (Riedinger *et al.*, 2011) or on wave over-reflection (Fridman *et al.*, 2008), it would be interesting to study experimentally the regime of strong anticyclonic rotation found in this thesis to be unstable to the radiative instability. Such experiments might be difficult since it is not easy to generate a single columnar vortex (Riedinger *et al.*, 2010a) but (Riedinger *et al.*, 2011) have shown that experiments with a rotating cylinder can be performed more easily. It would be also feasible to perform experiments on the stratified Taylor-Couette flow in the regime $\mu = 1/\lambda > 1$. According to our numerical results for $\eta = 0.9$ and $\lambda = 0$, the critical Reynolds number is $Re = \Omega_o R_o(R_o - R_i)/\nu \approx 7000$ around the Froude number $Fr = \Omega_o/N \approx 0.05$. This Reynolds number is higher and the Froude

number is lower than those for the regime $\lambda > 1$ previously investigated. This implies that the experimental setup must be large and the stratification strong in order to establish these conditions. However, a larger value of the gap ratio η might be more favorable to observe the instability since the growth rate in the inviscid limit is maximum for $\eta \approx 0.95$.

The present work on linear instabilities could be also extended to non-modal stability analyses. In particular, Antkowiak & Brancher (2004) have investigated transient growth for the Lamb-Oseen vortex in homogeneous fluids. They found that the optimal perturbations can excite a strong bending wave of the vortex core. It would be interesting to analyse the effects of the stratification, rotation and wave emission on this mode.

For simplicity, we have considered only columnar vortices in this thesis. However, real geophysical vortices are generally not columnar but have a pancake shape. A famous example is the Medditerannean eddies. Plougonven & Zeitlin (2002) have shown that pancake vortices in a stratified fluid emit gravity waves and, in turn, these waves can change the vortex shape by interaction. Therefore, stability analyses on pancake vortices might be interesting and very useful to understand more closely the dynamics of Meddies.

Appendix

Appendix: Validation of the Chebyshev collocation spectral method

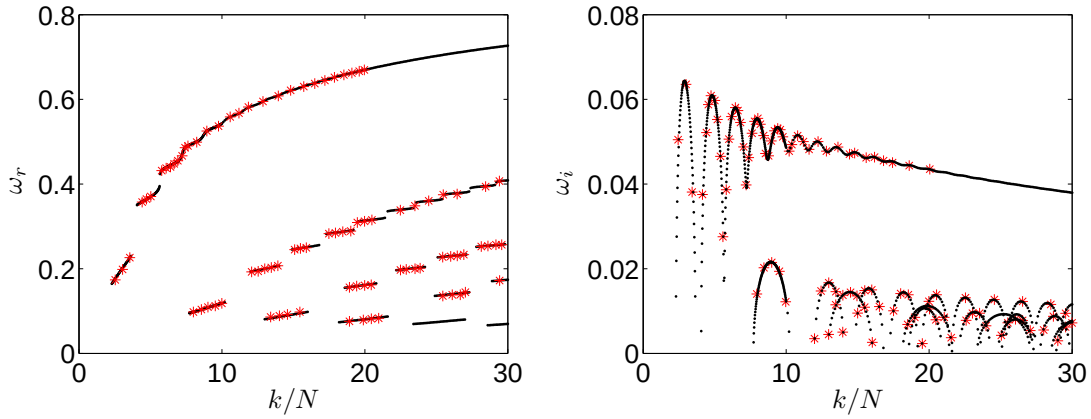

Figure A1: Comparison of (a) frequency and (b) growth rate obtained from the spectral code (black dots) and from results in figure 1 of Riedinger, Le Dizès & Meunier (2010b) (red symbols) for the Taylor-Couette flow for the Froude number $F = 0.2$, $\eta = 0.2$, $\Omega_o/\Omega_i = \eta^2$ and $m = 1$.

In order to validate the Chebyshev collocation spectral code, the results have been compared to the results of Riedinger, Le Dizès & Meunier (2010b) for the inviscid Taylor-Couette flow (figure A1). In this case, the domain size is finite with $\eta = 0.2$ so that we use the linear mapping (2.35) in chapter 2. We see in figure A1 that the agreement is excellent.

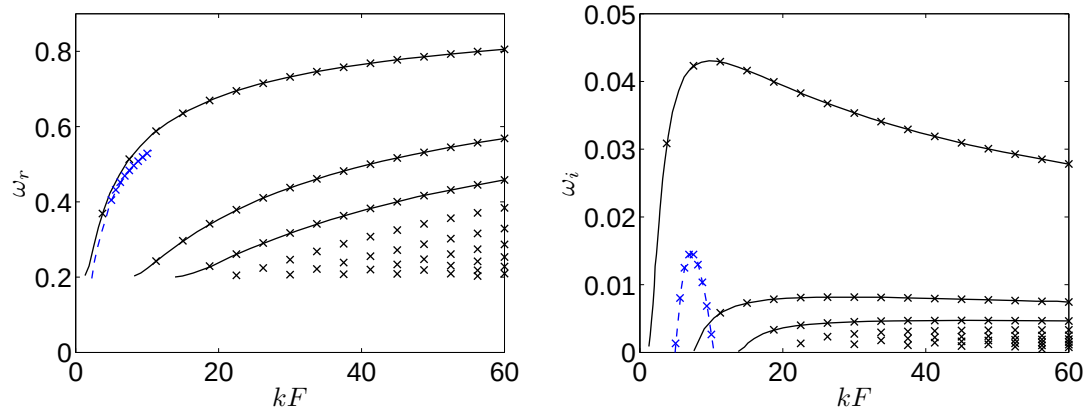

Figure A2: Comparison of (a) frequency and (b) growth rate obtained from the spectral code (symbols) and from results in figure 1 of Riedinger, Le Dizès & Meunier (2011) (lines) for the potential flow around a rotating cylinder for the Froude number $F = 1.25$, $m = 1$ and for the Reynolds numbers $Re = \infty$ (black) and $Re = 1000$ (blue).

The code has been also checked in the case of the flow around a rotating cylinder (figure A2 and Riedinger, Le Dizès & Meunier, 2011). We use the algebraic mapping (2.36) in chapter 2 since the domain is now semi-infinite. Again, we see in figure A2 that the agreement is excellent for both the invisicid case (black lines) and the viscous case (blue lines).

Bibliography

Abramowitz, M. & Stegun, I. A. 1965 *Handbook of Mathematical Functions*. New York: Dover.

Acheson, D. J. 1976 On over-reflexion. *J. Fluid Mech.* **77**, 433–472.

Andereck, C. D., Liu, S. S. & Swinney, H. L. 1986 Flow regimes in a circular Couette system with independently rotating cylinders. *J. Fluid Mech.* **164**, 155–183.

Antkowiak, A. 2005 Dynamique aux temps courts d'un tourbillon isolé. PhD thesis, Université Paul Sabatier de Toulouse.

Antkowiak, A. & Brancher, P. 2004 Transient energy growth for the Lamb-Oseen vortex. *Phys. Fluids* **16**, L1.

Batchelor, G. K. 1964 Axial flow in trailing line vortices. *J. Fluid Mech.* **20**, 645–658.

Batchelor, G. K. 1967 *An Introduction to Fluid Dynamics*. London: Cambridge University Press.

Bender, C. M. & Orszag, S. A. 1978 *Advanced Mathematical Methods for Scientists and Engineers*. New York: McGraw-Hill.

Billant, P. 2010 Zigzag instability of vortex pairs in stratified and rotating fluids. Part 1. General stability equations. *J. Fluid Mech.* **660**, 354–395.

Billant, P. & Chomaz, J.-M. 2000*a* Experimental evidence for a new instability of a vertical columnar vortex pair in a strongly stratified fluid. *J. Fluid Mech.* **418**, 167–188.

Billant, P. & Chomaz, J.-M. 2000*b* Theoretical analysis of the zigzag instability of a vertical columnar vortex pair in a strongly stratified fluid. *J. Fluid Mech.* **419**, 29–63.

Billant, P. & Chomaz, J.-M. 2001 Self-similarity of strongly stratified inviscid flows. *Phys. Fluids* **13**, 1645.

Billant, P. & Le Dizès, S. 2009 Waves on a columnar vortex in a strongly stratified fluid. *Phys. Fluids.* **21**, 106602.

Bordes, G., Moisy, F., Dauxois, T. & Cortet, P.-P 2012 Experimental evidence of a triadic resonance of plane inertial waves in a rotating fluid. *Phys. Fluids* **24**, 014105.

Bower, A. S., Armi, L. & Ambar, I. 1997 Lagrangian Observations of Meddy Formation during A Mediterranean Undercurrent Seeding Experiment. *J. Phys. Oceanogr.* **27**, 2545.

Broadbent, E. & Moore, D. W. 1979 Acoustic destabilization of vortices. *Philos. Trans. R. Soc. London, Ser. A* **290**, 353.

Caton, F., Janiaud, B. & Hopfinger, E. J. 2000 Stability and bifurcations in stratified Taylor-Couette flow. *J. Fluid Mech.* **479**, 93–124.

Charney, J. G. 1971 Geostrophic Turbulence. *J. Atmos. Sci* **28**, 1087–1095.

Chow, K. C., Chan, K. L. & Lau, A. K. H. 2002 Generation of Moving Spiral Bands in Tropical Cyclones. *J. Atmos. Sci* **59**, 2930.

Cortet, P.-P, Lamriben, C. & Moisy, F. 2010 Viscous spreading of an inertial wave beam in a rotating fluid. *Phys. Fluids.* **22**, 086603.

Crow, S. C. 1970 Stability theory for a pair of trailing vortices. *AIAA J.* **8**, 2172–2179.

Cushman-Roisin, B. 1994 *Introduction to geophysical fluid dynamics*. Prentice-Hall.

D'Asaro, E. A. 1988 Generation of Submesoscale Vortices. *J. Geophys. Res.* **93**, 6685–6693.

Fabre, D. & Jacquin, L. 2004 Viscous instabilities in trailing vortices at large swirl numbers. *J. Fluid. Mech.* **500**, 239–262.

Fabre, D., Sipp, D. & Jacquin, L. 2006 The Kelvin waves and the singular modes of the Lamb-Oseen vortex. *J. Fluid. Mech.* **551**, 235.

Fontane, J., Brancher, P. & Fabre, D. 2008 Stochastic forcing of the Lamb-Oseen vortex. *J. Fluid Mech.* **613**, 233–254.

Ford, R. 1994 The instability of an axisymmetric vortex with monotonic potential vorticity in rotating shallow water. *J. Fluid Mech.* **280**, 303–334.

Fridman, A. M., Snezhkin, E. N., Chernikov, G. P., Rylov, A. Yu., Titishov, K. B. & Torgashin, Yu. M. 2008 Over-reflection of waves and over-reflection instability of flows revealed in experiments with rotating shallow water. *Phys. Lett. A* **372**, 4822–4826.

Geli, L., Cosquer, E., Hobbs, R. W., Klaeschen, D., Papenberg, C., Thomas, Y., Menesguen, C. & Hua, B. L. 2009 High resolution seismic imaging of the ocean structure using a small volume airgun source array in the Gulf of Cadiz. *Geophys. Res. Lett.* **36**, L00D09.

Gent, P. R. & McWilliams, J. C. 1986 The instability of barotropic circular vortices. *Geophys. Astrophys. Fluid Dynamics* **35**, 209–233.

Gostiaux, L., Didelle, H., Mercier, S. & Dauxois, T. 2007 A novel internal waves generator. *Exp. Fluids* **42**, 123–130.

Hopfinger, E. J., Browand, F. K. & Gagne, Y. 1982 Turbulence and waves in a rotating tank. *J. Fluid Mech.* **125**, 505–534.

Jones, W. L. 1968 Reflexion and stability of waves in stably stratified fluids with shear flow: a numerical study. *J. Fluid Mech.* **34**, 609–624.

Kelvin, L. 1880 Vibrations of a columnar vortex. *Philos. Mag.* **10**, 155.

Kerswell, R. R. 2002 Elliptical instability. *Annu. Rev. Fluid Mech.* **34**, 83–113.

Kloosterziel, R. C. & van Heijst, G. J. F. 1991 An experimental study of unstable barotropic vortices in a rotating fluid. *J. Fluid Mech.* **223**, 1–24.

Kundu, P. K. & Cohen, I. M. 1990 *Fluid Mechanics*. Elsevier science.

Kuo, H. 1949 Dynamic instability of two-dimensional nondivergent flow in a barotrophic atmosphere. *J. Meteor.* **6**, 105–122.

Lacaze, L., Birbaud, A.-L. & Le Dizès, S. 2005 Elliptic instability in a Rankine vortex with axial flow. *Phys. Fluids.* **17**, 017101.

Le Bars, M. & Le Gal, P. 2007 Experimental Analysis of the Stratorotational Instability in a Cylindrical Couette Flow. *Phys. Rev. Lett.* **99**, 064502.

Le Dizès, S. 2000 Non-axisymmetric vortices in two-dimensional flows. *J. Fluid Mech.* **406**, 176–198.

Le Dizès, S. 2004 Viscous Critical-Layer Analysis of Vortex Normal Modes. *Stud. Appl. Math.* **112** (4), 315–332.

Le Dizès, S. & Billant, P. 2009 Radiative instability in stratified vortices. *Phys. Fluids.* **21**, 096602.

Le Dizès, S. & Lacaze, L. 2005 An asymptotic description of vortex Kelvin modes. *J. Fluid Mech.* **542**, 69.

Le Dizès, S. & Riedinger, X. 2010 The strato-rotational instability of Taylor-Couette and Keplerian flows. *J. Fluid Mech.* **660**, 147.

Lindzen, R. S. & Barker, J. W. 1985 Instability and wave over-reflection in stably stratified shear flow. *J. Fluid Mech.* **151**, 189–217.

Lindzen, R. S., Farrell, B. & Tung, K-K. 1980 The Concept of of Wave Overreflection and Its Application to Baroclinic Instability. *J. Atmos. Sci.* **37**, 44.

Lord Rayleigh 1917 On the Dynamics of Revolving Fluids. *Proc. Roy. Soc. London, A* **94**, 148–154.

Maas, L. R. M., Benielli, D., Sommeria, J. & Lam, F.-P. A. 1997 Observation of an internal wave attractor in a confined stably-stratified fluid. *Nature* **388**, 557–561.

McWilliams, J. C. 1985 Submesoscale, Coherent Vortices in the Ocean. *Rev. Geophys.* **23**, 165–182.

Ménesguen, C., Hua, B. L., Papenberg, C., Klaeschen, D., Géli, L. & Hobbs, R. 2009 Effect of bandwidth on seismic imaging of rotating stratified turbulence surrounding an anticyclonic eddy from field data and numerical simulations. *Geophys. Res. Lett.* **36**, L00D05.

Meunier, P. & Leweke, T. 2005 Elliptic instability of a co-rotating vortex pair. *J. Fluid Mech.* **533**, 125–159.

Miles, J. W. 1957 On the reflection of sound at an interface of relative motion. *J. Acous. Soc. Am.* **17**, 226–228.

Molemaker, M. J., McWilliams, J. C. & Yavneh, I. 2001 Instability and Equilibrium of Centrifugally Stable Stratified Taylor-Couette Flow. *Phys. Rev. Lett.* **86**, 5270.

Mowbray, D. E. & Rarity, B. S. H. 1967 A theoretical and experimental investigation of the phase configuration of internal wave of small amplitude in a density stratified fluid. *J. Fluid Mech.* **28**, 1–16.

Nadiga, B. T. & Aurnou, J. M. 2008 A Tabletop Demonstration of Atmospheric Dynamics: Baroclinic Instability. *Oceanography* **21(4)**, 196–201.

Nastrom, G. D., Gage, K. S. & Jasperson, W. H. 1984 Kinetic energy spectrum of large and mesoscale atmospheric processes. *Nature* **310**, 36–38.

Park, J. & Billant, P. 2012 Radiative instability of an anticyclonic vortex in a stratified rotating fluid. *J. Fluid Mech.* **707**, 381–392.

Peacock, T. & Weidman, P. 2005 The effect of rotation on conical wave beams in a stratified fluid. *Exp. Fluids* **39**, 32–37.

Pedlosky, J. 1979 *Geophysical Fluid Dynamics*. Springer-Verlag.

Plougonven, R. & Zeitlin, V. 2002 Internal gravity wave emission from a pancake vortex: An example of wave-vortex interaction in strongly stratified flows. *Phys. Fluids* **14**, 1259.

Pradeep, D. S. & Hussain, F. 2006 Transient growth of perturbations in a vortex column. *J. Fluid Mech.* **550**, 251–288.

Praud, O., Sommeria, J. & Fincham, A. M. 2006 Decaying grid turbulence in a rotating stratified fluid. *J. Fluid Mech.* **547**, 389–412.

Riedinger, X., Le Dizès, S. & Meunier, P. 2010b Viscous instability of a Lamb-Oseen vortex in a stratified fluid. *J. Fluid Mech.* **645**, 255–278.

Riedinger, X., Le Dizès, S. & Meunier, P. 2011 Radiative instability of the flow around a rotating cylinder in a stratified fluid. *J. Fluid Mech.* **672**, 130–146.

Riedinger, X., Meunier, P. & Le Dizès, S. 2010a Instability of a vertical columnar vortex in a stratified fluid. *Exp. Fluids.* **49**, 673–681.

Saffman, P. G. 1992 *Vortex Dynamics*. Cambridge: Cambridge University Press.

Schecter, D. A. 2008 The Spontaneous Imbalance of an Atmospheric Vortex at High Rossby Number. *J. Atmos. Sci* **65**, 2498.

Schecter, D. A., Dubin, D. H. E., Cass, A. C., Driscoll, C. F., Lansky, I. M. & O'neil, T. M. 2000 Inviscid damping of asymmetries on a two-dimensional vortex. *Phys. Fluids.* **12**, 2397.

Schecter, D. A. & Montgomery, M. T. 2004 Damping and pumping of a vortex Rossby wave in a monotonic cyclone: Critical layer stirring versus inertia-buoyancy wave emission. *Phys. Fluids.* **16**, 1334.

Schecter, D. A. & Montgomery, M. T. 2006 Conditions that inhibit the spontaneous radiation of spiral inertia-gravity waves from an intense mesoscale cyclone. *J. Atmos. Sci.* **63**, 435.

Schecter, D. A., Montgomery, M. T. & Reasor, P. D. 2002 A Theory for the Vertical Alignment of a Quasigeostrophic Vortex. *J. Atmos. Sci.* **59**, 150.

Schmid, Peter J. & Henningson, Dan S. 2001 *Stability and transitions in shear flows*. Springer.

Shalybkov, D. & Rüdiger, G. 2005 Stability of density-stratified viscous Taylor-Couette flows. *Astron. Astroph.* **438**, 411–417.

Takehiro, S. & Hayashi, Y. 1992 Over-reflection and shear instatbility in a shallow-water model. *J. Fluid Mech.* **236**, 259–279.

Weideman, J. A. C. & Reddy, S. C. 2000 A MATLAB Differentiation Matrix Suite. *ACM Transactions on Mathematical Software* **26**.

Yavneh, I., McWilliams, J. C. & Molemaker, M. J. 2001 Non-axisymmetric instability of centrifugally stable staratified taylor-couette flow. *J. Fluid Mech.* **448**, 1–21.